

POLITECNICO DI MILANO

School of Industrial Process Engineering

Master Degree in Materials Engineering and Nanotechnology

Department of Chemistry, Material and Chemical Engineering "Giulio Natta"



Self-assembled monolayer and electroless Ni-B as alternative barrier layer and interconnect for ULSI technology

Supervisor: **Prof. Luca Magagnin**

Co-Supervisor: **Sr. Dr. Silvia Armini**

Master Degree Thesis by:

Saracino Gianmaria

Matricola **784395**

Academic Year: **2012/2013**

POLITECNICO DI MILANO

School of Industrial Process Engineering

Master Degree in Materials Engineering and Nanotechnology

Department of Chemistry, Material and Chemical Engineering "Giulio Natta"



Self-assembled monolayer and electroless Ni-B as alternative barrier layer and interconnect for ULSI technology

Supervisor: **Prof. Luca Magagnin**

Co-Supervisor: **Sr. Dr. Silvia Armini**

Master Degree Thesis by:

Saracino Gianmaria

Matricola **784395**

Academic Year: **2012/2013**



English Abstract

Copper represents the main option as conductive material for interconnects in the Ultra-Large Scale Integrated (ULSI) technology since the replacement of aluminium in 1997. The introduction was triggered by the higher conductivity and electromigration resistance offered by copper. The necessity to avoid contact between the metal and the underlying SiO₂, because of the high interdiffusion coefficient of copper in silicon oxide, brought the semiconductor industry to develop and place a barrier layer at the metal/dielectric interface. Common practice, today, is the use of a double layer of Ta/TaN creating a final stack of SiO₂/Ta/TaN/Cu. In the Damascene process, a sputtering or Physical Vapour Deposition (PVD) step is employed for the deposition of the barrier layer, and, with the same technique, also a Cu seed layer can be conformally deposited. Such seed layer is necessary for the bottom-up filling of the vias or trenches by electroplated copper. To keep Moore's law verified, the future node generations will need to continue downscaling process, together with the barrier layer stack. Due to the impossibility to realize a conformal barrier layer of thickness below 5-6 nm, a rethinking process of the materials and deposition techniques needs to be taken in order to win the challenge.

An "all-wet" process was developed and improved in this project as an alternative road for the realization of a metal/barrier/dielectric stack. NiB is already known to have good barrier features against copper diffusion, possessing good adhesion and thermal stability, together with remarkable conductive properties. The alloy was deposited on a Si/SiO₂ substrate appropriately modified through the use of Self-Assembled Monolayers (SAMs) and catalysed by immersion in a PdCl₂ solution. The goal of this project is the evaluation of the electroless NiB thin film and line conductivity on SAMs, on both blanket and patterned silicon, so that a good comparison with copper and other metals may be possible.

The first part of this master thesis project is the evaluation of the SAM. Two different precursors, (Aminoethylaminomethyl)-phenylethyltrimethoxysilane (PEDA) and (3-Trimethoxysilylpropyl)-

diethylenetriamine (DETA), both belonging to the amino-silane family, were chosen because of their ability to create strong bonds with the SiO₂ substrate and because of the presence of negatively charged tail groups. The SAM was deposited with different techniques: on coupons using a solvent-based solution, by vapour deposition on full wafer. Different times were used for both depositions so that the best characteristics could be selected. Contact angle (CA) was used as a simple technique to check the presence and quality of the organic layer, while the near-zero thickness was measured through the use of x-ray reflectivity (XRR) and ellipsometry (EP10) techniques. The number of top amino-groups was counted through the use of X-ray photoelectron spectroscopy (XPS), and the same technique was employed to evaluate the quantity of Pd uptake versus immersion time on the differently processed SAMs. A uniform uptake of strongly bonded Pd atoms is essential to correctly catalyse the subsequent metal deposition. Two different NiB chemistries (10% and 1% of B) were employed covering a wide range of different deposition options (deposition time, anneal, etc.). Thin film resistivity could be calculated through the evaluation of the thickness of the deposit, with XRR techniques, and of the resistance, through 4-point probe measurements. Using the same technique, also the growth rate of the film on different substrates was measured. For all the deposit adhesion, measured through the use of a 4-point bending tool with a visual monitoring of the interface through Scanning Electron Microscopy (SEM), proved to be strong enough to satisfy the requirements necessary for the successive processing step of the Integrated Circuit (IC) fabrication. Chemical compositions of the deposits were evaluated using Elastic Recoil Detection (ERD). Finally, the chemistry was transferred to patterned coupons for the evaluation of line resistivity. Liquid SAM, with its superior properties with respect to the vapour one, was the only deposited on the patterned samples before the thick deposition (up to 300 nm) of NiB. The removal of excessive metal was realized through Chemical-Mechanical Polishing (CMP), using a MECAPOL polisher. A first run confirmed the best characteristics of DETA and NiB 1% over the other deposits. After a good knowledge of the CMP and a good evaluation of the line filling through the use of optical microscopy and SEM were achieved, a last run of samples was made in order to be inspected under Transmission Electron Microscopy (TEM). Resistance of the coupons were evaluated

though 4-point probe measurements while accurate knowledge of the section area of the line gave the possibility to calculate resistivity. The realization of lines with resistivity below the one of W with widths down to 14 nm was proven possible.

Italian Abstract

Il rame rappresenta la principale scelta per le interconnessioni di metallo nella tecnologia ULSI dal 1997, anno in cui è subentrato all'alluminio, data la sua maggiore conducibilità rispetto a quest'ultimo. A causa dell'alto coefficiente di diffusione del Cu all'interno del layer dielettrico di SiO₂, è stato necessario l'introduzione di uno layer intermedio che evitasse il contatto diretto tra il metallo e il substrato. Questo ruolo è oggi svolto da un doppio strato di Ta/TaN che viene normalmente depositato tramite PVD o sputtering, insieme ad un primo strato (seed) di rame necessario per il successivo riempimento di vie o trincee tramite elettrodeposizione. Man mano che le dimensioni vanno riducendosi come risultato del potenziamento e abbassamento dei costi dei circuiti integrati, come descritto dalla legge Moore, lo strato barriera a base di tantalio, che difficilmente riuscirà a raggiungere dimensioni inferiori ai 5 nm mantenendo accettabili caratteristiche, dovrà essere abbandonato. Un ripensamento totale dei materiali e delle tecniche di deposizione è quindi essenziale per permettere la creazione di barriere con caratteristiche migliori alle tradizionali rispettando i nuovi vincoli dimensionali.

In questo progetto è stato sviluppato e migliorato un processo "all-wet" che comprende più passaggi in soluzione per la realizzazione della struttura dielettrico/barriera/metallo. Il conduttore è rappresentato da una lega a base di nickel-boro, "electroless" depositato su substrato di SiO₂, opportunamente funzionalizzato tramite l'uso di monostrati organici autoassemblati (SAM). La deposizione di metallo è possibile previa catalizzazione tramite immersione in una soluzione di PdCl₂. Il NiB è noto avere buone proprietà di barriera se accoppiato con rame: oltre a non permettere la diffusione degli atomi di silicio possiede buona adesione sul SAM e stabilità termica. In questo progetto si tenterà di valutare le caratteristiche del film e della linea di NiB in modo tale da avere un possibile confronto con altri metalli quali Cu e Ni.

La prima parte del progetto è centrata sulla caratterizzazione del SAM. Due differenti precursori organici sono stati utilizzati, l'(aminoetilaminometil)-feniltrimetossisilano (PEDA) e il (3-trimetossisililpropil)-dietilentriammina (DETA), entrambi appartenenti alla famiglia degli ammino-silani, scelti per le loro caratteristiche di formare legami forti con il substrato e la presenza di gruppi carichi negativamente (ammine) in coda alla molecola. Per la deposizione sono state utilizzate una tecnica di deposizione liquida, in soluzione organica, e una a vapore. Tramite la variazione dell'angolo di contatto è stato possibile valutare l'effettiva deposizione del SAM e quindi, tramite ellissometria (EP10) e riflettività tramite raggi x (XRR), ne è stato valutato lo spessore. La spettroscopia fotoelettronica tramite raggi x (XPS) è stata quindi impiegata per valutare la composizione atomica superficiale dello strato organico. Successivamente la stessa è stata anche impiegata per stimare l'adsorbimento superficiale di palladio da parte del SAM. Nella seconda parte del progetto ci si è concentrati più sull'ottimizzazione del processo di deposizione electroless. Due bagni con composizioni diverse sono state utilizzate (NiB 1% e NiB 10%) e diverse caratteristiche di deposizione (tempi di deposizione, ricottura, ecc.). La misurazione dello spessore del film, tramite XRR, e della resistenza elettrica, attraverso misure a quattro terminali, hanno reso possibile la misura su thin film e del tasso di crescita del film stesso. L'adesione, misurata tramite uno strumento di piegatura su quattro punti, si è dimostrata elevata e sufficiente, per tutti i campioni, per sostenere i successivi passaggi necessari nell'industria del circuito integrato (IC). La composizione chimica del film di NiB al variare della profondità è stata possibile grazie alla tecnica di analisi di richiamo elastico (ERD). La deposizione è stata quindi trasferita sui campioni patternati dove si è cercato di isolare il caso in cui la resistività di linea risultasse minore. La combinazione NiB 1% con DETA si è rivelata inizialmente la migliore sotto questo punto di vista ed è quindi stata esaminata più attentamente. Una comprensione migliore della fase di chemical mechanical polishing (CMP), tramite l'uso del polisher MECAPOL, affiancato da immagini da microscopio ottico e da microscopio a scansione elettronica (SEM), ha portato alla ottimizzazione del processo di creazione delle linee. A quel punto è stato possibile selezionare i migliori campioni per essere analisi tramite microscopio a scansione a effetto tunnel (TEM). La conoscenza esatta della sezione delle linee unita alla resistenza di queste valutata tramite

misurazione a quattro terminali ha reso possibile il calcolo della resistività di siffatte linee. È stato quindi dimostrato che è possibile depositare tramite ELD, NiB in linee con larghezze pari a 14 nm, con resistività comparabili a tutti gli altri metalli presenti in commercio.



Table of Contents

CHAPTER 1: INTRODUCTION.....	1
1.1 NANOTECHNOLOGY	1
1.2 COPPER INTERCONNECT TECHNOLOGY	4
1.2.1 <i>The Damascene Process</i>	5
1.2.2 <i>Issues in Cu interconnections</i>	10
1.2.3 <i>Requirements for barrier layers</i>	11
1.3 BARRIER LAYER STATE OF ARTS	12
1.4 SELF-ASSEMBLED MONOLAYER (SAM)	14
1.4.1 <i>SAM as advanced barrier layer in interconnect technology</i>	19
1.4.2 <i>SAM deposition techniques</i>	22
1.4.2.1 Liquid deposition	22
1.4.2.2 Vapour deposition	22
1.5 ELECTROLESS DEPOSITION (ELD)	23
1.5.1 <i>Metal Ions Source</i>	25
1.5.2 <i>Reducing Agents</i>	25
1.5.3 <i>Complexing Agents</i>	27
1.5.4 <i>Additives</i>	28
1.6 NICKEL-BORON ELECTROLESS DEPOSITION	29
CHAPTER 2: AIM OF THE WORK.....	35
CHAPTER 3: EXPERIMENTAL TECHNIQUES	38
3.1 SAMs DEPOSITION TECHNIQUE	38
3.1.1 <i>Vapour</i>	38
3.1.2 <i>Liquid</i>	40

3.2	CONTACT ANGLE	40
3.3	SPECTROSCOPIC ELLIPSOMETER (EP10)	42
3.1	X-RAY REFLECTIVITY (XRR).....	45
3.2	X-RAY DIFFRACTIVITY (XRD).....	47
3.3	TOTAL X-RAY FLUORESCENCE (TXRF).....	48
3.4	FOURIER TRANSFORM INFRARED SPECTROSCOPY (FTIR)	49
3.5	ANAEROBIC GLOVEBOX.....	51
3.6	X-RAY PHOTOELECTRON SPECTROSCOPY (XPS)	52
3.7	SCANNING ELECTRON MICROSCOPE (SEM)	54
3.8	TRANSMISSION ELECTRON MICROSCOPY (TEM)	56
3.9	FOUR POINT PROBE.....	57
3.10	CHEMICAL-MECHANICAL POLISHING.....	60
CHAPTER 4: SELF-ASSEMBLED MONOLAYER CHARACTERIZATION		62
4.1	INTRODUCTION.....	62
4.2	PEDA.....	64
4.2.1	<i>Materials and Methods</i>	64
4.2.1.1	Sample preparation.....	64
4.2.2	<i>Analysis and Results</i>	66
4.2.3	<i>Discussion</i>	71
4.3	DETA.....	72
4.3.1	<i>Materials and Methods</i>	73
4.3.1.1	Sample preparation.....	73
4.3.2	<i>Analysis and Results</i>	73
4.3.3	<i>Discussion</i>	77
4.4	OBSERVATIONS.....	78
CHAPTER 5: ELECTROLESS DEPOSITION OF NIB ON SAM		80
5.1	INTRODUCTION.....	80

5.2	PALLADIUM DEPOSITION	81
	5.2.1 <i>Materials and Methods</i>	81
	5.2.1.1 Sample preparation.....	81
	5.2.2 <i>Analysis and results</i>	82
	5.2.3 <i>Discussion</i>	83
5.3	ELECTROLESS DEPOSITION OF NiB	84
	5.3.1 <i>Materials and Method</i>	84
	5.3.1.1 Sample preparation.....	84
	5.3.1.2 Analysis techniques	86
	5.3.2 <i>Thin Film Resistivity</i>	86
	5.3.2.1 Process description	86
	5.3.2.2 Results presentation	88
	5.3.2.3 Discussion.....	92
	5.3.3 <i>Growth Rate Evaluation</i>	93
	5.3.3.1 Process description	93
	5.3.3.2 Results presentation	93
	5.3.3.3 Discussion.....	95
	5.3.4 <i>Adhesion Evaluation</i>	96
	5.3.5 <i>Chemical analysis</i>	98
5.4	NiB IN TRENCHES.....	100
	5.4.1 <i>Materials and Methods</i>	100
	5.4.2 <i>Results Presentation and Discussion</i>	105
	5.4.2.1 First run	105
	5.4.2.2 Second run.....	106
	5.4.2.3 Third run.....	108
	5.4.3 <i>TEM Analysis</i>	109
	5.4.3.1 Line shape.....	109
	5.4.3.2 Line resistivity.....	113
CHAPTER 6: CONCLUSIONS AND FUTURE PERSPECTIVES.....		118

6.1	CONCLUSIONS	118
6.2	FUTURE PERSPECTIVES	121
	REFERENCES	123

List of Figures

FIGURE 1.1 - A BETTER UNDERSTANDING OF THE NANOSCALE DIMENSION AND ITS ACHIEVEMENTS MAY BE ACHIEVED CONFRONTING OBJECTS PRESENT COMMONLY IN NATURE WITH HAND-MADE ONES.	2
FIGURE 1.2 - SCHEMATIC CROSS SECTION OF AN INTEGRATED CIRCUIT, WHICH SHOWS THAT THE METALLIC INTERCONNECTS ARE MECHANICALLY SUPPORTED AND ELECTRICALLY INSULATED BY AN INTER-LEVEL DIELECTRIC (ILD).....	4
FIGURE 1.3 - CU-DAMASCENE PROCESS FLOW: THE DIFFERENCES BETWEEN SINGLE AND DOUBLE DAMASCENE PROCESSES ARE QUITE EVIDENT FROM THE PICTURE AS MUCH AS THE LOWER AMOUNT OF STEPS IN THE DD ONE.	6
FIGURE 1.4 - DUAL DAMASCENE PROCESS STEPS	7
FIGURE 1.5 - A DUAL DAMASCENE ARCHITECTURE SHOWING THE DIFFERENT MATERIALS IN THE UNIT STRUCTURE	9
FIGURE 1.6 - (A) SCHEMATIC OF THE EFFECTIVE RESISTANCE OF A CU INTERCONNECT AND (B) VARIATION OF RESISTIVITY VERSUS THE THICKNESS OF THE BARRIER LAYER	12
FIGURE 1.7 - TEM CROSS-SECTION OF AN ALD TAN BARRIER AND CO CAP LAYER ³²	13
FIGURE 1.8 – PUBLICATIONS REGARDING SAMs FROM 1987 TO 2009.....	16
FIGURE 1.9 - A) REPRESENTATION OF A SURFACTANT MOLECULE WITH THE THREE MAIN PARTS COMPOSING IT (HEAD, BACKBONE AND TAIL). B) SCHEMATIC OF A SELF-ASSEMBLED MONOLAYER ON A SUBSTRATE.	17
FIGURE 1.10 - SCHEMATIC OF THE REACTION BETWEEN A TRIMETHOXY-SILANE MOLECULE AND A HYDROXYL-FUNCTIONALIZED STRUCTURE. THE PROCESSES CAN BE SUMMARIZED IN 4 STEPS: HYDROLYSIS OF THE METHOXY GROUP, CONDENSATION OF THE MOLECULES IN OLIGOMERS, FORMATION OF WEAK H-BONDS AND THE FINAL FORMATION OF THE MONOLAYER.	18
FIGURE 1.11 - REPRESENTATION OF AN AMINO-SAM (APTMS) USED AS A BARRIER LAYER FOR SUCCESSIVE COPPER DEPOSITION	19
FIGURE 1.12 - MODEL OF A SILANE MOLECULE: ALL THE MOLECULES IN THIS GROUP HAVE IN COMMON THE SILICON ATOM, UNITING THE HYDROLYSABLE GROUPS AND THE BACKBONE.	21

FIGURE 1.13 - ELECTROLESS DEPOSITION PROCESS SCHEMATIC. UP: THE REACTION IS CATALYZED BY THE SUBSTRATE.
DOWN: THE REACTION IS CATALYZED BY THE DEPOSITED METAL. 24

FIGURE 1.14 - Ni-B PHASE DIAGRAM..... 33

FIGURE 2.1 - SCHEMATIC OF THE REALIZED STACK. 36

FIGURE 3.1 - THE UVO CLEANER (LEFT) AND THE SILANIZATION OVEN (RIGHT) USED DURING THE RESEARCH⁹⁶..... 39

FIGURE 3.2 - SCHEMATIC REPRESENTATION OF THE UVO CLEANING MECHANISM⁴⁹..... 39

FIGURE 3.3 - A) PICTURE OF A WATER DROPLET ON A SURFACE; B) SCHEMATIC REPRESENTATION OF THE LIQUID
CONTACT ANGLE AND SURFACE TENSIONS AND ENERGIES..... 41

FIGURE 3.4 - EFFECTS OF SiO₂ SURFACE STATE ON HYDROPHILIC BEHAVIOUR. A) UVOZONE CLEANED. B) NH₂-SAM
FUNCTIONALIZED..... 42

FIGURE 3.5 - ELLIPSOMETER WORKING PRINCIPLE 43

FIGURE 3.6 - PICTURE OF THE ELLIPSOMETER EMPLOYED: THE LASER EMITTER, THE WAFER STAGE AND THE DETECTOR
CAN BE EASILY INDIVIDUATED..... 44

FIGURE 3.7 - DIAGRAM OF X-RAY SPECULAR REFLECTION. 45

FIGURE 3.8 - XRR SPECTRUM SAMPLE: THE INFORMATION THAT CAN BE EXTRAPOLATED FROM THE PLOT ARE
DESCRIBED (INFORMATION PROVIDED BY X-RAY REFLECTIVITY)⁹⁹..... 46

FIGURE 3.9 - SCHEMATIC VIEW OF A TXRF INSTRUMENT..... 49

FIGURE 3.10 - SCHEMATIC OF A BEAM-SPLITTER, PRESENT IN EVERY FTIR INSTRUMENT. 50

FIGURE 3.11 - SCHEMATIC OF THE TRANSFORMATION FROM AN IR SOURCE SIGNAL INCIDENT ON A
SUBSTRATE/SUBSTANCE TO INTERPRETABLE IR SPECTRA..... 50

FIGURE 3.12 - GLOVEBOX OVERVIEW USED FOR COPPER ELD (PLAS LABS, MODEL 855-AC)..... 51

FIGURE 3.13 - SCHEMATIC REPRESENTATION OF AN XPS MEASUREMENT 53

FIGURE 3.14 - REPRESENTATION OF THE POSSIBLE PHENOMENA RELATED TO THE INTERACTION OF X-RAYS WITH A
SPECIMEN TOGETHER WITH THE INSTRUMENT USED TO COLLECT INFORMATION FROM THEM. 54

FIGURE 3.15 - SEM MICROSCOPE SCHEME..... 55

FIGURE 3.16 - SIMPLE SCHEMATIC OF A TRANSMISSION ELECTRON MICROSCOPE. 56

FIGURE 3.17 - REPRESENTATION OF A FOUR-POINT PROBE USED FOR THE MEASUREMENT OF SHEET RESISTANCE.. 58

FIGURE 3.18 - CAPTION OF THE 4 NEEDLES USED TO MEASURE THE RESISTIVITY ON PATTERNED COUPONS..... 59

FIGURE 3.19 - SCHEMATIC CMP STEP.....	60
FIGURE 4.1 - MOLECULAR STRUCTURE OF PEDA.....	64
FIGURE 4.2 - EXAMPLE OF THICKNESS DATA COLLECTED BY THE F5 TOOL.	69
FIGURE 4.3 - CHEMICAL STRUCTURE OF DETA.....	72
FIGURE 5.1 - REPRESENTATION OF THE ELD STEPS. A) DIW RINSE. B) IMMERSION IN PdCl ₂ . C) PRE-RINSE IN DIW & ADDITIVE M/B. D) NiB SOLUTION IMMERSION. E) POST RINSE IN DIW.	85
FIGURE 5.2 - REPRESENTATION OF THE CRACK CREATED TO ESTIMATE THE ADHESION OF THE METAL LAYER.	96
FIGURE 5.3 - ADHESION ISSUES: A LOW ADHESION MAY CAUSE THE LIFTING OF THE METAL LAYER.	97
FIGURE 5.4 - REPRESENTATION OF THE DIE: EVERY DIE IS DIVIDED IN 3 SUB DIES (A0, A1, A2). EACH COLUMN AND ROW CONTAINS DIFFERENT FEATURES. IN THE PRESENT WORK THE 5 MM LONG LINE WAS MEASURED, WITH NOMINAL DEPTH OF 60 NM. WIDTH RANGED FROM 10 NM TO 825 NM.....	101
FIGURE 5.5 - PARTICULAR OF THE CMP MECAPOL TOOL.....	101
FIGURES 5.6 - PARTICULARS OF THE PATTERNED COUPONS AFTER CMP; THE SQUARE REPRESENT THE CONTACTS NECESSARY FOR THE ELECTRIC MEASUREMENT OF THE RESISTANCE OF THE LINES.	103
FIGURES 5.7 – DETAILS OF THE PATTERNED SAMPLE PEDA LIQ 2H WITH NiB 10%.	104
FIGURES 5.8 - DETAILS OF THE COUPON PEDA LIQ 5H WITH NiB 10%.	105
FIGURE 5.9 – TEM IMAGE OF THE SECTION OF THE PARALLEL IN THE PATTERNED COUPONS; ONLY THE MIDDLE ONE IS ABLE TO CONDUCT, THE OTHER FOUR ARE DUMMIES.	110
FIGURE 5.10 - TEM SECTION OF LINE #1.....	110
FIGURE 5.11 - (LEFT) HAADF-STEM OF THE PREVIOUSLY PICTURED SECTION AND (RIGHT) DF-STEM OF IT.	111
FIGURE 5.12 - (FROM UPPER LEFT, CLOCKWISE) SECTION OF THE FOUR CONDUCTIVE LINES. THE EXPLOSION IN THE SECOND LINE IS EVIDENT FROM THE IMAGE.	114

List of Tables

TABLE 1.1 – REDUCING AGENTS COMMONLY USED IN ELD PROCESSES.	26
TABLE 4.1 - SAMs PRECURSORS EMPLOYED WITH THE RESPECTIVE MOLECULAR STRUCTURE.....	63
TABLE 4.2 - CA VALUES, TOGETHER WITH STANDARD DEVIATIONS, OF PEDa WET-DEPOSITED CONSIDERING DIFFERENT DEPOSITION TIMES.....	66
TABLE 4.3 - ATOMIC CONCENTRATIONS OF THE ELEMENTS FOUND ON THE SURFACES.	71
TABLE 4.4 - CA VALUES FOR LIQUID DEPOSITED DETA.....	73
TABLE 4.5 - ATOMIC RELATIVE CONCENTRATIONS OF SPECIES ON THE COUPONS.	77
TABLE 5.1 - ADHESION PROPERTIES OF NiB 10% AND 1% ON DIFFERENTLY PROCESSED BARRIER LAYERS.	98
TABLE 5.2 - ATOMIC SPECIES PRESENT IN THE COUPONS.	99
TABLE 5.3 - LINE DIMENSION AND RESISTIVITY AS EVALUATED FROM TEM.	116

List of Plots

PLOT 4.1 - CONTACT ANGLE VALUES OF VAPOUR DEPOSITED PEDA, FOR 1H AND 30' DEPOSITION.	67
PLOT 4.2 - XRR PLOTS OF PEDA SAM FOR DIFFERENT DEPOSITION TIMES. THE PLOT IS PRESENTED IN TERMS OF REFLECTIVITY VALUE OF THE X-RAY VS THE ANGLE (2θ) OF REFLECTION.	68
PLOT 4.3 - THICKNESSES VALUES OF PEDA VS TIME. TWO DIFFERENT MEASURES, MADE WITH TWO DIFFERENT MEASURING SYSTEMS ARE PRESENTED: ONE THROUGH XRR, ONE EMPLOYING ELLIPSOMETRY.	68
PLOT 4.4 - THICKNESS VALUE, MEASURED THROUGH F5 INSTRUMENT FOR DEPOSITION TIMES OF 30' AND 1H.	69
PLOT 4.5 - ATOM COUNT VERSUS THE BONDS BINDING ENERGY: FROM THESE PLOTS IT IS POSSIBLE TO HAVE AN ESTIMATION OF THE ATOMIC PERCENTAGES IN THE SURFACE.	70
PLOT 4.6 - CONTACT ANGLE VALUES OF VAPOUR DEPOSITED PEDA, FOR 1H AND 30' DEPOSITION.	74
PLOT 4.7 - XRR PLOTS OF DETA SAM FOR DIFFERENT DEPOSITION TIMES. LIKE PLOT 4.1 EVERY CURVE REPRESENT, FOR EVERY A DIFFERENT DEPOSITION TIME, THE REFLECTIVITY VS THE ANGLE (2θ) OF REFLECTION.	75
PLOT 4.8 - THICKNESSES VALUES OF DETA VS TIME. THE TWO DIFFERENT MEASURES, MADE THROUGH THE USE OF THE XRR METHOD AN ELLIPSOMETRY PRESENTED: ONE THROUGH XRR, ONE EMPLOYING ELLIPSOMETRY.	75
PLOT 4.9 - THICKNESS VALUE, MEASURED THROUGH F5 INSTRUMENT FOR DEPOSITION TIMES OF DETA OF 30' AND 1H.	76
PLOT 5.1 - ATOMIC COUNT OF Pd AND Cl ATOMS AFTER PALLADIUM DEPOSITION ON LIQUID SAM.	82
PLOT 5.2 - ATOMIC COUNT OF Pd AND Cl ATOMS AFTER PALLADIUM DEPOSITION ON VAPOUR PROCESSED SAM. ..	83
PLOT 5.3 - RESISTIVITY DATA OF NiB10% PROCESSED ON PEDA LIQ 2H AND 5H.	89
PLOT 5.4 - RESISTIVITY DATA OF NiB10% PROCESSED ON DETA LIQ 2H AND 5H.	89
PLOT 5.5 - RESISTIVITY DATA OF NiB1% PROCESSED ON PEDA LIQ 2H AND 5H.	90
PLOT 5.6 - RESISTIVITY DATA OF NiB1% PROCESSED ON DETA LIQ 2H AND 5H.	90
PLOT 5.7 - RESISTIVITY DATA OF NiB10% ON VAPOUR DEPOSITED (1H AND 30') PEDA AND 30' DETA	91
PLOT 5.8 - RESISTIVITY DATA OF NiB1% ON VAPOUR DEPOSITED (1H AND 30') PEDA AND 30' DETA.	92
PLOT 5.9 - GROWTH RATE STUDY OF THE NiB 1% CHEMISTRY.	94

PLOT 5.10 - GROWTH RATE STUDY OF THE NIB 10%. THE BLACK LINES REPRESENT THE THREE LINEAR TREND LINES. 94

PLOT 5.11 - TWO EXAMPLES OF CHEMICAL TEST MADE ON THE SURFACES OF THE TWO FRACTURE PLANES. 97

PLOT 5.12 – (LEFT) SPECTRUM OBTAINED FROM THE ERD MEASUREMENT; THE GRAPH IS PRESENTED IN TERMS OF THE TIME OF FLIGHT OF THE DETACHED ATOMS FROM THE SURFACE VERSUS THE ENERGY POSSESSED. A DEPTH GRAPH (RIGHT) CAN BE THEN OBTAINED. 99

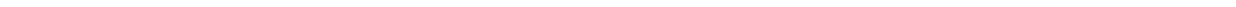
PLOT 5.13 - RESISTIVITY DATA OF THE FIRST RUN ON PATTERNED COUPONS..... 106

PLOT 5.14 - RESISTIVITY DATA OF THE SECOND RUN OF PATTERNED COUPONS (THE FIRST ONE HAS BEEN KEPT TO PERMIT A GOOD CONFRONT). 107

PLOT 5.15 - RUN 3 OF PATTERNED COUPONS..... 108

PLOT 5.16 - ELEMENT COUNT MADE BY HAADF-STEM 112

PLOT 5.17 - RESISTIVITY DATA, TOGETHER WITH THE SAMPLES STEM PROCESSED. 115



Chapter 1: Introduction

This brief introductory chapter is presented to the reader in order to allow him to familiarize with the subjects covered in this master thesis project. Three main topics will be of particular interest, which will be covered in this chapter. The first one will focus on the research field in which this work was developed: that is the integrated circuit (IC) technology; the second, on the revolutionary characteristics and properties of Self-Assembled Monolayers (SAM) and the final part of the chapter will be dedicated to an analysis of the electroless deposition of metals, in particular nickel, exposing advantages and issues of this technique.

1.1 Nanotechnology

When talking about Nanotechnology, the famous speech “There is plenty of space at the bottom”, made by Richard P. Feynman in 1959 cannot go uncited. The lecturer, during his talk at Caltech University, envisaged the possibility to create smaller and smaller machines, enabling us to manipulate the single atoms and molecules¹. The speech is often held as an inspiration for the research at lower scales, i.e. for the field of research that would later be called nanotechnology. But this word was actually introduced for the first time only in 1983 by Japanese scientist Norio Taniguchi . who gave the following definition “‘Nano-technology’ mainly consists of the processing of, separation, consolidation, and deformation of materials by one atom or one molecule”².

In the last years many definitions of nanotechnology have been proposed, mainly focusing on the possibility to nano-manipulate objects. The emphasis on this aspect is not causal: it is this that distinguishes nanotechnology from chemistry, with which is often compared. While in the latter

the motion of objects like molecules and atom is random and uncontrolled (in the limits defined by the free energy possessed by these elements) in the former a non-random *eutactic* environment needs to be available to achieve the desired control³. In this sense the US Foresight Institute gave a rather appreciated definition. According to, it nanotechnology is a group of emerging technologies in which the structure of matter is controlled up to the nanometre scale to produce novel materials and devices that have useful and unique properties⁴.

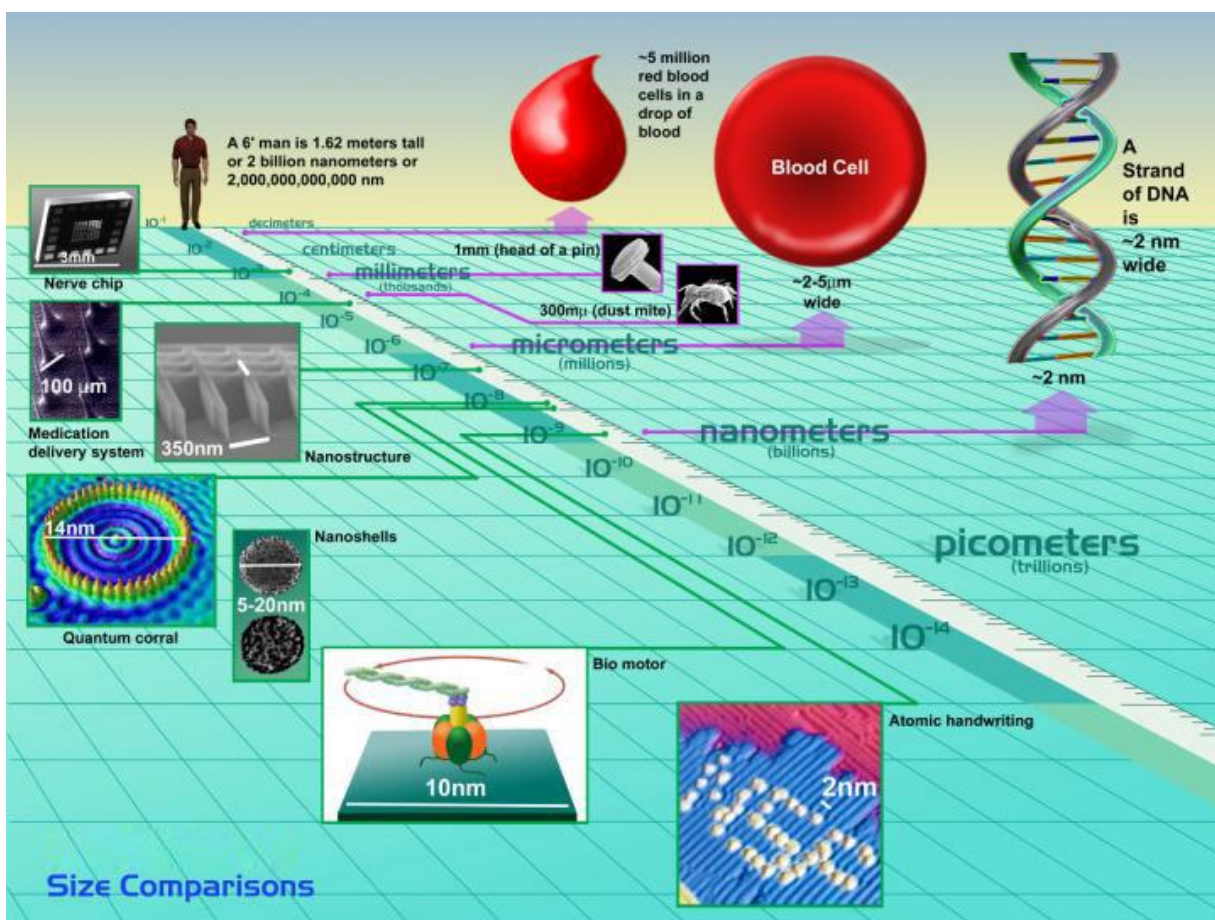


Figure 1.1 - A better understanding of the nanoscale dimension and its achievements may be achieved confronting objects present commonly in nature with hand-made ones.

One essential characteristic that should be considered and not be underestimated is the profound multidisciplinary nature of Nanotechnology. Research in some of its fields requires a deep understanding of different areas of science and technology but, at the same time, such research

promises breakthroughs in many areas, such as materials and manufacturing, medicine and healthcare, energy, biotechnology, information technology, and national security.

It is widely believed that especially Nanoelectronics will provide a fundamental shift in the way Integrated Circuits (IC) are processed and already the most recent silicon CMOS technology generation (22nm), shows physical behaviour typical of the regime of nanoelectronics. But Moore's law cannot hold forever. The capability to double the number of transistors on a chip roughly every two years is getting much more difficult now that the physical limit of materials has been reached. With a mix of chemistry, physics, biology and engineering, nanoelectronics may provide a solution to the increasing fabrication costs, and may allow integrated circuits to be scaled beyond the limits of the modern transistor⁵. If this will be the case, the goal of building microchips able to host and integrate 10^{10} devices per cm^2 by the year 2018, as estimated by the ITRS (International Technology Roadmap for Semiconductors)⁶, will be largely exceeded. A level of integration this high will, of course, be very difficult to achieve, and totally impossible if the patterning of features of this dimension will follow the existing fabrication processes. While current ICs can have almost any arbitrary pattern, nanoelectronics will likely have a regular structure generated by a stochastic self-assembly process.

This means that the components are able to guide each other in order to build structures with very little external intervention or none at all. The self-assembly capability is typical of so called "*bottom-up*" process. This term, opposed to a "*top-down*" approach, was introduced in the field of nanotechnology by the Foresight Institute in 1989 to distinguish between two different philosophies for the manufacturing of nanostructures. While the first involves the manipulation of atoms and molecules like building blocks for atomically precise nanostructures, the top-down approach is a more conventional technique which instead reaches the same goal by starting from larger pieces of materials and modifying them using large, externally controlled devices⁷. Electron beam lithography⁸, atomic layer deposition and molecular vapour deposition^{9,10}, for example, are all techniques involving some kind of nanomodification of matter. These are bottom-up

techniques largely used today in many engineering fields. Self-Assembly Monolayers (SAM) also have shown promising properties with their tuneable properties. Instead a commonly used top-down technique is dry etching of bulk materials, useful in the creation of circuits on the top surface of silicon microchips¹¹.

Nanoelectronics and, more widely, Nanotechnology have the potential to deeply change everyday life in ways that today cannot be predicted, while the numbers of fields where nanotechnology will be employed will largely increase along with the decreasing of technology prices.

1.2 Copper interconnect technology

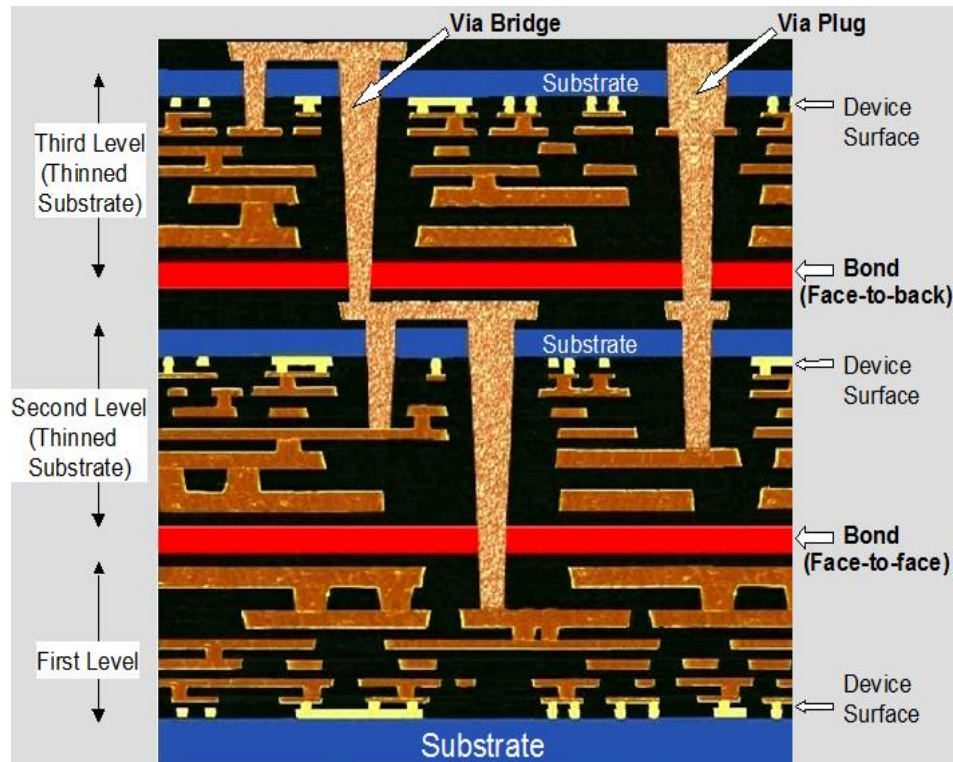


Figure 1.2 - Schematic cross section of an integrated circuit, which shows that the metallic interconnects are mechanically supported and electrically insulated by an inter-level dielectric (ILD).

Interconnect technology represents an area of electrical engineering regarding the metallization process necessary to produce electrical conductive lines for the interconnection of the individual semiconductor devices as shown in Fig. 1.2.

An overview of how interconnections are produced, which materials are employed and how these have been developed, will be given in the following paragraphs.

1.2.1 The Damascene Process

Copper has represented the fundamental material for the realization of interconnections in semiconductor integrated circuits since 1997¹². Previously, the lack of volatile Cu compounds made patterning procedures practically impossible, consequently making aluminium the best choice from the start of the IC industry. The destiny of aluminium was anyway already foreseeable: copper wires conduct electricity with about 40 percent less resistance than aluminium wires, which results in a 15 percent burst in microprocessor speed due to the decrease of RC delay, which, in turn, increases the IC speed. Copper wires are also significantly more durable and 100 times more reliable over time, and can be shrunk to smaller sizes than aluminium. Also copper gives the possibility to add more layers of interconnections by introducing new manufacturing technologies.

Replacement of aluminium with copper represented a big challenge for semiconductor engineers. Aluminium can be deposited over the entire wafer surface and then patterned by reactive ion etching (RIE), while all efforts to apply the same process on copper failed. Since copper cannot be patterned, a new approach had to be developed in order to have a good filling of the patterned dielectric layers.

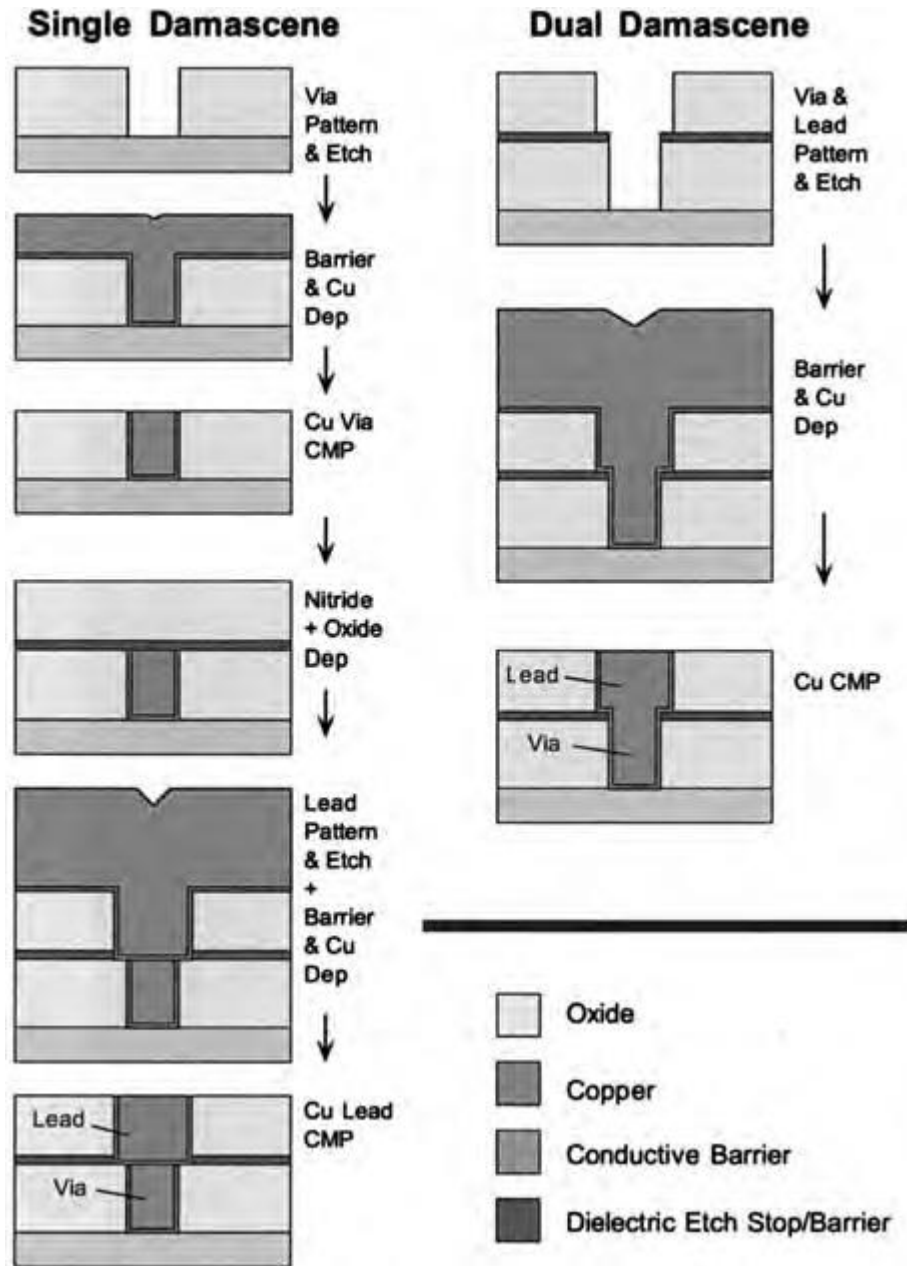


Figure 1.3 - Cu-damascene process flow: the differences between Single and Double Damascene processes are quite evident from the picture as much as the lower amount of steps in the DD one.

Various forms of PVD (sputtering, deposition etch, electron cyclotron resonance) as well as CVDs were examined initially¹³. A sub-conformal deposition of the metal in the trenches or vias, responsible for the formation of voids and seams, was the main reason the processes were abandoned¹⁴. At the end of the century, copper *Damascene* processes were introduced and the

century-old chemical mechanical polishing (CMP) procedure was renewed to integrate copper in deep sub-micron level circuitry. Superfilling, which refers to a filling process where a higher deposition rate is achieved at the bottom of the trench or via, with respect to the sides, resulting in a void-free filling, played a pivotal role in the success of this technology¹⁵. The damascene process can be either a *single Damascene (SD)* or a *dual Damascene (DD)*, as can be seen in figure 1.2. The difference between the simple SD process and the DD process is that in the DD process one metal deposition step and one CMP step are eliminated (as well as the dielectric deposition step). The reduction in the number of processing steps made DD more attractive than its twin single Damascene process.

Both SD and DD processes consist of 3 main steps (figure 1.3):

- 1) In the first step, the dielectric is completely patterned and a barrier layer such as Ta or TiN is deposited in order to prevent interaction between the substrate and the upcoming copper layer. A copper seed is then deposited over the barrier layer: good step coverage and uniformity is essential to avoid defects in the next step.

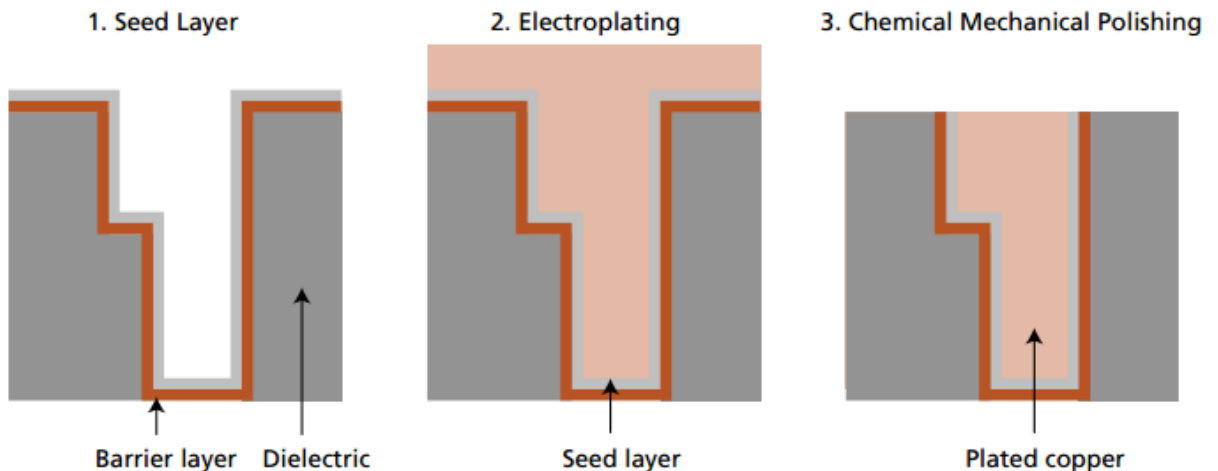


Figure 1.4 - Dual Damascene process steps

- 2) Electroplating (or electrochemical deposition ECD) is normally employed to completely fill the pattern. A reliable ECD process is highly dependent on the previous lithography, etching, barrier layer and seed layer deposition steps.

- 3) The chemical mechanical polishing (CMP) step is essential to remove excessive copper, due to the impossibility for it to be etched away. CMP is able to provide globally planar surface but only if the original topography is amenable to global planarity. It consists of a synergistic process that removes material through a mechanical action of a solution (*slurry*) containing abrasive particles like silica and alumina, while a chemical attack is carried out by the hydrogen peroxide contained in the slurry that manages to oxidize the metal layer^{16,17}.

The patterning of the dielectric is normally made through the formation of a cap layer (constituted of silicon compound, Si_xN_y normally) which is, in turn, coated with a photoresist material and patterned through the lithographic step. Anisotropic etching is then able to cut through the surface hard mask (plasma Si_xN_y is often employed) without attacking the underlying substrate thanks to an embedded etch-stop layer.

The ability of the CMP to stop the planarization once the dielectric layer has been exposed, with the possibility to remove the copper in a planar fashion, leads to the realization of successive layers of insulator and copper, creating a multilayer (more than 10) interconnection structure.

Five different DD processes were studied over the last few years. Nowadays only two are currently in mainstream production: *embedded-via first* and *embedded-trench first*. The difference between them is the way the etching step is carried out. In the first case the etching attacks both layers on which the DD process is done. A second etching is made on the top layer that has been previously coated with photoresist. In the *embedded-trench first* approach the etching phase attacks one layer at a time. The major drawback in this case is that, after the trench is etched, the photoresist that is applied for the via-step will completely fill the feature. As a result, the PR can be said to be *pooled* in the trench, leaving an extra thick resist layer right in the area where via holes are to be patterned. This creates a difficult situation to fabricate fine structures for via holes. For smaller trenches the *embedded-via first* approach has been widely accepted in industry¹⁸.

Figure 1.4 shows a double damascene unit with different materials embedded in the structure. As a whole, the damascene architecture has introduced borderless contact via, a decrease in process induced damage regarding the front end part of the line, which addresses soft plasma processes for either dry etching, cleaning or material deposition, improvement in performance (speed) of the devices and fine line structure. As a matter of fact, copper damascene processes can fabricate Cu-interconnecting lines less than 1/1000th of the width of a human hair.

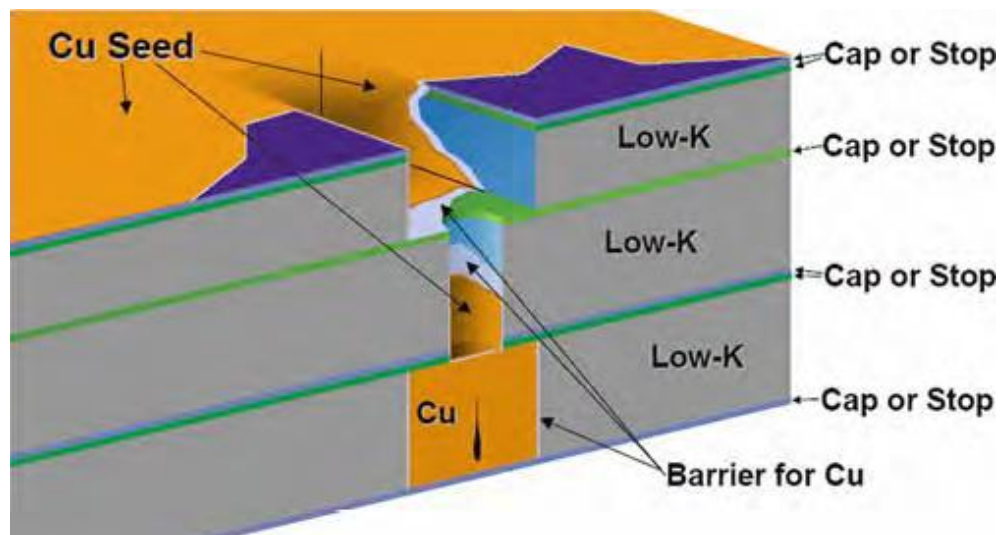


Figure 1.5 - A dual damascene architecture showing the different materials in the unit structure

Today the electronic industry is preparing to launch the new 14 nm technology node that is going to make the 22 nm one, introduced in 2012 already obsolete¹⁹. The development of high-performing sub-22 nm devices brings new, greater and more numerous challenges in the coupling of low K materials and metals. Incorporation of new nanotechnologies like the use of self-assembled materials, 3D integration, spintronics or molecular electronics in interconnect architecture is essential to continue on the road of miniaturization. Even then, new challenges will be emerging that will lead to the modification of the known technologies to achieve the ultra-high performances of wiring systems so essential in today's IC development.

1.2.2 Issues in Cu interconnections

In the previous chapter we described how the deposition process had to be rethought after the revolution from an aluminium based industry to a copper based one. Apart from the absence of volatile compounds, formerly mentioned, there are several other difficulties encountered in the use of Cu interconnect. The issues are mainly caused by some peculiar chemical and mechanical properties of copper. It is worth mentioning, for example, that copper does not form a stable oxide, as instead aluminium does. Also, in contrast to other three-dimensional (3D) transition metals, Cu has a very high diffusivity in silicon (diffusion coefficient $D = 3 \times 10^{-4} \text{ cm}^2/\text{s}$)²⁰, due to its small atomic radius and weak interaction with the silicon lattice. Furthermore copper interacts strongly with silicon, forming silicides (Cu_3Si) starting from 200 °C, modifying its atomic structure²¹.

Copper diffusion normally happens through the migration of its ions Cu^{+} , which is enhanced by the presence of applied currents²². Instead the formation of copper ions is enhanced by a series of factors like high humidity, presence of impurities on the top surfaces and/or in the bulk of the dielectric material²³. The presence of copper in silicon oxide impacts the function of the active elements by creating short trap state or causing shortcuts in case of agglomeration²⁴. Moreover copper shows low adhesion on underlying silicon oxide layers due to the difference in the free energy of formation of copper oxide against that of silicon oxide. The oxide is normally formed by a combination of CuO and Cu_2O and, as already mentioned, these oxides present very different properties with respect to alumina, Al_2O_3 . While alumina provides very good protective properties for aluminium technology processes, copper oxides show completely opposite properties.

A *cap layer* has been used, since the birth of copper interconnect technology, to avoid oxidation, corrosion, interface diffusion and other issues in copper. A *barrier layer*, sandwiched between copper interconnections and the dielectric layer, was instead introduced to prevent chemical contact between the dielectric materials and copper.

1.2.3 Requirements for barrier layers

An ideal barrier layer should provide an insurmountable boundary between copper and the dielectric layer. This implies that crystalline materials should be avoided, due to the presence of faster diffusion paths like grain boundaries. As a general rule, the higher the crystallization temperature the higher the diffusion-blocking of the material²⁵ will be. Crystalline materials may be employed if grain boundaries are avoided (impurity atoms like O, N, C, Zr are useful in this sense) or if they are present but their directionality is perpendicular to the film surface. A basic requirement for barrier/interconnects stack is to show a resistivity as low as possible: the presence of the barrier layer will surely cause a decrease in the net cross-section occupied by copper, resulting in a higher resistivity of the line or via. It is important then to scale down the barrier films, even more so, since the copper lines are undergoing a shrinking process.

Figure 7.4 shows how the resistivity changes by varying the thickness of some of the commonly used barrier layers (b) with the ITRS (International Technology Roadmap for Semiconductors) requirements, and (a) a schematic of the effective resistance of the copper interconnect in a line and in a via.

The bonding properties between the dielectric layer and copper have to be necessarily improved for reliability issues, in particular to their electromagnetic behaviour. The formation of a strong interface is important from the standpoint of adhesion between the different layers, reducing the risk of crack propagation²⁶.

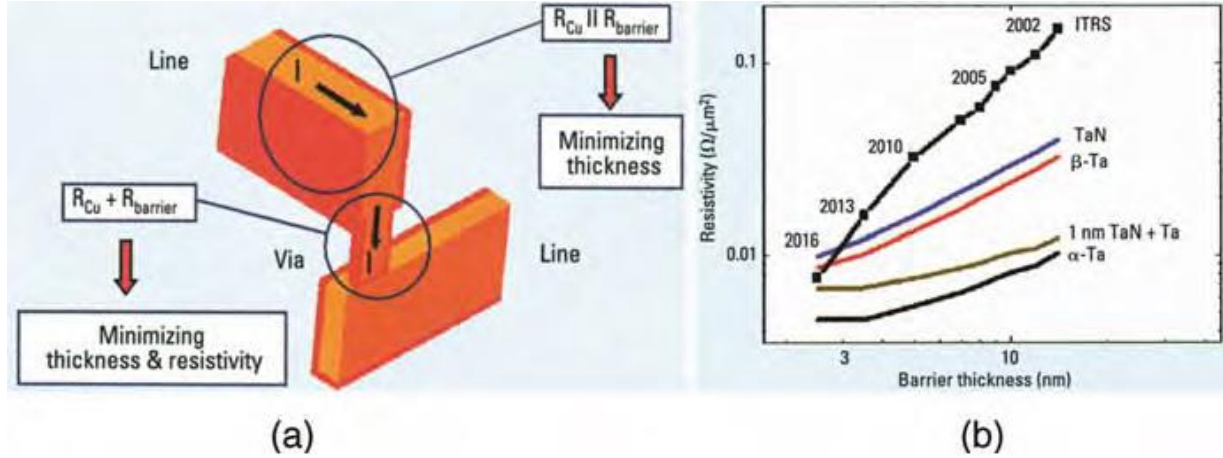


Figure 1.6 - (a) Schematic of the effective resistance of a Cu interconnect and (b) variation of resistivity versus the thickness of the barrier layer

Also the wetting capability of the barrier film with respect to the liquid metal should be considered. A good wetting will provide low roughness and will affect the crystallographic orientation of the growing layer. Last, but not least, thermodynamics and kinetics have always to be taken into account to foresee possible undesired reactions between different layers¹⁸.

1.3 Barrier Layer State of Arts

A conventional barrier layer in advanced ULCI metallization is normally composed of a bilayer of tantalum (Ta) and tantalum nitride (TaN). The implementation of a double Ta/TaN_x was first introduced in reference²⁷. Such structure is able to adhere very well to the substrate through the strong TaN_x/SiO₂ interface, whereas the Ta has a high adherence towards the metal layer. The bilayer is also characterized by a thermal stability that is at least as high as the most stable single layer²⁴. With a density of 16.3 and c/a 6.5 g/cm³, the double film can reach values of copper diffusion coefficient higher than $2 \cdot 10^{-14}$ cm²/s and avoids the formation of copper silicides up to 700 °C. The deposition was carried out through a double process: PVD for the Ta layer and ALD for TaN_x. At the present day a PVD process is successfully employed for both films.

The described structure and processing is not free of issues. It is expected that these barriers, together with the PVD copper seed layer, will not be able to meet the future technology requirements. A thinner and continuous copper barrier/seed with good step coverage and no overhang for excellent copper gap fills is necessary as the dimensions of the trench or via hole shrinks and the aspect ratio increases²⁸. The PVD process does not maintain these requirements for barrier layers thinner than 5-6 nm and furthermore it shows an excessive resistivity compared to that of copper ($\rho_{TaN}=350\mu\Omega\cdot cm^{29}$).

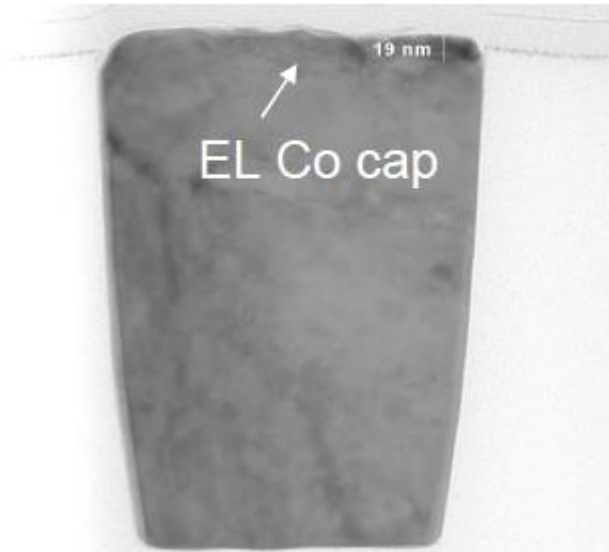


Figure 1.7 - TEM cross-section of an ALD TaN barrier and Co cap layer³²

Therefore a radical improvement of the PVD Ta/TaN_x process or a change in the used materials or deposition modes is expected in order to meet the new interconnect size as well as good barrier layer characteristics.

Techniques like advanced PVD (ENhanced COverage Resputtering), CVD and ALCVD (Atomic Layer Chemical Vapour Deposition) have demonstrated better conformality characteristics than traditional PVD^{30,31}. A lot of effort has been made in recent years to implement Atomic Layer Deposition (ALD) in order to overcome the deposition issues of PVD, especially conformality and thickness³². ALD presents many similarities to PVD, like the use of gas precursors, but shows interesting differences. In particular the self-limiting character of the process can be exploited to achieve high uniformity deposits also in narrow trenches, holes and vias. Different compounds can be deposited with this technique, especially transitional metals and their nitrides (Ta, Ti, W)³³.

Pressure is today being put on new *ultra-low-k* materials to reduce the *RC delay*, in order to achieve high speeds in nanoscale circuits³⁴, for future scaled down interconnect technologies.

Porous low-k materials have been under study in recent years as a new class of materials able to meet tighter requirements. These materials present new issues that have to be compensated by the barrier layer^{30,35}. Low mechanical strength, porous sidewalls of vias and trenches will be present if conventional PVD is used.

As we will see in the next paragraphs, Self-Assembled Monolayers (SAM) alternative barriers, even if presenting similar principles to ALD precursors, offer interesting advantages. No strict need of vacuum, single cycle deposition for the achievement of conformal, near-zero thickness layers, even at room temperature and pore sealing characteristics can be achieved by tuning the SAM precursor structure³⁶.

1.4 Self-assembled monolayer (SAM)

The term Self-Assembly Monolayer (SAM) has been cited earlier in this work without providing a good explanation of its meaning. This paragraph will provide the reader with a good insight in the SAMs original and novel properties.

A self-assembled monolayer is an ordered thin layer, formed by organic molecules able to auto-arrange spontaneously in an ordinate manner on top of appropriate substrates with which it normally has a strong interaction³⁷. Complex hierarchical structures can be formed from small building-block, involving multiple energy scales and degrees of freedom³⁸. As already said in paragraph 1.1, the self-assembling ability of SAMs allows them to be considered a typical “bottom-up” approach.

Organic films have always captured the attention of many scientists for centuries due to their particular behaviour. Already Benjamin Franklin more than 200 years ago studied the calming influence of oil on water waves³⁹. In the 19th century, Pockels prepared monolayers at the air-water interface⁴⁰⁻⁴², followed by the works of Rayleigh⁴³, Hardy⁴⁴ and others. The first to actually

study self-assembled monolayer was I. Langmuir, who in 1917 published the first work on what would later be, in honour of his work, called Langmuir films⁴⁵. The concepts were extended a few years later thanks to the help of K.B. Blodgett, who studied the deposition behaviour on solid substrates (for the first time) of carboxylic acids⁴⁶. Their combined work led to the introduction, for the first time, of the concept of monolayer and the two dimensional physics which describes it. In 1946 the work by Zisman led to the discovery of the self-assembling characteristic of some of these molecules thanks to their spontaneous chemisorption on the surface⁴⁷. No great interest was given to SAM until the 80s and 90s. Their ability to self-assemble, and therefore to produce atomically precise and relatively cheap films and nanostructures has gained large interest in many fields like electronic devices, chemical and biological sensors and coatings, as attested by the increasing number of publications over the last 20 years (figure 1.6). Apart from the pure curiosity factor that has historically characterized research on amphiphilic monolayers, SAMs are particularly attractive for the following reasons:

- the ease of preparation;
- the tunability of surface properties via modification of molecular structure and functions;
- their use as building blocks in more complex structures, e.g., for "docking" additional layers to a surface;
- the possibility of lateral structuring in the nanometre regime;
- the applications made possible by these features³⁸.

In addition, these materials often exhibit optical, electrical, optoelectronic, mechanical, chemical, or other properties which are not obtainable with inorganic materials.

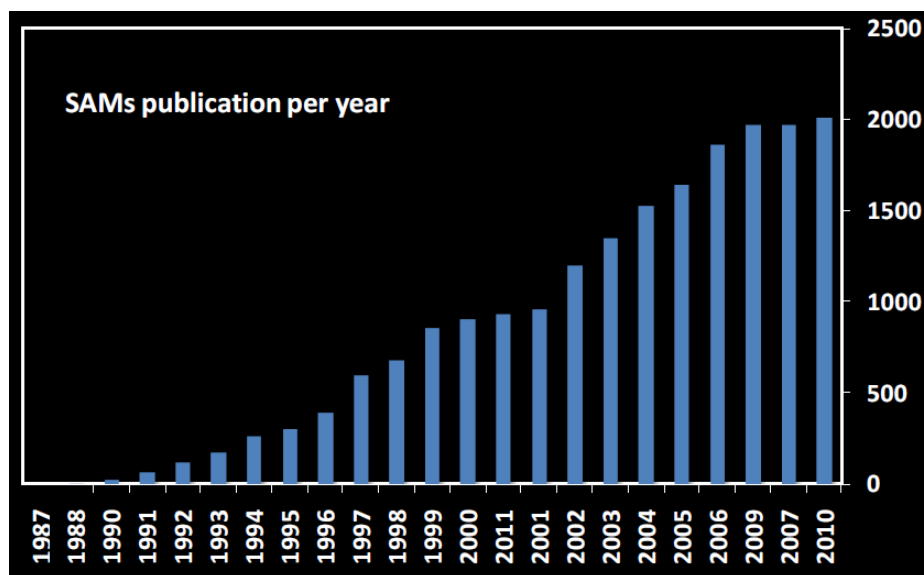


Figure 1.8 – Publications regarding SAMs from 1987 to 2009

The ability to spontaneously form assemblies arises from their unique amphiphilic chemical structure. In fact, self-assembled molecules are typically composed of two groups: a *head group*, chosen correctly to have high affinity to the appropriate substrate, and a *tail group*, which is able to completely modify the interfacial properties of the system. The *backbone*, connecting head and tail of the molecule, may be considered a third functional group, because of its ability to modify the SAM's properties. Figure 1.7 (a) gives an accurate representation of the different parts of a SAM precursor molecule. When such molecules are brought in contact with a surface, acting as a substrate for the deposition, the head group of the molecules will tend to be physisorbed and/or form a chemical bond to the surface (chemisorption), anchoring the molecule to the substrate. Furthermore, as the number of molecules bonded to the substrate increases, the backbone will tend to tilt of a certain angle ϑ , bringing the tail group closer to each other. The decrease in free volume and the rising van der Waals forces between closely packed molecules cause a reduction of the free energy of the system⁴⁸ making the process thermodynamically favourable.

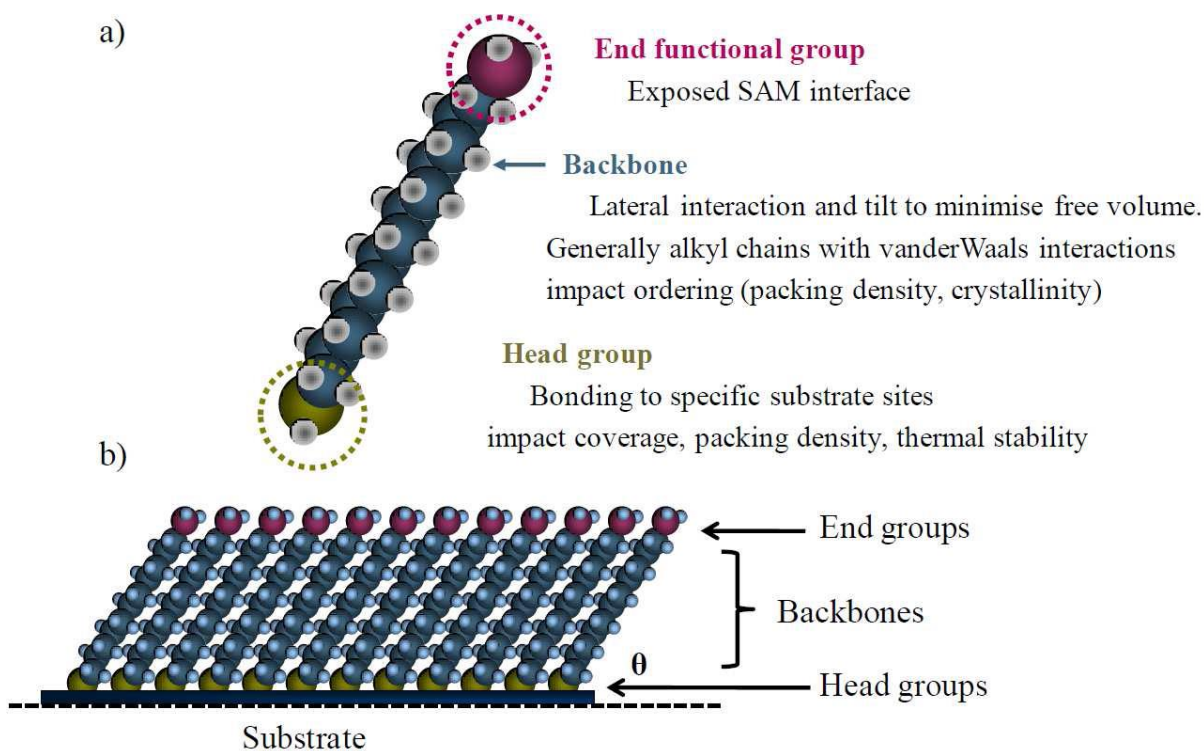


Figure 1.9 - a) Representation of a surfactant molecule with the three main parts composing it (head, backbone and tail). b) Schematic of a self-assembled monolayer on a substrate.

The possibility to tailor head and tail groups of the constituent as needed enables an accurate design of the surfaces and interfaces and the selective deposit of SAMs on a specific substrate. End groups can be chosen to allow for further physical or chemical functionalization essential for the employment of SAMs as intermediate layers for successive depositions⁴⁹. We can add hydrophilic end groups (i.e. $-\text{OH}$, $-\text{NH}_2$, $-\text{COOH}$) or hydrophobic ones ($-\text{CH}_3$) to vary the wetting of a substrate and the interfacial properties of it. On the other hand an appropriate head group can be selected in order to react with the substrate. Since the head group has to be selected wisely considering the chemical functional group defining the substrate (while the rest of the molecules can be almost freely chosen), this “chemisorption pair” is used to classify the specific system in the following³⁸. One of the most popular is probably the group of thiols ($-\text{SH}$): they have high affinity with metal substrates like Au^{50} (111). Alkoxy ($-\text{Si}(\text{OCH}_3)_3$) and trichlorosilans ($-\text{SiCl}_3$) groups instead react with oxidized substrate. Because of the reactivity of the alkoxy and chloride groups with the hydroxyl groups present on semiconductor silicon and insulator silica surfaces,

alkylalkoxysilanes and alkyltrichlorosilanes are of particular interest for technological applications, for example, in the MEMS field⁵¹⁻⁵⁴ for antistiction purposes. The importance of the backbone should also be stressed: the alkyl chain that links head and tail makes a significant contribution to the mechanical properties of the SAM. A major issue with chlorosilanes is the possibility to react with the substrate as well as with each other, in the bulk of the solution, before they actually manage to reach the substrate⁵⁵. On the other hand organosilanes do not polymerize in solution, but bring other complications: head groups are larger because of the presence of typically three silanol groups, they require the presence of water in the medium as a condition for the deposition and the formed bonds are normally irreversible.

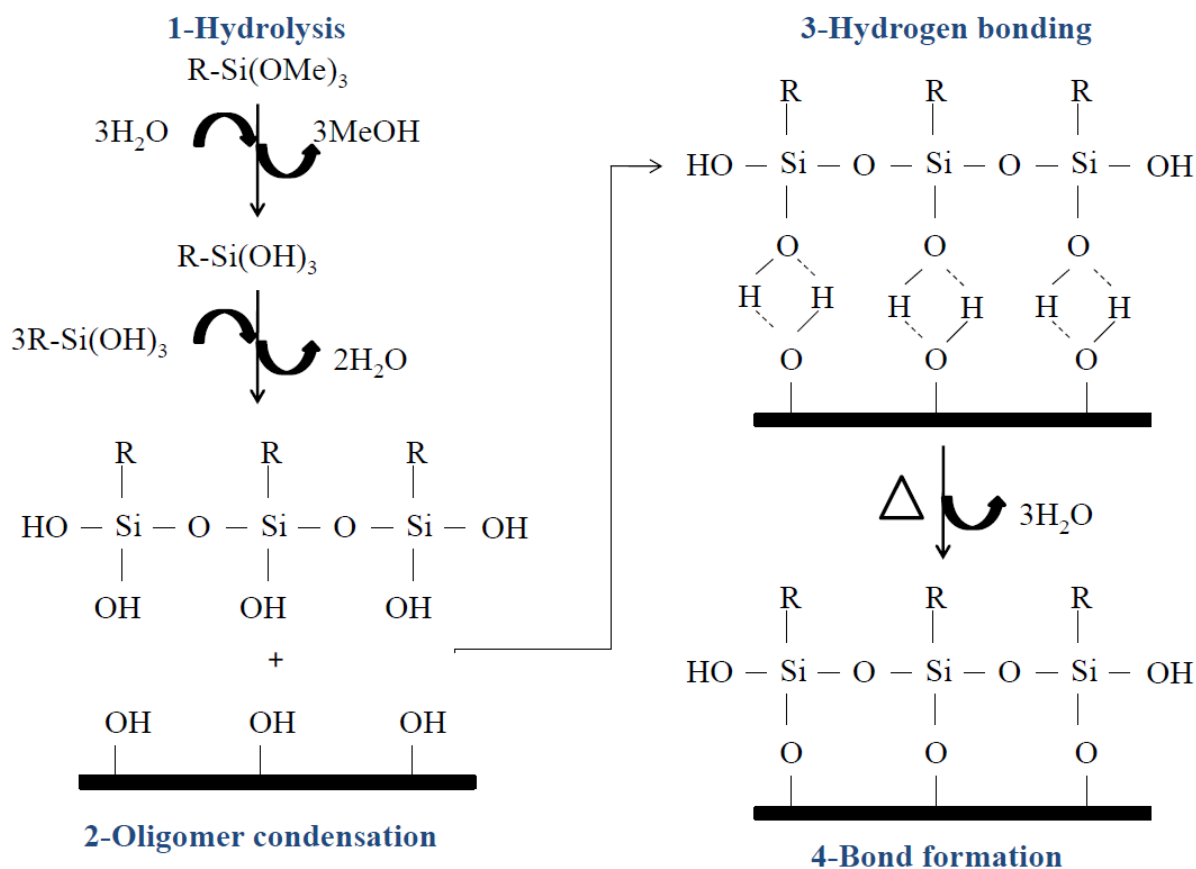


Figure 1.10 - Schematic of the reaction between a trimethoxysilane molecule and a hydroxyl-functionalized structure. The processes can be summarized in 4 steps: Hydrolysis of the methoxy group, condensation of the molecules in oligomers, formation of weak H-bonds and the final formation of the monolayer.

Still Alkylsilane-based SAMs are very interesting for microelectronics because of the possibility to be grown from solution⁵⁶ but also through gas-phase deposition^{57,58}, giving interesting possibilities for easy integration on 300 mm wafer. It must be underlined that SAM formation process is still not fully understood: it can be anyway taken for granted the importance of the water layer adsorbed into the surface for the adsorption of the molecules before the formation of the chemical bonding^{59,60}. A schematic representation of the process is illustrated in the figure below.

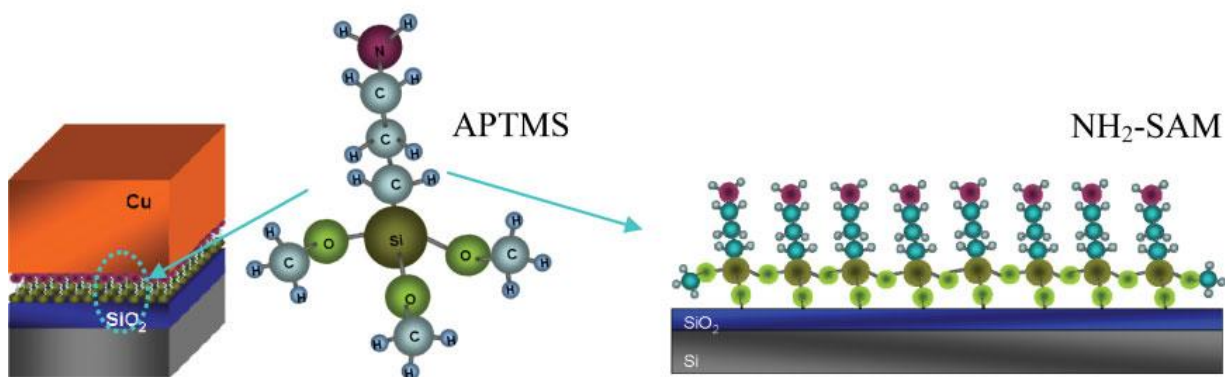


Figure 1.11 - Representation of an amino-SAM (APTMS) used as a barrier layer for successive copper deposition

1.4.1 SAM as advanced barrier layer in interconnect technology

We described, in a previous paragraph, how scaling of the feature size has brought many new and harder challenges in the IC industry over the last decade. Within the new technologies that were proposed as alternative diffusion barrier layers, the employment of SAM emerged. The first study on the use of SAMs to stop interdiffusion of copper in the dielectric layer was published by A. Krishnamoorthy *et al.* in 2001⁶¹. In the report the characteristics of 4 different SAMs were studied as new, ultrathin barrier layers (≤ 2 nm thick), to prevent the diffusion of Cu in the lower dielectric layer. Results were then compared to two, at the time, state-of-art Ta and Ti based barrier films with thicknesses ranging from 10 to 30 nm. The 4 SAMs molecules used as precursors

had different chain lengths and end groups, while the methoxysilane group, used to anchor the molecule to the substrate remained unchanged. Conclusions were promising; it was established that the inhibition effect of the diffusion of copper was caused by the presence of the SAM or, at least, the time to failure was increased and the chain length and terminal group of the precursor were able to modify these performances.

It should be noticed that until 2001 self-assembled monolayers were gaining interest in many applications both in and out of the IC field (anticorrosion coatings, patterning, etc.)⁶², e.g., also in 2001, M.M. Sung *et al.* published a paper regarding the use of thiols on copper with similar properties as the ones assembled on gold⁶³. In 2003 Ramanath *et al.* compared some SAMs, among which the one used by Krishnamoorthy *et al.*, where) with the Ta/TaN conventional barrier film, showing lower performance of the SAMs in terms of extrapolated mean-time to failure⁶⁴. MPTMS (containing a mercapto-, SH-, group) became used in the later years as a diffusion barrier and as adhesion enhancer factor at the Cu/SiO₂ interface⁶⁵. New SAMs started to undergo through testing: in 2004 Ganesan *et al.* utilized amino- and carboxy- terminated precursors for the same purposes as before, assessing better behaviour for the latter⁶⁶. First use of SAM barriers in IC-like structure was shown by Gandhi *et al.* in 2007, who studied the effect of different monolayers in single damascene structures⁶⁷. Also, in a successive publication, Gandhi *et al.* demonstrated the positive effect of curing the SAM at high temperature after deposition to increase adhesion properties⁶⁸.

It should be noticed that until 2008 no coupled characterization in terms of adhesion, process stability and reliability and film properties were conducted. A publication by Caro *et al.*, reported the results of research conducted in imec laboratories about a screening made on precursors with different head groups (methoxy-, chloro- or mixed) with different chain lengths and tail groups (amino-, bromo-, ciano-, mercapto-, methen-). The paper concluded that different groups and chain lengths could heavily modify the properties of the growing SAM, and that the amino-terminated one, made by 3-APTMS (aminopropyltrimethoxysilane), was the most promising as an inhibitor for Cu diffusion^{36,69}. Since then many different papers, screening different SAMs, have been successfully published. These studies have concluded that SAMs can be used as a barrier layer, providing an interface toughening mechanism at copper/silica interfaces, tailored with organosilanes. But SAMs have been proved useful not only as alternative barrier layers but also for the improvement of copper deposition techniques like PVD, CVD and ElectroLess Deposition (ELD).

In the last years imec research has gone towards the development of barrier properties of amino-terminated groups, especially APTMS, resulting in publications^{70,71}, along with the implementation of these new deposition techniques, trying to solve PVD limitations. This is the starting point of this research project^{36,72}.

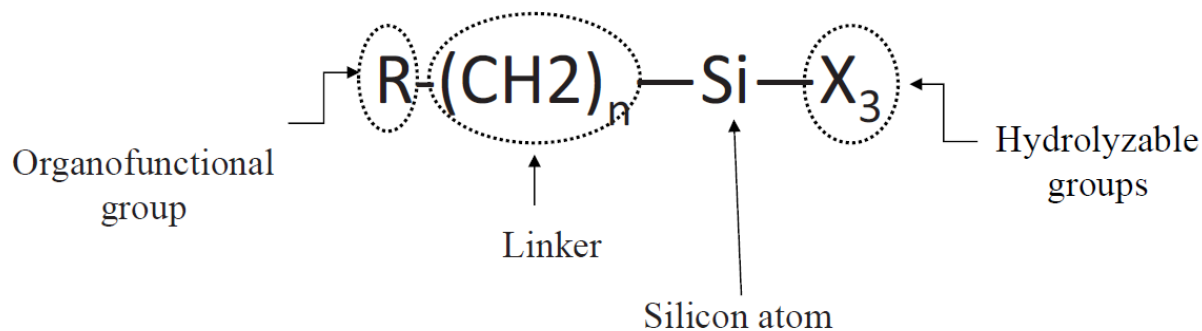


Figure 1.12 - Model of a Silane molecule: all the molecules in this group have in common the silicon atom, uniting the hydrolysable groups and the backbone.

1.4.2 SAM deposition techniques

Several kinds of SAMs deposition processes have been studied since their discovery. Of all of them especially the vapour-phase and liquid-phase deposition have been intensively used. Others, like spraying or spin-coating, are sometimes used for special applications.

1.4.2.1 Liquid deposition

Probably the first deposition technique employed, liquid-phase assembled of organic molecules is still the most widely used. It has been widely studied in the past three decades so the reaction mechanism has been quite well understood. The liquid is very useful to provide an effective medium to allow the SAMs precursors molecules to reach the substrate and react on and with it. Different liquids can be used as deposition mediums other than water; organic solvents like alcohols and toluene are largely used. An advantage of the wet process is the effectiveness at room temperature, without need of vacuum formation. However it has been demonstrated that the film quality can vary with the deposition temperature⁷³. The technique suffers from sensitiveness to humidity present in the ambient and polymerization of the precursor that may create particulate over the surface⁵⁵. Also the solvent has to be chosen wisely to avoid the deposition of multilayers.

1.4.2.2 Vapour deposition

Vapour deposition has acquired interest in the recent past especially for industrial applications. It represents a typical example of CVD, where the precursor is heated up at temperatures higher than 100 °C. The SAM in a liquid phase is deposited in a reservoir and, once the temperature has reached an optimal value, it evaporates, reaching the nearby substrate. Pressure is kept low: the reaction chamber is normally kept near vacuum conditions and increases when the SAMs

precursor evaporates (vapour pressure around 5 torr). The process can be carried out at lower temperatures (50-120 °C) if the reservoir consists of the SAM precursor diluted in a solution. Still adequate vapour pressure of the precursor has to be reached to have a correct deposition. Vapour deposition is useful in avoiding undesired side-reactions and favouring a monolayer deposition. The mechanism of deposition is still not perfectly understood but studies have confirmed that SAMs deposited with liquid and vapour process maintain comparable properties⁷⁴. The industrial interest in vapour deposition is justified by the previous cited advantages over the liquid one but mainly because of the easier and less numerous process phases. Liquid deposition involves a high number of rinsing and cleaning steps not necessary with vapour deposition, making the latter very attractive under the scaling-up point of view.

1.5 Electroless Deposition (ELD)

Electroless deposition is a process that, although not recognized as such, has been used in practice for centuries, even if only in the last 50 years important scientific results have been achieved⁷⁵. This became possible after the discovery of its working mechanisms by Dr. Abner Brenner and Grace Riddell at the National Bureau of Standards, where they accidentally observed that the additive H_2PO_2 caused apparent cathode efficiencies of more than 100% in a nickel electroplating bath. This led them to the correct conclusion that some chemical reduction was involved. It is defined as a nonelectrical plating of metals and plastics to achieve uniform coating by a process of controlled autocatalytic (self-continuing) reduction. It involves deposition of many different metals such as silver, gold, palladium, nickel, copper or alloys of these metals plus P or B by means of a reducing chemical bath.

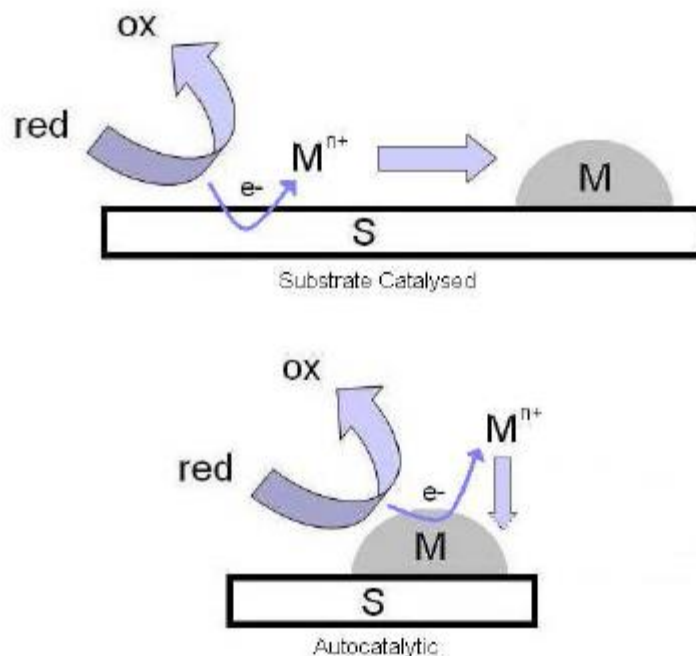


Figure 1.13 - Electroless deposition process schematic. Up: the reaction is catalyzed by the substrate. Down: the reaction is catalyzed by the deposited metal.

The name *electroless* can be somehow misleading. There are no external electrodes present in the bath, so no external electric field is applied, but still there is transfer of charges (electric current) involved. While in a typical electroplating process an anode connected to an external power supply provides the metal ions necessary for the deposition, here the metal is supplied by a metal salt dissolved in the bath. The cathodes role is instead taken on by the substrate while a chemical reducing agent provides the electrons necessary for the reaction. A great advantage of ELD over electroplating is due to the possibility to deposit metals even on nonconductive surface, as well as metals and semiconductors.

The process can be easily understood by looking at the schematized version in Fig 1.9.

The metal ion oxidizes on top of the substrate to form a metallic layer. This is possible thanks to the electrons provided by the reducing agent made available due to the passage from a reduced state to an oxidized one. In many cases the substrate is not able to catalyze the reaction. In this

case normally noble metal nanoparticles, already present on the substrate at the entering of the ELD bath, are used to start the reaction. Once the reaction has started their role is no longer important because it's the same metal that catalyzes the reaction. This explains the autocatalytic nature of the process.

A typical electroless solution is made by a blend of different chemicals, each of them performing an important and exclusive function. This includes:

- a source of metal ions
- the reducing agent
- complexing agents
- stabilizers
- inhibitors
- energy

1.5.1 Metal Ions Source

As already said, metal ions come from a salt dissolved inside the solution. Most commonly used salts belong to the sulphate family, like nickel and copper sulfates. The choice is due to the non-deteriorating capabilities of the bath by the sulphate groups remaining in the bath after the reduction of the metal on the surface. Other precursors include also metallorganic molecules like nickel acetate or chloride compounds, used for more specific applications⁷⁶.

1.5.2 Reducing Agents

The metals most commonly deposited by electroless deposition are shown in table 1.1, along with commonly used reducing agents. Since the role of the reducing agent is to supply electrons, all

the listed species have similar structures in that they contain a certain number of reactive hydrogen atoms. The catalytic dehydrogenation of the reducing agent is responsible for the metal reduction.

Table 1.1 – Reducing agents commonly used in ELD processes.

Reducing agents for Electroless plating processes	
Sodium Hypophosphite - NaH₂·H₂O	Ni, Co, Cu, Pd, Ag
Sodium Borohydride - NaBH₄	Ni, Au, Co, Cu, Ag
Dimethylamineborane - (CH₃)₂NH·BH₃	Ni, Co, Cu, Ag, Au, Pd
Hydrazine - H₂N·NH₂	Ni, Pd, Au
Formaldehyde - HCHO	Cu, Ag

The metal deposition can then be understood as a sum of two electrochemical reactions (an oxidation and a reduction) happening inside an electrochemical cell, with a consequential liberation and consummation of electrons

The general reactions are:

Reduction of a metal ion

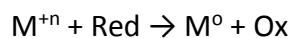


Oxidation of the reducing agent



Resulting in:

Overall Reaction



The overall reaction can be derived through a simple sum of the two redox semi-reactions and gives an idea of the stoichiometric reactions occurring during the metal deposition. However the complexity of the reactions and of the other phenomena that take place inside the electrochemical bath is much higher than the situation described by the chemical equations⁷⁶. Hence, it is necessary and convenient to study the mechanism occurring for the salt and reducing agent we are interested in.

1.5.3 Complexing Agents

Over the decades many different additives to the plating bath have been developed. One family is referred to as complexing agents. Formed mainly by organic acids or their salts (important exceptions are the ammonium ion and pyrophosphate ion) they play three roles:

- Help maintain a stable pH level
- Prevent nickel salts precipitation
- Reduce the presence of free metal ions⁷⁷

The complexing agent acts by displacing the water molecules around the metal ion to form a metal complex. The chemical properties of the metal ions in the aqueous solution are then altered, affecting among many, the colour of the plating solution and most importantly the driving force for the reduction⁷⁶, as described by Nernst's Law. The rate of the metal deposition is in practice then proportional to the rate at which the metal-ligands bonds are broken and so inversely proportional to the strength of the bonds. ELD is then described more effectively by mixed potential and bath stability, while the reaction rate is heavily affected by the pH of the bath⁷⁸ because of its influence on the ΔE° of the reducing reaction⁷⁹.

1.5.4 Additives

Under the name additives there are a high number of different compounds used in chemical baths in order to increase the lifetime and stability of the solution.

Stabilizers are used in order to avoid a decomposition of the plating solution, which can happen at any time. Decomposition comes normally along with an increase in the volume of hydrogen gas evolved, that causes the formation of a fine black precipitate through the bulk of the solution giving it a much darker colour. This precipitates are formed by metal salts, depending on the metal plated and on the reducing agent used. Stabilizers are able to prevent or retard this homogenous reaction, giving the possibility to use the bath for a long period, and in the meantime also accelerate the plating process. Four “classes” are normally used as stabilizers:

- Compounds based on IV group elements (Te, Se, etc.)
- Unsaturated organic acids (maleic acid, etc.)
- Heavy metal cations (Sn^{+2} , Pb^{2+} , etc.)
- Compounds containing oxygen (AsO_2^- , MoO_4^{2-} , etc.)

For a correct usage of stabilizers there must be a precise identification of the issues that can be solved by the stabilizers. Secondly the compatibility of the stabilizers with the other chemicals employed in the bath must be assessed: synergistic action with other additives could cause a loss in catalytic activity. Finally the additives must not inhibit or lessen the effectiveness of the other stabilizers present^{76,77}.

Another family of additives is known as buffers. Buffers are substances used to avoid a relevant change in pH towards more acidic or basic one. They normally act by reactions that consume or reduce protons or hydrogen ions in the bulk of the solution or close to the plated surface. Better is the buffer and higher must be the quantity of acid (or base) necessary to give the same change

in the pH of the bath. The maintenance of the pH of the deposition bath is essential because the end-product film is strongly dependent on it.

Finally, surfactants are commonly used in ELD baths. H₂ is a by-product that is always present during electroless deposition and it has to be removed. By changing the surface energy, surfactants are able to avoid H₂ evolution or to favour the removal of it. The absence of H₂ impurities inside the film is very beneficial to the film properties⁸⁰.

Many other additives are still used in ELD solutions to give many different effects such as the control of the surface tension, the removal of hydrogen from the deposits or the suppression of its evolution, and the improvement of the quality of the metal film, etc⁷⁶.

It is clear from this simple description of the typical compounds used in electroless deposition processes that quality does not depend just on the plated metal. Physical properties such as resistivity, roughness, hardness, adhesion, density of the film, etc. depend on many factors. Temperature, pH, composition of the bath, catalytic actions of the substrate, but also additives are among some these variables. The correlations lying between the quality of the film and the type of the solution used are not scientifically understood. All the knowledge of the effect of the bath chemistry on the film quality is mainly due to empirical works. An effective improvement in the process efficiency and applicability is then very complicated. However the high level of control of the morphology of the deposit can be exploited to give good filling of trenches up to nanometres scale, essential for an effective use of the technique in the ultra-large scale integration (ULSI) interconnect technology.

1.6 Nickel-Boron Electroless Deposition

This paragraph will be focusing on the electroless deposition of nickel boron alloys through an explicit understanding of the reaction mechanisms governing the process, from a theoretical and

practical point of view. A good understanding of the reduction of the nickel ions through the exploitation of the reactive reducing agent is essential to perform a correct development of the process itself, by increasing the plating rate, the density and uniformity of the film and by increasing the efficiency of the chemical species employed. In particular the possibility to have a good control over the final composition of the layer in terms of boron content is of extreme interest. The final boron content of the NiB deposit will have a large impact on defining the properties of the alloy.

An initial step to understanding the mechanisms governing the NiB ELD is to underline some essential features of the process:

- Evolution of hydrogen is always present as a consequence of the reduction of the nickel ions
- Depending on the reducing agent employed, there will always be at least a second element present in the deposition (boron, phosphorus)
- The process of reduction has to take place on chosen substrate but also on the surface of the depositing metal
- Hydrogen is formed as a by-product of the reduction reaction
- The molar ration of the deposited nickel with respect to the consumed reducing agent is usually close to 1 or less.
- The ratio of the utilized reducing agent is never close to 100%

The following section can then focus on the understanding of the chemical reactions governing the NiB ELD as the properties of the formed layer and its possible applications.

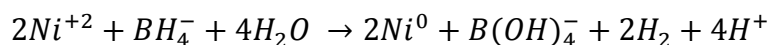
The most important reducing agents containing boron are the borohydride ion (BH_4^-) and amine boranes.

The borohydride reducing agent may consist of any water soluble borohydride compound but sodium borohydride is generally preferred. Some disadvantages come from the usage of borohydride based baths. In order to suppress the precipitation of nickel boride the pH has to be

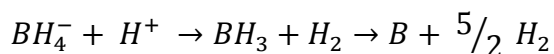
kept above the value of 12. As a consequence it is necessary for the substrate to withstand such basic environments.

Different possible mechanisms have been proposed: the accepted one, suggested by Mallory, on the basis of experimental data⁸¹⁻⁸³ is described in the following:

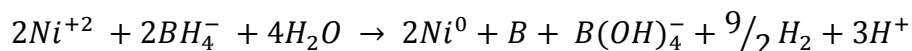
Reduction of nickel:



Reduction of boron:

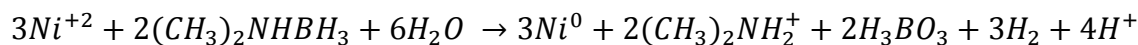


Thus, the overall reaction is:



Commercial use of amine boranes has in general been limited to dimethylamineborane (DMAB), $(CH_3)_2NHBH_3$. While theoretically the three hydrogens bonded to the boron atom should be able to reduce three nickel ions, this is not supported experimentally. Studies have confirmed that the molar ratio of nickel ions reduced versus DMAB molecules consumed is approximately 1:1⁸². As before, we can write down the two semi-reactions.

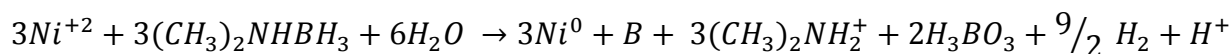
Reduction of nickel:



Reduction of boron:



And, overall:



Concentration of boron in the film is mainly determined by the nature and concentration of the introduced substances and also by the plating conditions. Normally the percentage of boron in the NiB film is quite low, with nickel concentration range going from 90% to 99.9%, even if deposit with 30% (or higher) of boron were also produced⁸⁴⁻⁸⁶.

As can be seen from the phase diagram the solubility of boron inside nickel is very low. Hence, for low percentages of boron, the NiB layer would result in a metastable supersaturated alloy that would separate creating a mixture of pure Ni and Ni₃B. Experimentally it has been demonstrated that for concentration of boron around 6% the deposit may have amorphous characteristics. Only after anneal at 300-400 °C the film actually resembles more the thermodynamically stable situation described by the phase diagram. Depending on the temperature and the heating condition a mix of Ni₃B and Ni₂B is obtained⁸⁷.

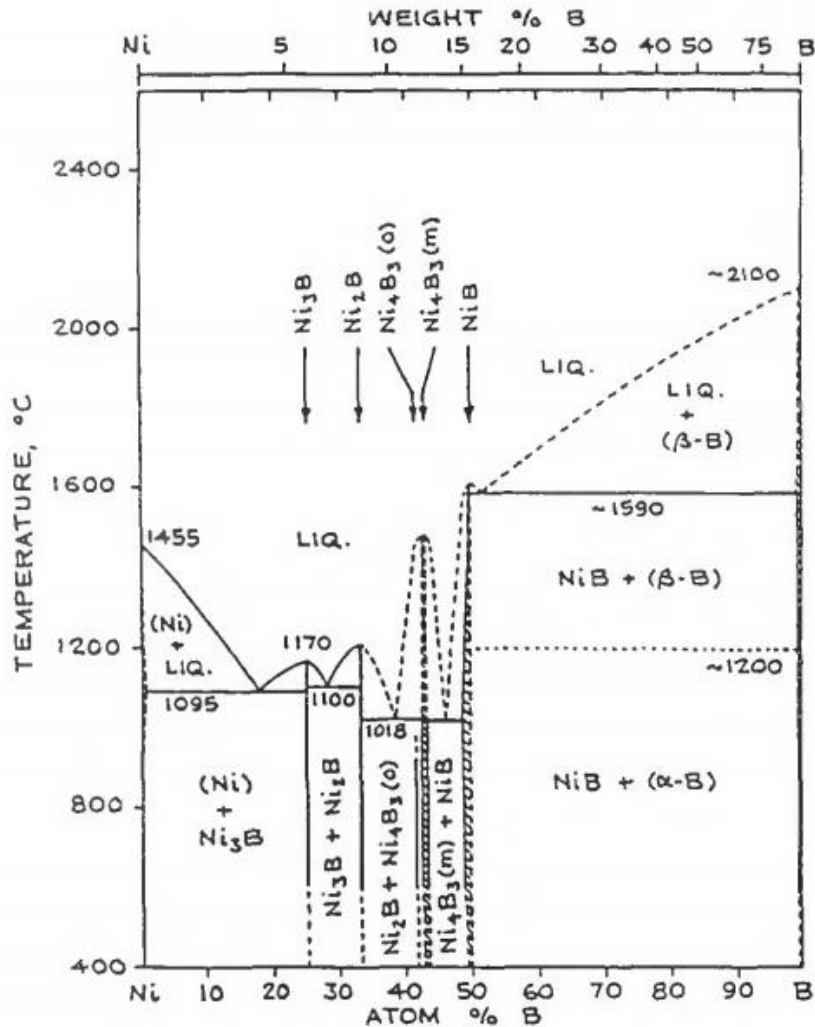


Figure 1.14 - Ni-B phase Diagram

More recent studies⁸⁸ have shown how the microstructure of the NiB deposits can vary with the deposition period and in the depth of the film. A semi-crystalline phase is normally formed at the early deposition stages, where the Ni content is at its highest. An amorphous growth at longer deposition times is characterized by the higher boron content of the later deposition stages. Nucleation of the NiB layer normally starts with the formation of highly packed islands on the top of the surface. Thus, at first the growth rate of the deposits tends to be much higher in the vertical direction than in the horizontal one. Later on, the growth is mainly due to new particles forming on top of the first layer, with equal growth rate in all directions. This evolution is responsible for

the change of morphology of the deposit, starting from a semi-crystalline columnar shape growth to an amorphous one. The different growth modes can be responsible for the development of tensile stresses inside the film. Consequently, atomic rearrangements can occur especially during post-deposition anneal but also during prolonged deposition.

We described NiB ELD as an autocatalytic process, where the deposited metal is able to act as a catalyser for a self-continuing reaction. It is anyway necessary for many substrates to be properly activated, prior to the deposition step, in order for the deposition to occur. Some kinds of metals, like Cu, Au, Ag, Pt, Pd are able to catalyse NiB deposition⁸⁹, while others can be forced to act as a catalytic surface by displacement plating of metals. For the other substrate, normally, palladium metal is used as a catalyser centre and hence different technologies have been developed for its deposition. Mainly Pd can be deposited with costly sputtering or PVD techniques or by immersion of the substrate in solution containing palladium chloride⁹⁰.

Chapter 2: Aim of the Work

This master thesis project, together with all the experiments necessary for its development and realization, was realized in imec laboratories (situated in Leuven, Belgium) during a 6 months internship.

In the previous chapter we described what a barrier layer is, its purpose and its current state-of-arts in the IC industry. We also described some issues that may be encountered due to the continual shrinking process in electronics. These issues are mainly related to the PVD process that cannot guarantee a correct step coverage, homogeneity and conformality of the Ta/TaN barrier layer. Alternative ways need to be developed to guarantee a good filling of small features like trenches and vias.

Among the potential alternative routes that have been examined, an all-wet process for the fabrication of ULSI devices has shown promising results in terms of cost-performance, better step coverage on features with complex geometries, simpler process for the formation of the film, without requiring costly vacuum environments⁹¹⁻⁹³. The wet process is composed of the formation of a SAM on the silicon dioxide, an electroless deposition on metal as barrier/seed layer, through a palladium catalyzation, and finally an electroplated copper filling of the features in patterned silicon wafers. As a metal intermediate layer, nickel-boron has shown good adhesion on the modified SAM, high temperature stability, smoothness and uniformity, good conductivity compared to copper and especially, together with the SAM layer, good barrier properties necessary to prevent Cu diffusion⁹⁴.

In this work, the process flow for the formation of thin NiB layers and the evaluation of such alloy as an alternative metal to copper interconnects in shallow trenches has been studied. First of all a screening of two different SAMs has been made, evaluating the one with the best properties in terms of stability, barrier properties and as host for the growing NiB successive layer. Previous

studies have demonstrated how amino-terminated alkoxy-silanes are the most suitable as precursors for this task³⁶. The deposition relies in fact on the negatively charged amino groups which are able to attract the positive Pd^{2+} charged atoms, present in the water-based PdCl_2 solution used as catalyser, forming palladium clusters on the surface. Also the uptake of Pd and Cl atoms from the SAM has been evaluated to assess the capability of the SAM to facilitate successive depositions. So, if the first part is mainly dedicated to the evaluation of the goodness of the SAM layers (but always paying attention to the successive deposition steps), the second part will be mainly focusing on the metal deposit characteristics. Deposition of copper has been thoroughly evaluated on SAM and in particular on amino-terminated SAM^{69,71,93}. Some copper

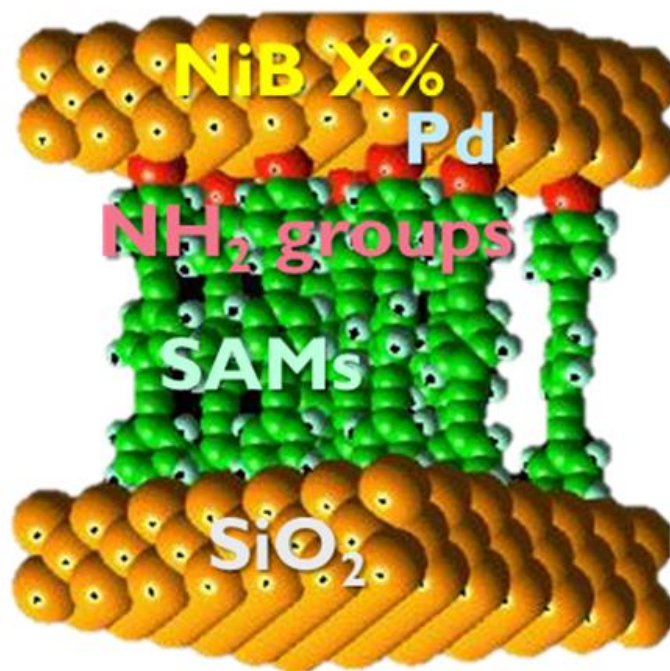


Figure 2.1 - Schematic of the realized stack.

issues, and more specifically diffusion, have been discussed in the introduction. Aware of these issues, in this research, we tried an alternative route employing NiB not only as a barrier layer, but also as a surrogate metal for line metallization. Two different NiB alloys have been evaluated, with different percentages of boron.

The deposits will be considered acceptable if good results are achieved in terms of the following characteristics: electrical (sheet and line resistance/resistivity), mechanical (adhesion) and chemical (atomic percentages in the film). Also, the growth process will be analysed in order to achieve a better understanding of the deposition process. The most significant measurements have been made both on blanket and patterned wafer, cut in coupons of various dimensions, all composed of silicon dioxide on silicon. The final stack, as can be seen in Fig. 2.1., is composed of Si/SiO₂/Amino-SAM/NiB-X%.

Chapter 3: Experimental techniques

3.1 SAMs deposition technique

All samples utilized during this research were used as substrates for SAM deposition. The deposition could be realized using either a wet or a dry process, as later described. Several different depositions were made, each varying one or more specifics of the process in order to achieve the best SAM deposition technique for the subsequent Electroless Deposition (ELD) of nickel-boron.

3.1.1 Vapour

The deposition of SAM using a vapour phase technique (PVD) was performed in a silanization oven (Figure 3.1 – right). Unlike the wet deposition, SAMs PVD was realized on 300mm wafer from which it was possible to cut out the coupons used in the following ELD experiments. In the same fashion as the liquid deposition, the SiO₂ substrate was pre-cleaned in a Jealight UV-O₃ cleaner (Figure 3.1 – left). This was performed in order to maximize the presence of –OH groups on the surface of the wafer and remove contaminants that can be present on top of the wafer. Atomic oxygen is simultaneously generated when molecular oxygen is dissociated by 184.9nm and ozone by 253.7nm. The latter is also capable of removing most hydrocarbons (Figure 3.2). The produced atomic oxygen is highly reactive: the excited carbon based contaminants on top of the wafer are readily attacked by it, producing smaller and volatile compounds that desorb from the surface, resulting in a perfectly clean substrate⁹⁵.



Figure 3.1 - The UvO cleaner (left) and the Silanization Oven (right) used during the research⁹⁶.

Before placing the wafer in the processing chamber the oven went through a pre-bake under N_2 flow at $155^\circ C$. The deposition process was later performed at a temperature of $140^\circ C$ for 30' or 60'. The silane come from a reservoir of 100 μl placed on a small grid above the wafer. At the end of the baking the oven was purged under N_2 flow and changes in pressure from 28 mbar to 700-800mbar.

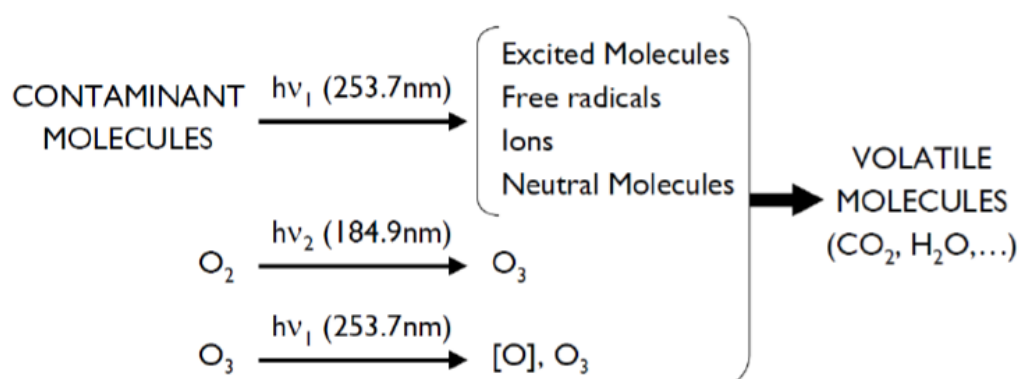


Figure 3.2 - Schematic representation of the UVO cleaning mechanism⁴⁹

3.1.2 Liquid

Even if the resulting equilibrium structures should be and are, in fact, equivalent³⁸, liquid deposition is considered a better technique than the vapour one since it is more widely used and the chemistry is better understood. Coupons cut from the Si wafer, with just a thin layer of SiO₂ plasma obtained on top, were processed in the already described UV-O₃ cleaner. The solution used was based on methanol, with a SAM precursor concentration of 5 mM (365 µl on 250 ml of solution). Also DIW was present (12.5 ml on a total of 250 ml) since H₂O is essential for the hydrolysis of silanes and their subsequent condensation. PEDA and DETA were both added in an oxygen-free environment, inside a Glove Box, where oxygen concentration is lower than 10 ppm, to avoid oxidation issues of the SAM precursor. Deposition is then carried out in tanks to avoid as much as possible the entrance of moisture. Coupons have been kept inside the solution for a time longer than 2 hours. This is the evaluated time needed to free a SAM from major defects. The depositing methanol based solution, is optimal to obtain a monolayer film. The free energy of the precursor molecule in the solution is such that the first deposition is energetically favoured, but the deposition of the subsequent layers is not.

At the end of the deposition the coupons were rinsed to remove the last traces of solvent and impurities. The step included 4 sonication processes for 2 minutes in respectively pure methanol, acetone, ethanol and DIW. The increase in polarity of the baths guarantees an enhancement in the solubility of the remaining previous solvent: the complete removal of it is essential to avoid interference with the ELD experiments, performed in aqueous solutions.

3.2 Contact angle

The measurement of the contact angle is a rather simple yet fast method to evaluate the wetting properties of surfaces through the use of a solvent droplet, typically water. The Dataphysics

OCAH230L contact angle measurement system, used during the development of this work, is based on goniometry and acquires images of the contour of a specific liquid sessile drop deposited on top of the solid surface by means of a CCD camera. Contact angles are determined by fitting a mathematical expression to the shape of the drop and then calculating the slope of the tangent of the drop at the liquid-solid-vapour (LSV) interface line⁹⁷. The angle θ is also related to the surface tensions between the different phases as described by the Young equation:

$$\gamma_{sg} = \gamma_{sl} + \gamma_{gs} \cos \theta$$

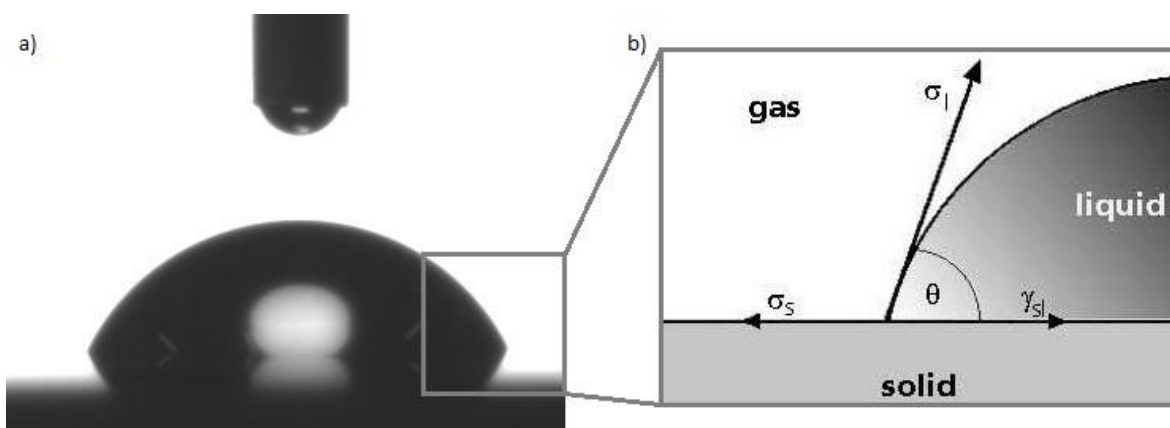


Figure 3.3 - a) Picture of a water droplet on a surface; b) schematic representation of the liquid contact angle and surface tensions and energies.

A schematic representation of the problem is depicted in Figure 9.3. Young's equation however is only valid under thermodynamic equilibrium. This practically means that the system has to be static: the drop is not moving and the drop volume is not changing. Therefore the contact angle measurement can be employed to evaluate the surface energies just by using two different liquids and fitting the results. The hydrophilic or hydrophobic character of the surface can be simply assessed by confronting the measured CA against a fixed value. Normally a 90° angle is considered the discriminating value between surface with high and low affinity with water. Contact angle measurements have been useful in this work to understand how the different tail groups present on the SAMs could modify the surfaces behaviour. It was also used every time for both wet and dry processed SAM to evaluate to goodness of the layer by comparing the measured CA value with the optimal value.

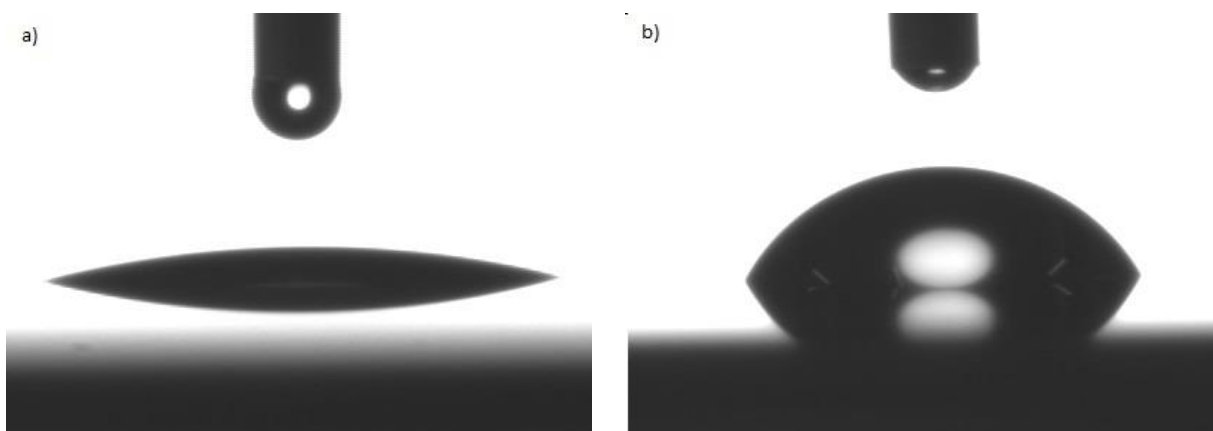


Figure 3.4 - Effects of SiO₂ surface state on hydrophilic behaviour. a) UVOzone cleaned. b) NH₂-SAM functionalized

3.3 Spectroscopic Ellipsometer (EP10)

The main techniques used in this work to study thin film are spectroscopic ellipsometer and x-ray reflectivity. Spectroscopic ellipsometer enables the user to measure the thickness but also the refractive index of semi-transparent thin film. The working principle of the instruments is based on the reflection and the transmission of a surface: the former depends, at a dielectric interface, on the polarization of the light while the latter compels; for transparent layers, the change of the phase of the incoming wave depends on the refractive index of the material. An ellipsometer is able to measure layers as thin as 1 nm up to a few μm . Other applications include the identification of materials, thin layers and characterization of surfaces. Apart from the high number of surface properties that can be evaluated the main advantage is the non-destructiveness of this optical, indirect technique.

The experimental setup consists of a laser and a polarizer which is able to provide a linear polarization to the monochromatic light. The beam, sent towards the sample, is reflected from the layer of interest and then analysed by an analyser. Ellipsometry is a specular optical technique where the angle of incidence equals the angle of reflection. Light which is polarized parallel to the

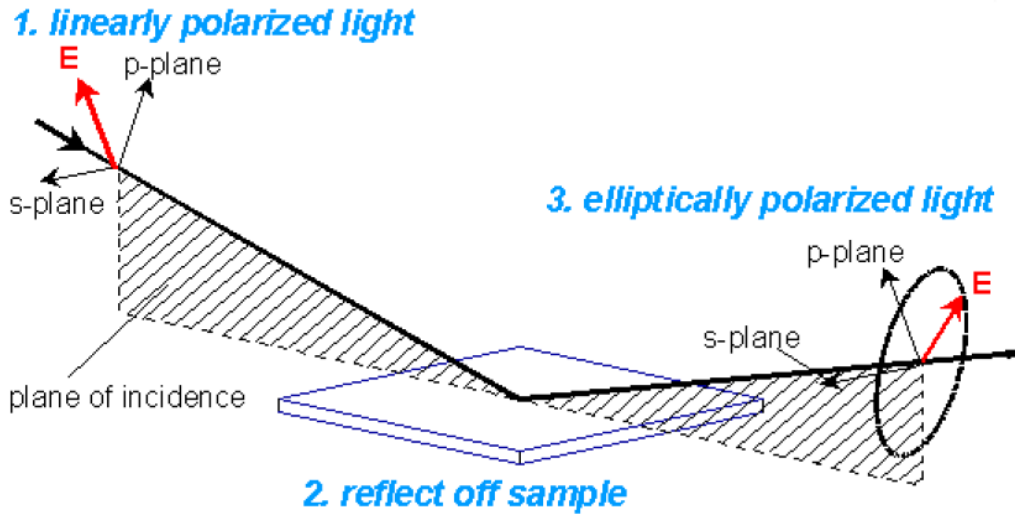


Figure 3.5 - Ellipsometer working principle

plane formed by the incident and reflected beam is named p-polarized, light with a perpendicular direction of polarization is called s-polarized, accordingly. After the reflection both s- and p-components go through a change in amplitude as expressed by the Fresnel equation.

$$\rho = \frac{r^p}{r^s} = \tan \Psi \cdot e^{i\Delta}$$

The ellipsometer measures the complex reflectance ratio, ρ , which may be parameterized by the amplitude component Ψ and the phase difference Δ . The amplitudes of both s and p components after the reflection, normalized to their initial values, are denoted by r_s and r_p .

For a single phase system the equation reduces to:

$$\rho = \frac{R^p}{R^s} = \tan \Psi \cdot e^{j\Delta} = f(n_i, k_i, d_i, \dots i)$$

Where n_i , k_i , d_i represent respectively the complex refractive index, the extinction coefficient and the thickness of the i film.

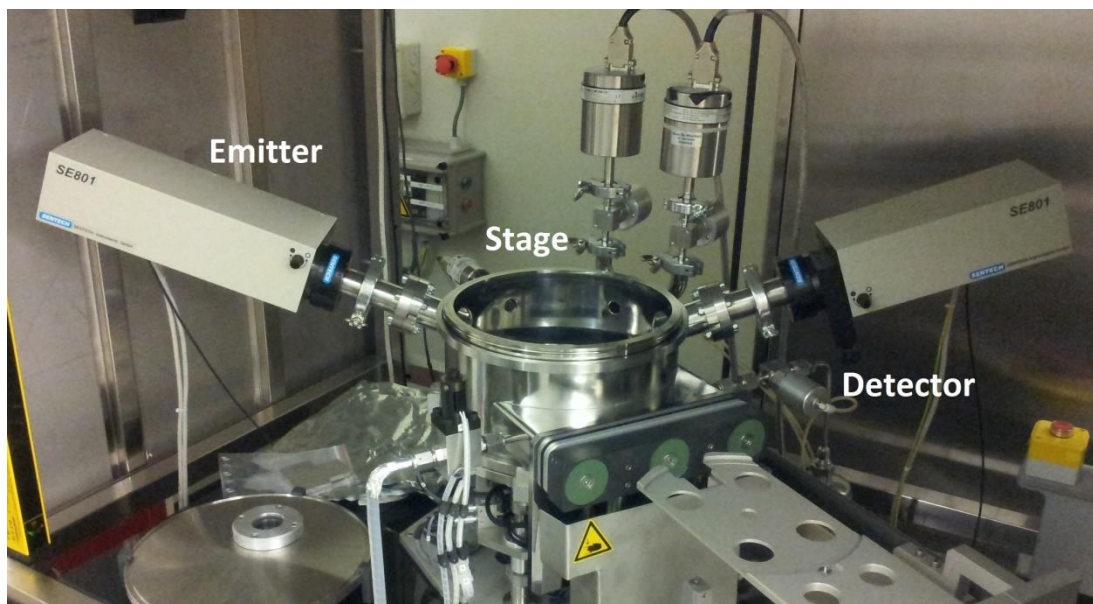


Figure 3.6 - Picture of the Ellipsometer employed: the laser emitter, the wafer stage and the detector can be easily individuated.

Being an indirect method, the measurement of Ψ and Δ cannot be converted directly into the optical constants of the sample. An iterative procedure (last-square minimization) is used to calculate the exact values of Ψ and Δ by means of the cited Fresnel equation. Very well defined interfaces are essential in order to achieve good results, due to the fact that output data are obtained through an indirect method⁹⁸.

A SENTECH SE400PV Ellipsometer was largely used during this research for the analysis of thickness and changes in refractive index of the SAM layer that are useful for the determination of the layer growth and the eventual presence of multilayers.

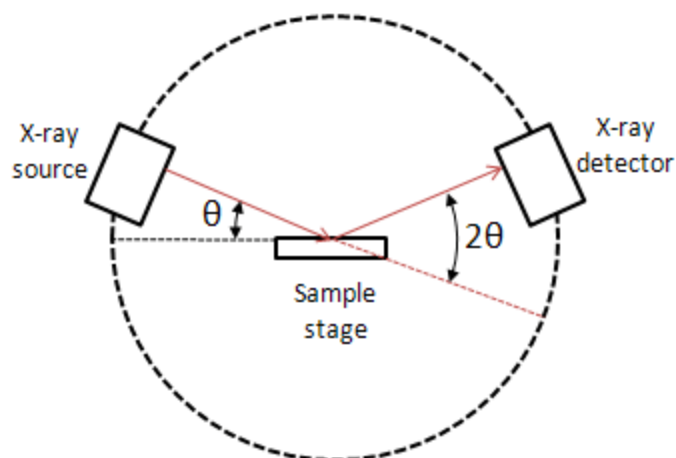


Figure 3.7 - Diagram of X-ray specular reflection.

3.1 X-Ray Reflectivity (XRR)

Similar to Ellipsometry, X-Ray Reflectometry (XRR) is a commonly used technique that combines a higher precision (1-3 Å) in the determination of thicknesses, up to c/a 200 nm, to the advantages of being non-destructive and contactless. Furthermore it is able to determine density and roughness of multilayer structures. The technique involves the reflection of a monochromatic x-ray beam of a certain wavelength λ from a flat surface at a grazing angle ω and the beam reflected with an angle 2ϑ is recorded by a detector. The operational mode is defined $\vartheta/2\vartheta$ because the specular reflection satisfies the condition $\omega = 2\vartheta/2$, that forces the incident angle to be always half of the one of diffraction. The reflection of the beam will depend on the different electron density of the various layers present in the sample, corresponding to the classical optics refractive index. Below a certain value of incident angle θ (normally around 0.3°) total external reflection occurs: this value of critical angle θ_c gives information regarding the density of the film. Above the value of θ_c the intensity will vary with the angle θ , giving rise to interference of the refracted

beams that will cause the birth of fringes of interference. Typical range of measurement lies between the 0° and 5° for the θ angle. The period of the interference fringes and the damping of the fringes provide insight respectively of the thickness and roughness of the layers.

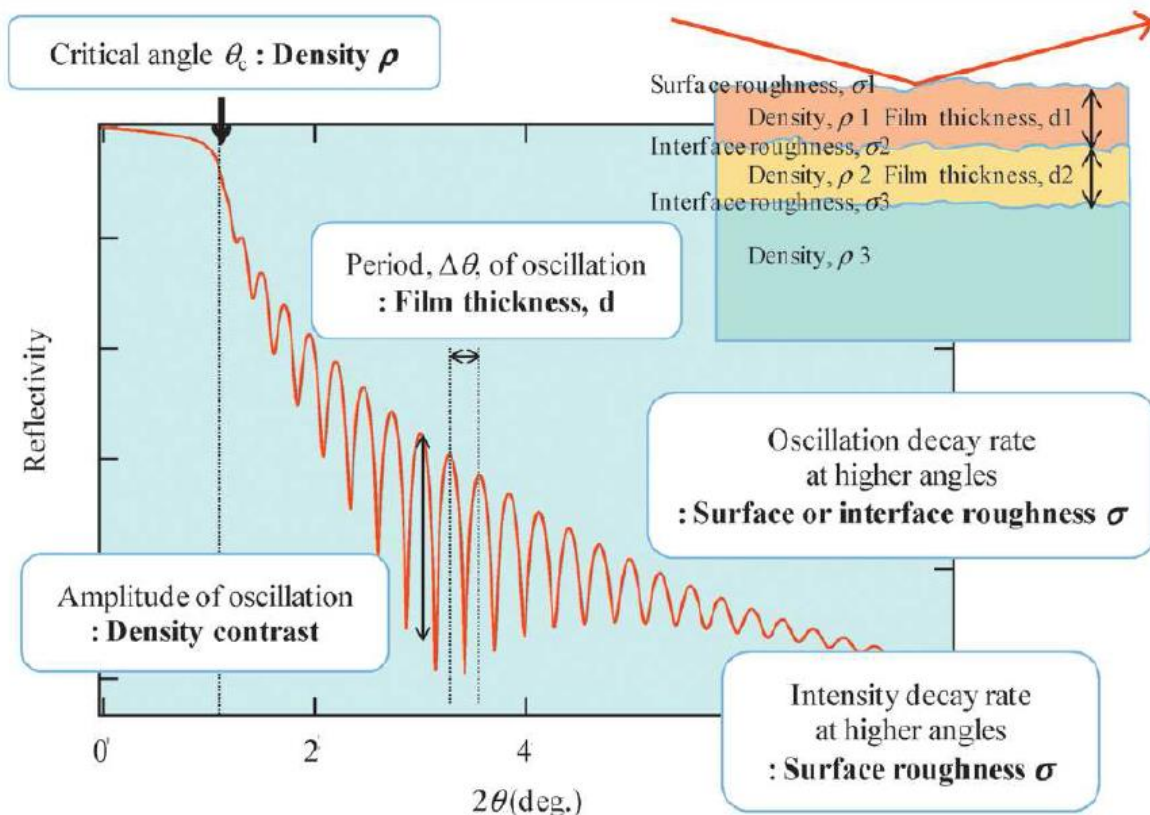


Figure 3.8 - XRR spectrum sample: the information that can be extrapolated from the plot are described (information provided by X-Ray Reflectivity)⁹⁹.

The outcome can be analysed by means of the classical theory of Fresnel for ideal smooth surfaces: the measured reflectivity is simulated with a software that changes parameters like density, roughness and thickness until a good fit is found. The chemical composition has to be already known.

The evaluation of SAMs with the XRR technique can be complex because of the very fine thicknesses of these layers (around 1-1.5 nm) and the smoothness that characterize them. But even if the number of periods is limited and the amplitude is very low, XRR is still useful to obtain information thanks to the high difference between the lower SiO_2 layer and eventual NiB top

layer. Indeed XRR has been proved to be a very powerful tool in the assessment of the thickness and roughness of the NiB layer mainly for the evaluation of the growth rate and the film resistivity but also to understand the changes occurring in the thin film after pulse annealing¹⁰⁰. The tool used in this work was the Bede MetrixL, used also to obtain XRD spectra.

3.2 X-Ray Diffractivity (XRD)

X-Ray Diffraction (XRD) is another technique that exploits the interaction between x-rays and the surface of the sample. The goal, with this technique, is to identify the crystalline phases present in the films and the structural properties such as strain rate, grain size and/or phase composition. Since the sensibility goes down to thicknesses of c/a 5 nm it is adapt to explore thin films properties.

As in the case of XRR a $\theta/2\theta$ operational mode is used with the angle θ , being the one defined by the surface of the sample and the incident x-ray beam, which is reflected with a 2θ angle, providing a diffraction pattern. This pattern is used to determine factors, typical of a crystalline form, that determine the intensity of the reflected x-ray. An X-ray hitting a crystalline form and reflecting can interfere with each other giving constructive or destructive interference. The first one will occur when Bragg's law is satisfied:

$$n\lambda = 2d \sin\theta$$

Where n is an integer number, λ is the wavelength of the incident wave, d is the spacing between the crystalline planes in the atomic structure and θ is the angle between the incident ray and the scattering planes. For single crystal or epitaxial films the spectra can be easily obtained but for polycrystalline structures like the one studied in this work each grain will possess a particular orientation. The surface is then tilted along a different angle ϕ to obtain multiple direction diffraction spectra. In this research the Bede MetrixL HDXRD mode was used to understand which

crystalline phases where present in the NiB layer and how the phases changed after an annealing process at high temperature.

3.3 Total X-Ray Fluorescence (TXRF)

Total reflection x-ray fluorescence (TXRF) is a surface analysis technique used to trace the atoms present on a surface. It is commonly used in the semiconductor chip manufacturing industry to assess the presence and quantity of contaminants, particles or residues on wafers. The main difference with respect to simple XRF is the impingement angle θ of the x-rays: it is always smaller than the critical angle θ_c at which total reflection occurs. If the width of θ is around 40° for XRF, in TXRF it arrives to values smaller than 0.1° , giving a huge increase in surface sensitiveness (sensitivity) by reducing the penetration depth from $1\mu\text{m}$ to $2\text{-}3\text{ nm}$ ¹⁰¹. An increased elemental measurement sensitivity due to its unique configuration coupled with a reduced measurement background contributions by elimination of sample scattering resulting in increased elemental measurement sensitivity, represent a big advantage of TXRF over conventional XRF.

The technique is based on the excitation by ionization of inner electron-shells by x-ray beam. The resulting relaxation of outer electrons towards the inner shells releases energy by photon emission. Qualitative analysis is possible through the evaluation of the energy of the emitted photons: this will be related to the difference in energy between the inner and outer orbitals'

$$E_{\text{photon}} = E_{\text{inner shell}} - E_{\text{outer shell}}$$

and is a unique characteristic of the studied element. Quantitative analysis is instead made by measurement of the intensity of the x-ray fluorescence radiation, which is directly related to the amount of atoms in the material^{102,103}.

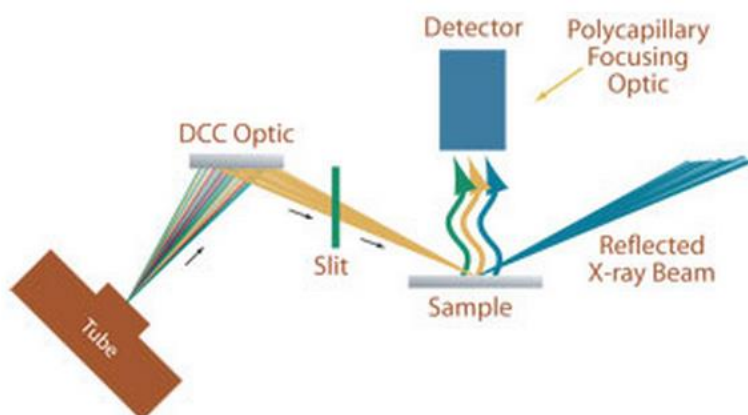


Figure 3.9 - Schematic view of a TXRF instrument

In this project, TXRF measurements were used to evaluate the quantity, in terms of atoms/cm², of Pd atoms present on the surface of different SAMs, for different deposition times and processing techniques, using a Atomika TXRF8300W tool.

3.4 Fourier Transform InfraRed Spectroscopy (FTIR)

Invented more than one hundred years ago, the two-beam Michelson interferometer is still the heart of the most modern Fourier transform infrared (FTIR) spectrometers. It consists of a fixed mirror, a moving mirror and a beam splitter. The beam splitter consists of a laminate material that reflects and transmits light equally.¹⁰⁴ So the collimated infrared beam produced by a He-Ne laser is partially reflected toward a fixed mirror while the other half is transmitted to a moving mirror. The moving mirror scans back and forth producing a path length difference with respect to the fixed mirror; at every moment the position of the scanning mirror has to be precisely known. The two IR beams are then reflected back to the beam splitter by the mirrors and onto the sample. On leaving the sample compartment the light is refocused on the detector. The two combined beams interfere constructively or destructively depending on the wavelength of the

light and the optical path difference introduced by the movement of the mirror. The latter is referred to as retardation: to obtain an interferogram, the detector signal is recorded as a function of the retardation^{36,104,105}.

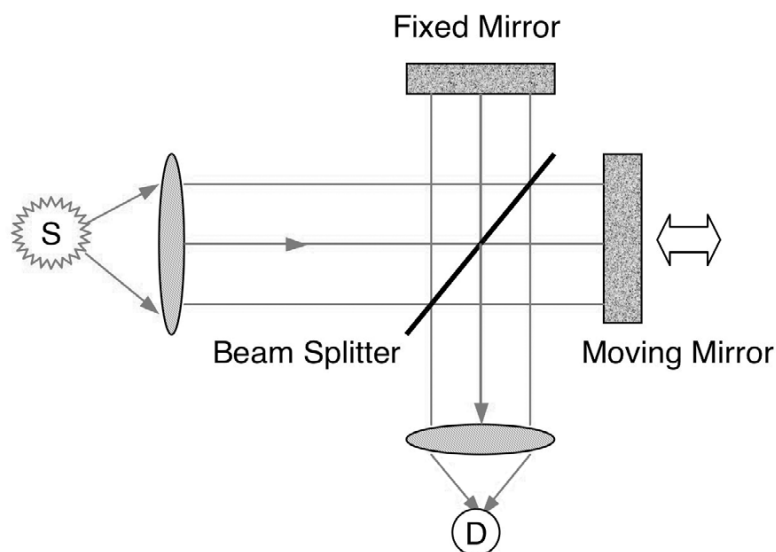


Figure 3.10 - Schematic of a beam-splitter, present in every FTIR instrument.

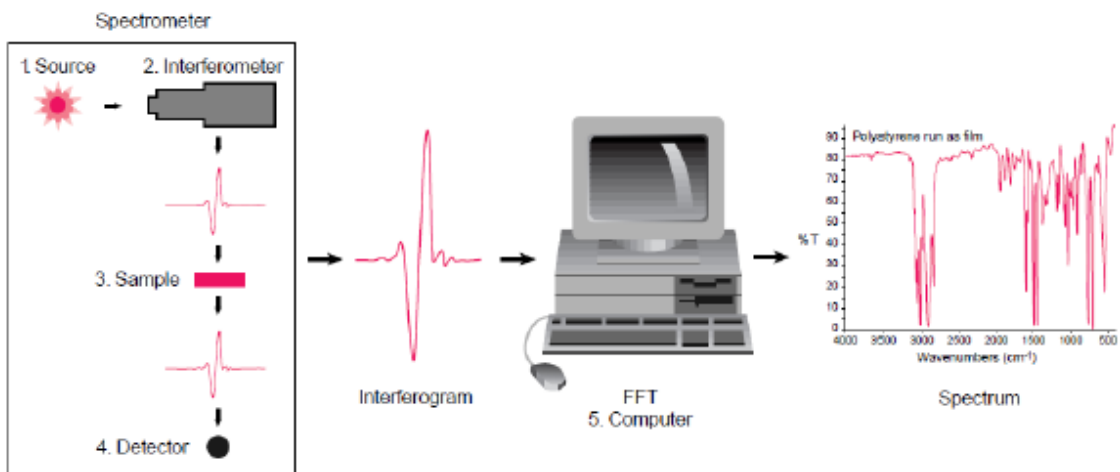


Figure 3.11 - Schematic of the transformation from an IR source signal incident on a substrate/substance to interpretable IR spectra

3.5 Anaerobic glovebox

A glovebox has been employed thoroughly during this work, due to the sensitiveness of the chemicals employed for the ELD process. A high presence of oxygen during the deposition would cause a faster decomposition of the bath, producing a lower quality metal film. The glovebox employed is shown in figure 3.12. The specific glovebox used for this, other than just atmospheric isolation, makes use of a Pd-catalyst canister which removes oxygen from the atmosphere by reducing it into water.

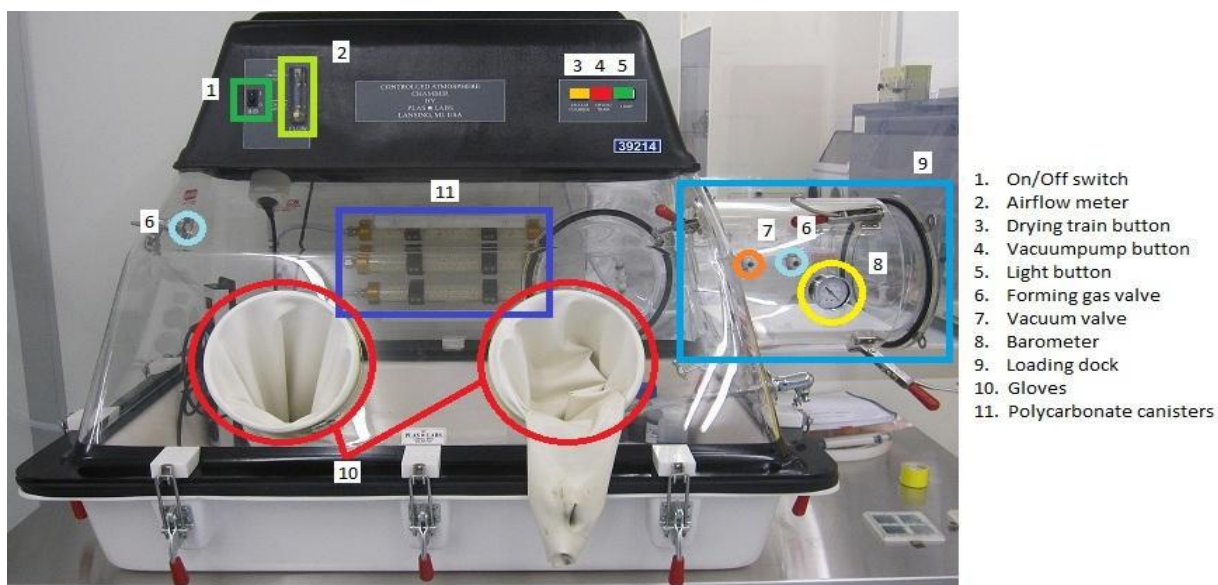


Figure 3.12 - Glovebox overview used for copper ELD (PLAS LABS, model 855-AC).

Forming gas (96% N₂ and 4% H₂) is pumped inside the glovebox: the hydrogen is necessary for the production of water, while nitrogen grants an inert environment. The water vapor released by the reaction and the solutions used for the experiments increase the moisture content in the atmosphere. In order to allow the Pd-canister to operate at its optimal capacity, the water is continuously removed from the atmosphere with the use of the drying train. The air is hereby guided through polycarbonate canisters which removes the moisture. The employed glovebox, if

used correctly, grants an atmosphere practically free from O₂ (concentration of the order of a fraction of ppm).

3.6 X-Ray Photoelectron Spectroscopy (XPS)

X-ray Photoelectron Spectroscopy (XPS), also known as ESCA (Electron Spectroscopy for Chemical Analysis) is a technique mostly used to retrieve chemical state of elements at the surface. As most of the surface analysis technique it uses a focused beam of x-rays aimed towards the surface of the samples to obtain a spectrum while the kinetic energy and number of electrons that escape from the top (from 0 to c/a 10 nm) of the material being analysed.

In a simple XPS experiment a X-ray beam illuminates a sample from which electrons are ejected as a result of the photoelectric effect. The kinetic energy of the ejected electrons is then determined by an electron analyser. As the energies of the X-ray and of the ejected electron are known, the binding energy of the electron can be determined:

$$E_{binding} = E_{photon} - (E_{kinetic} + \varphi)$$

where $E_{binding}$ is the binding energy (BE) of the electron, E_{photon} is the energy of the X-ray photons being used, $E_{kinetic}$ is the kinetic energy of the electron as measured by the instrument and φ is the work function of the spectrometer (not the material). The work function term ϕ is essentially an instrumental correction factor that accounts for the few eV of energy given up by the photoelectron as it becomes absorbed by the instrument's detector. The equation above simply takes into account the conservation of energy of the electron during the process. Knowing the binding energy leads to an easy identification of the elements from which the electron originates. Depending on the chemical state of the elements, small variations of the binding energy may be present leading to chemical analysis. IMEC has a Theta300 system from Thermo Instruments: it is equipped with a monochromatized Al Ka X-ray source (1486.6 eV), a neutralization gun and a

sputter source (Ar) working between 0.5 and 2.0 keV. It allows parallel angle resolved analysis with for angles between 21 and 78 degree as measured from the normal. It has a variable X-ray spot size between 400 and 25 microns. The tool was mainly used in this work to determine and compare the $-NH_2$ group density on coupons with different deposition technique: vapour or liquid. Also it was possible to calculate the thickness of the SAMs in order to compare them with the values derived from EP and XRR.

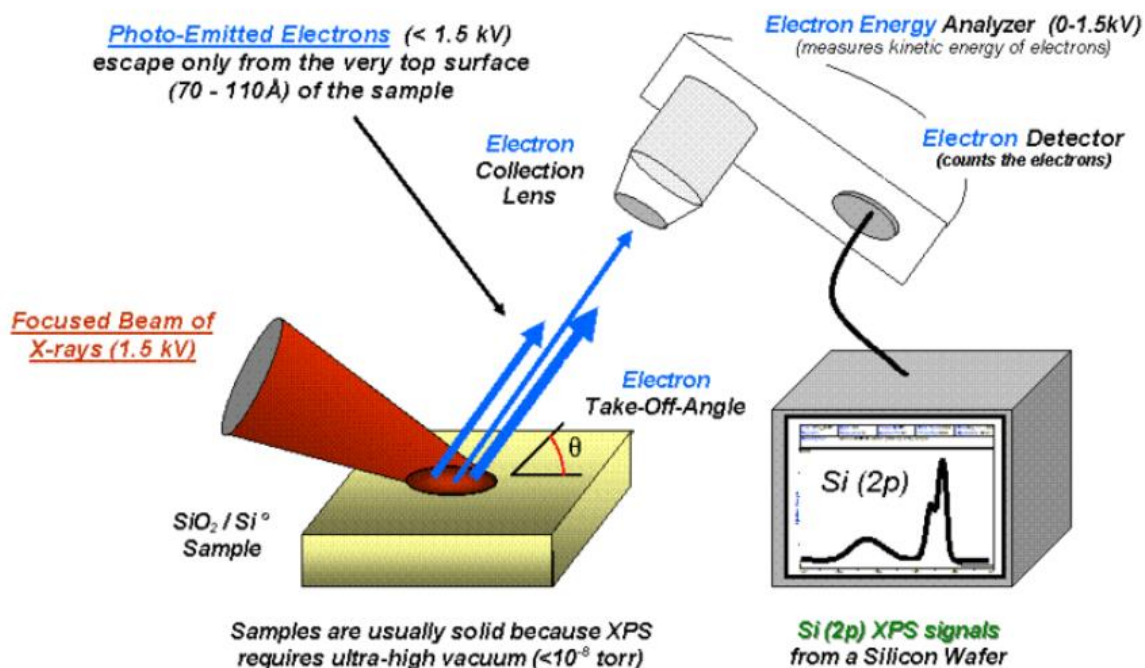


Figure 3.13 - Schematic representation of an XPS measurement

3.7 Scanning Electron Microscope (SEM)

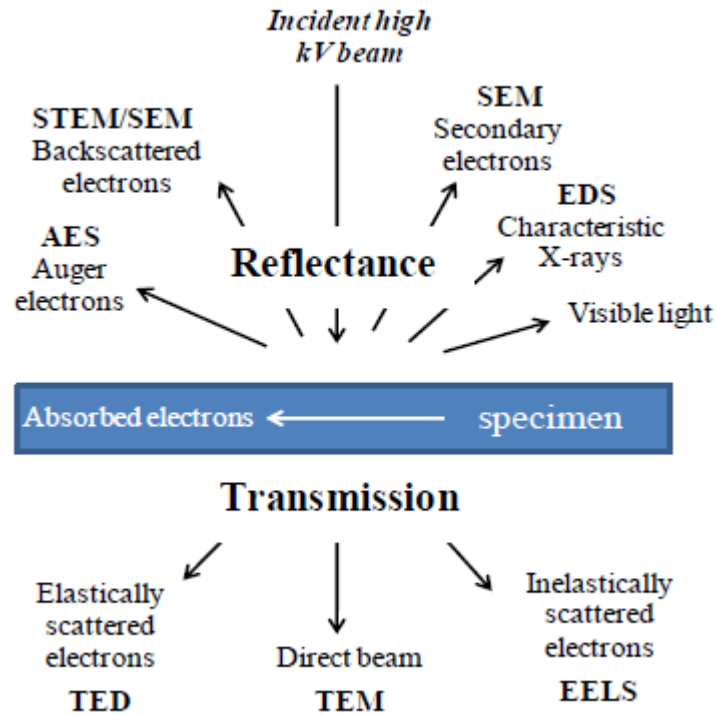


Figure 3.14 - Representation of the possible phenomena related to the interaction of x-rays with a specimen together with the instrument used to collect information from them.

The Scanning Electron Microscope (SEM) is a special type of electron microscope that produces images of a sample by scanning it with a focused beam of electrons. It is one of the most commonly used electron microscopes for the examination of microstructures and their morphology. The microscope uses a focused beam of high energy electrons that on hitting the surface of the sample generates a variety of signals, including secondary electrons (SE), back-scattered electrons (BSE), characteristic X-rays, light (cathodoluminescence) (CL), specimen current and transmitted electrons that can then be analysed. It's rare anyway to have detectors for all possible signals mounted on a SEM, but secondary electron detectors are standard equipment for all tools. Optical lenses are installed to enlarge the visual angle and it is also possible to obtain compositional and orientation data on the sample. Basically, in a scanning

electron microscope a small beam of electrons (of the order of ~ 10 nm) scans the surface of a sample, while the subsequent interactions of the electrons with this sample are further analysed by several detectors as shown in Fig. 3.13. In Fig. 3.14, instead, there is a simple schematic of a SEM microscope.

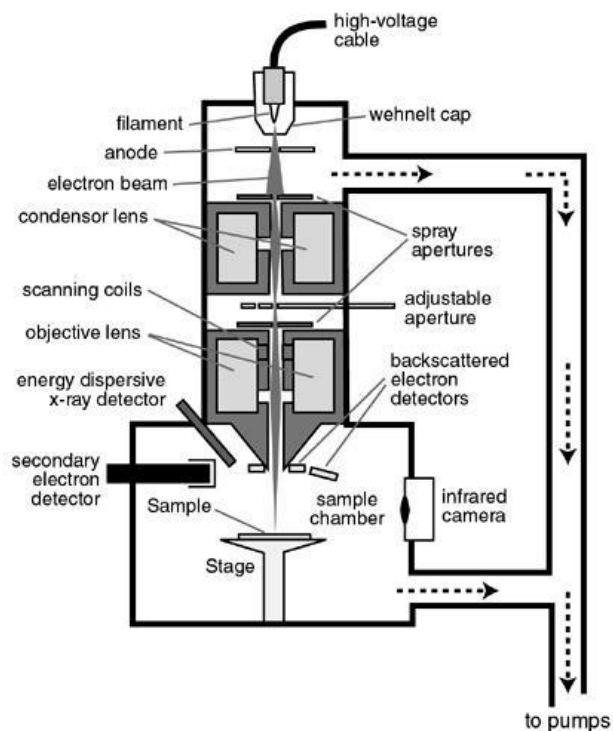


Figure 3.15 - SEM microscope scheme

In the most common or standard detection mode (secondary electron imaging or SEI), the SEM can produce very high-resolution images of a sample surface, revealing details smaller than 1 nm in size. Due to a very narrow electron beam, SEM micrographs have a large depth of field, yielding a characteristic three-dimensional appearance useful for understanding the surface structure of a sample. Also the intensity of back-scattered electrons (BSE) is normally evaluated because the signal is strongly related to the atomic number (Z) of the specimen; BSE images can then provide useful information about the distribution of different elements in the sample. The extraction of an image by SEM is then dependent on the signals coming from secondary and backscattered electrons. The source of electrons is usually a tungsten filament or a field emission gun. The

electrons emitted are focused by a series of electromagnetic lenses and accelerated to an energy in the range of 1-30keV. Subsequently, the beam is deflected by scan coils to direct it to a specific position on the sample.

In this work SEM was used to characterize and give real images of the NiB and/or Cu layer inside the structures that were processed. It is a very powerful tool to give a precise indication on the presence of possible defects on thin film structures and so to correct possible flaws in the processing step.

3.8 Transmission Electron Microscopy (TEM)

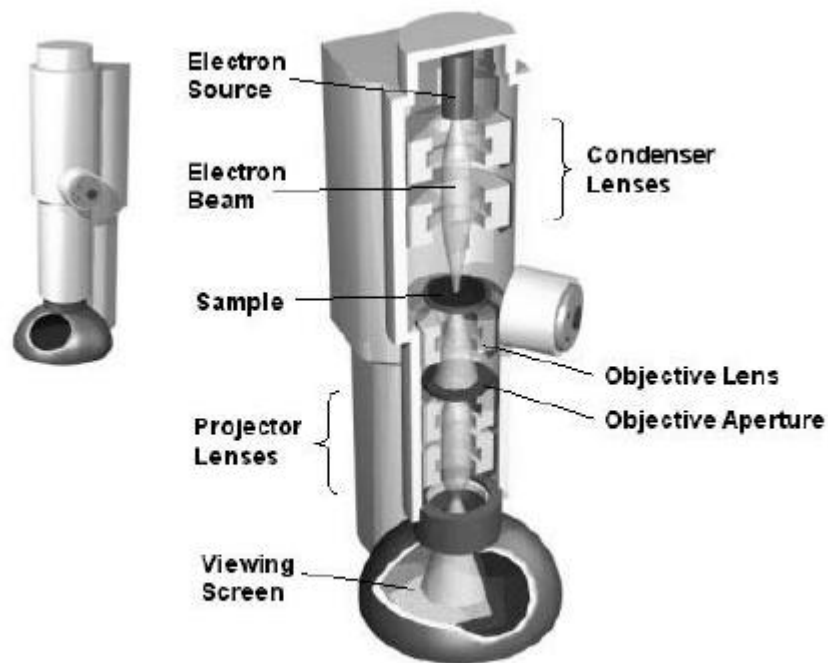


Figure 3.16 - Simple schematic of a transmission electron microscope.

The Transmission Electron Microscopy (TEM) (schematic in figure above) is a microscopy technique where a high energy monochromatic and coherent beam of electrons is transmitted through an ultra-thin specimen (less than 200 nm), interacting with the latter as it passes through it. These electrons are scattered at different angles depending on the density of the atoms encountered. One of the most important advantages of TEM over other characterization techniques is that information can be obtained both from direct and indirect space. In direct space, two modes are typical, i.e. TEM and High resolution TEM (HRTEM) which can discern the structure and morphology of a material thanks to the high magnification and high resolution allowed by this technique. In indirect space, diffraction yields information on the crystallinity of the specimen. Besides these possibilities, chemical information can also be acquired using the inelastic interaction of the incoming electrons with the atoms of the specimen. Here two techniques are typical, i.e. electron energy loss spectroscopy (EELS), and energy dispersive X-ray spectroscopy (EDS).

For the aim of imaging the filling of the trenches in patterned coupons with the NiB or Cu layer, and assessing the interdiffusion of chemical metals inside the silicon or the dissolution of barrier layers inside the metals, TEM has been an extremely important tool. On the other hand, despite the huge potential of the microscope, the imaging of the SAM layer still remains a great challenge. In this work it has been impossible to distinguish the SAM layer from the native SiO₂ or the MnN_x barrier layer.

3.9 Four Point Probe

During the realization of this project two different “4 point probe” tools for the evaluation of resistance were used. In particular, while the basic principles on which the tools worked were the same, the setup was different, one allowing a best usage for thin films, and the other for line resistivity. The 4 point probe uses separate pairs of current-carrying and voltage-sensing

electrodes to make more accurate measurements than traditional two-terminal sensing, having the advantage of eliminating the impedance contribution of the wiring and contact resistances. For the line resistivity configuration we have 4 contacts on the sample: on every one of them one probe will be positioned, assuring good contact between probe and bumps. 2 of the 4 probes were used to force a current into the line. This current will generate a voltage drop across the impedance to be measured according to Ohm's law $V=RI$. In order to avoid the contribution on the voltage drop, the one coming from the wires themselves, the other pair of sense connections is made immediately adjacent to the target impedance. The voltage drop across the wires is so small that it can be neglected.

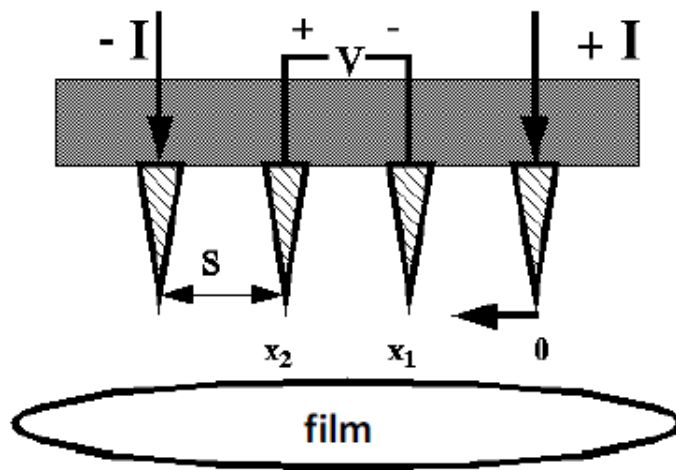


Figure 3.17 - Representation of a Four-Point Probe used for the measurement of sheet resistance.

On each coupon, for every line width, 4 different lines (contacts) were available for measurement. The value obtained was then an average made on these 4 measurements. In the case of thin film resistivity instead, measurements could be made on every location of the coupon. Normally 5 measurements were made around the centre of the coupons, where results are not affected by edge-effects. For line resistivity measurements the 4 probes could be moved independently in order to be able to position them correctly even for very different surface designs; this was instead not necessary for thin film resistivity measurements. Here the 4 probes were positioned

along a line where the 2 central ones measured the voltage while the external one forced the current, similarly to the previous case. Spacing between the probes is always the same and constant. Figure 3.16 and 3.17 can be useful to understand the differences between the 2 different systems that have been used.

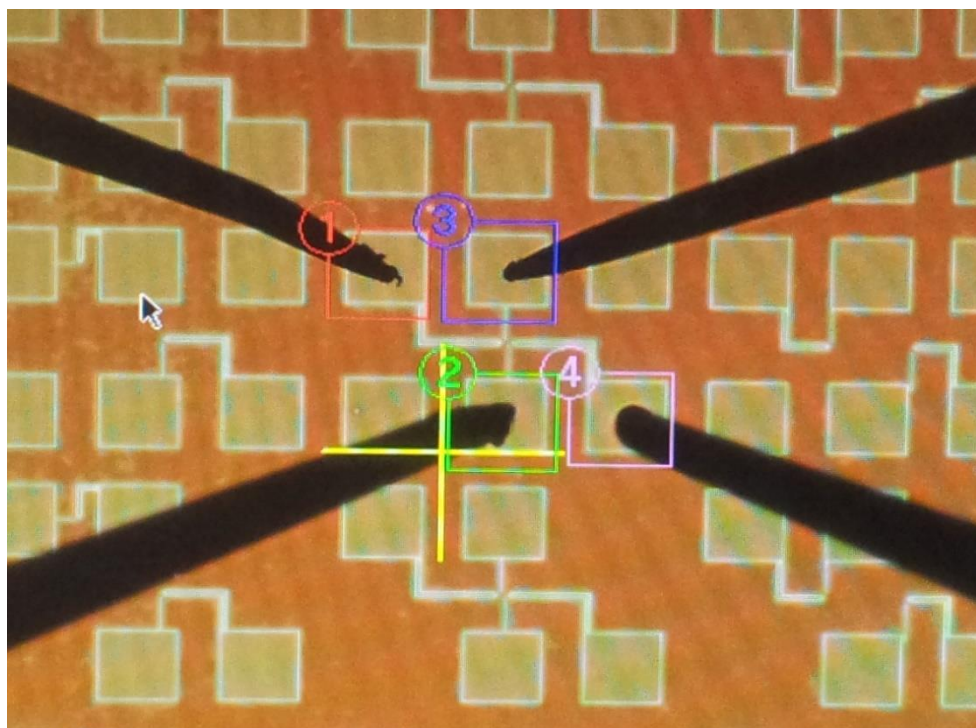


Figure 3.18 - Caption of the 4 needles used to measure the resistivity on patterned coupons.

Note that in the case of a very thin sheet, current lines arise in the form of rings around the probes, while for metal lines they run along the line itself. The resistance data obtained is of quite low significance: additional calculations had to be made to obtain resistivity values, which are far more useful and comparable.

3.10 Chemical-Mechanical Polishing

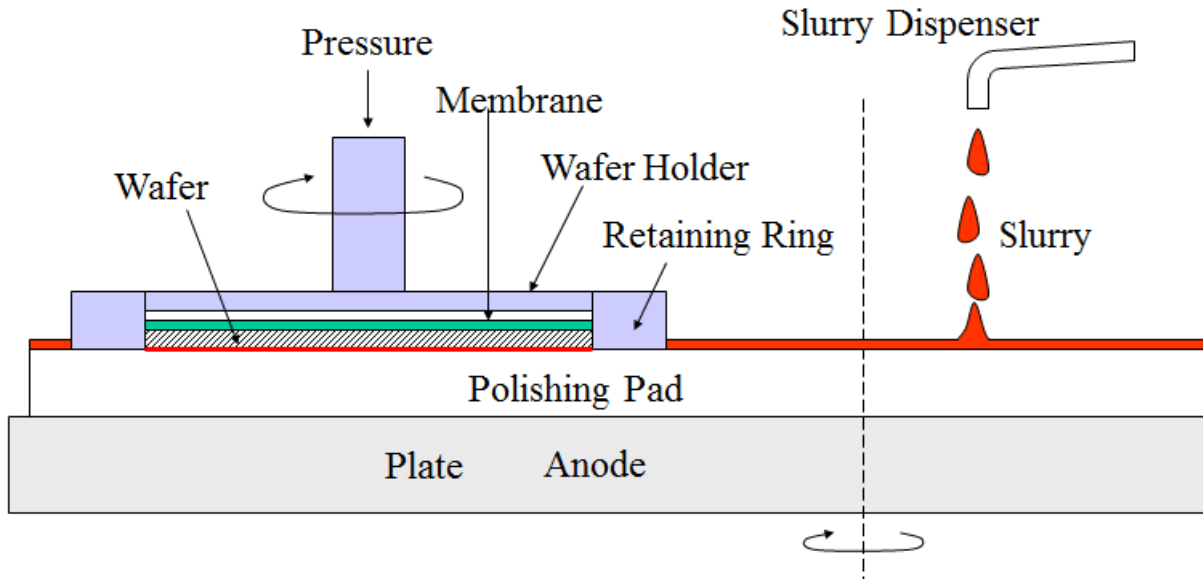


Figure 3.19 - Schematic CMP step.

Chemical Mechanical Polishing (CMP) is a process of smoothing surfaces by means of a chemical etching and free abrasive mechanical polishing. Since the moving from aluminium to copper of the semiconductor industry, this process has become a fundamental procedure to remove material in a planar and uniform fashion, with the ability to stop at the interface between copper and oxide layer due to the selectivity of the slurry. Mechanical grinding alone may theoretically achieve planarization but the surface damage is higher compared to CMP. Chemistry alone, on the other hand, cannot obtain planarization because most chemical reactions are isotropic. However, the removal and planarization mechanism is much more complicated than just considering chemical and mechanical effects separately. CMP makes use of the fact that high points on the wafer would be subjected to higher pressures from the pad as compared to lower points, hence, enhancing the removal rates there and achieving planarization¹⁰⁶. Mainly used with copper it can also be applied on other metals like tungsten, nickel, silicon dioxide and (recently) carbon nanotubes¹⁰⁷. It consists of a rotating and extremely flat platen which is covered by a pad. The wafer is mounted upside down on a carrier that is provided with a retaining ring that keeps

the wafer in the correct horizontal position and vacuum is used to keep the wafer in the carrier during loading and unloading. Good speed control is important to prevent damage to the polished layer i.e. cracking or delamination; both, the platen and the carrier, are rotating and speed can be easily controlled. During chemical mechanical polishing, pressure is applied by a downward force transferred to the carrier through its axis and a gimbal mechanism¹⁰⁸.

In this work an experimental Mecapol polisher was used to remove the extra NiB on patterned coupons in order to measure the line resistivity. Different pads are available on the tool (for wafers from 2 to 8 inches and for wafer pieces), but for 2.9x2.6 cm coupons we used one type with precise pressure content. It was possible to adjust the rotating speed of the pad and the holder as well as the pressure of the pad to get the best result without damaging the metal or polishing the oxide surface¹⁰⁹. Two different commercial slurries were used on NiB 1% and NiB 10% layers: ACUPLANE 4100 and ACUPLANE 6000 A0. The first one gave the best results for both NiB chemistries because of its good selectivity between metal and SiO₂ and ability to uniformly polish the NiB layer.

Chapter 4: Self-Assembled Monolayer

Characterization

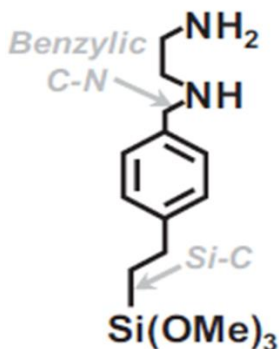
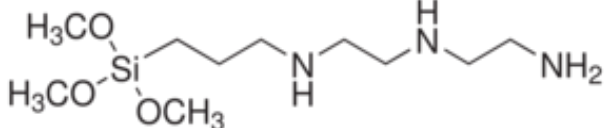
This chapter will be focusing on the presentation of the experiments realized for the characterization of the two studied SAM layers. This was possible through the evaluation of some important physical and chemical properties of the organic film, considering different precursors, deposition procedures and methods.

4.1 Introduction

During the development of this work two different molecules, employed as precursors for the SAM formation, were intensively studied. The precursors differed from each other in the number of amino-groups and in the kind of backbone uniting tail and head groups. (Aminoethylaminomethyl)-phenylethyltrimethoxysilane (PEDA) is characterized by two amino groups and a bulky, aromatic group, which is known to enhance the barrier properties of the SAM layer⁶¹; (3-Trimethoxysilylpropyl)-diethylenetriamine (DETA) shows instead a higher number of amino-group, with an alkyl-based backbone (Table 4.1). While DETA was studied for the first time in this kind of applications; PEDA has already shown promising results in previous studies and has been employed for further analysis other than as benchmark. Both SAMs belong to the -trimethoxysilane group ($-\text{Si}(\text{OCH}_3)_3$). The -trichlorosilane ($-\text{SiCl}_3$) based SAM show very good barrier properties when coupled with Cu, up to 400 °C, with no silicides formation. On the contrary more reactive groups, like $-\text{SH}$ and $-\text{C}_5\text{H}_4\text{N}$, present lower thermal stability (200-300 °C). Also the -trimethoxysilane group shows low thermal stability and silicides formation at low

temperature but surprisingly, when coupled with an amino-terminated group, the resulting monolayer show very good thermal stability and inhibition of copper diffusion. Besides, adhesion can be considered significantly high, since the tape-test has been successfully passed³⁶. This is the main reason why amino-trimethoxysilanes are chosen among the other SAMs. The chemical structures of the two molecules are presented in the following table.

Table 4.1 - SAMs precursors employed with the respective molecular structure.

SAM Precursor	Molecular Structure
<p>PEDA (Aminoethylaminomethyl)-phenylethyltrimethoxysilane</p>	
<p>DETA (3-Trimethoxysilylpropyl)-diethylenetriamine</p>	

The SAM layer, other than providing a barrier layer against interdiffusion, has to provide suitable anchoring positions for the palladium deposition. The accomplishment of such task is simplified by the presence of the amino-group of the proposed molecules, therefore di- and tri-amino heads are chosen as precursors. The quantity of Pd atoms on the surface will be evaluated as an indicator for the quality of the NiB growing layer. All the stack has to be characterized by good adhesion properties, necessary for the successive micromachinery passages.

We described in section 1.4.2 how the precursor can be deposited on silicon through different techniques. Both methods of deposition, vapour and liquid have been employed during this project, all on the same substrates: SiO_x on Si (100). An evaluation of the two processes,

considering different deposition times (from 1h to 24h for wet deposition and 30' or 1h for the vapour one) was also made.

Liquid deposition is normally carried out in a methanol-based solution. At first toluene was used as solvent, but the growth of PEDA did not follow a Langmuir-type growth kinetics. A more polar solvent like methanol, instead, produced a monolayer, as demonstrated from the evaluation of the thickness versus the growth-time.

4.2 PEDA

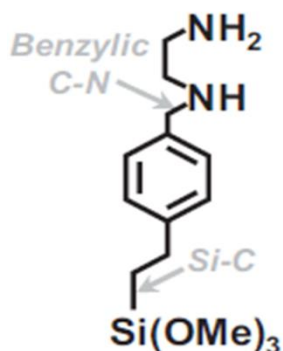


Figure 4.1 - Molecular structure of PEDA

4.2.1 Materials and Methods

4.2.1.1 Sample preparation

The (Aminoethylaminomethyl)-phenylethyltrimethoxysilane (PEDA) (precursor in figure 4.1) SAM has been prepared through both wet and dry process. The liquid deposition was carried out on square coupons of different dimension, depending on their successive employment, ranging from

2x2 to 5.5x5.5 cm². The coupon, previous to the actual deposition step, went through a cleaning process, involving the use of the described Jealight Uv-Ozone cleaner. The coupons were then freed from carbon residues and the surface was functionalized with –OH groups, necessary for the SAM anchoring step. The PEDA precursor is then diluted, with a concentration of 5 mM, in a methanol/water 95:5 v/v based solution, with acetic acid (1 mM). With such solution a perfect deposition could be achieved, with a bright and shiny surface (it appears blurry and thick if multilayer is deposited). Rinsing of the coupons is quite a complex step. It involved four different rinsing passages in four different solvents of increasing polarity: starting from methanol, on which the depositing solution is based, passing through acetone, ethanol and finally De-Ionized Water (DIW), every time with a 2' sonication. In such a way excessive molecules, eventually absorbed on top of the monolayer and remains of the depositing solution, could effectively be removed. A final drying with the N₂ gun closed the liquid deposition process. Deposition times ranged from 1h to 24h depending on the specific application. It has to be underlined that the cleaning step were normally done manually for patterned coupons, to avoid the collapse of the side of the trenches or other features present on the sample.

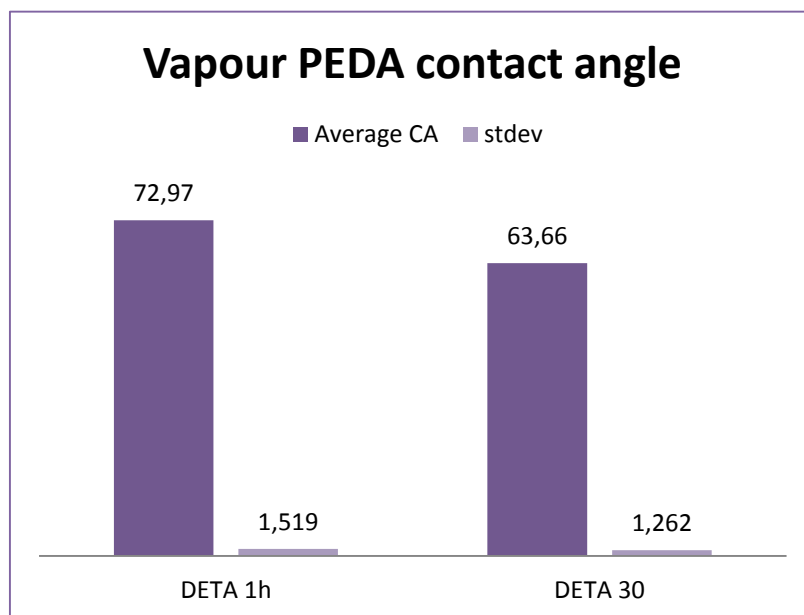
The dry deposition followed the same cleaning process, with the same purposes, with the only difference that full-wafer were processed. A full-wafer wet-deposition would be far more complicated than the coupon one, because the rinsing/sonication process cannot be accomplished effectively. In this sense, the dry deposition can be much more appealing to achieve industrial scaling-up. The wafer, after cleaning, was positioned on a support, inside the silanization oven, and brought to a temperature of 140 °C. The silane was deposited on a small grid, above the wafer, working as a reservoir. The deposition was carried out at low pressure, 28 mbar, to avoid the co-deposition of contaminants on the wafer during the SAM formation.

4.2.2 Analysis and Results

A first analysis to assess the goodness of the layer was the contact angle measurement. The CA value of PEDA was already known from previous studies and therefore this value could be confronted with the measured one on each single coupon. The earlier described dataphysics OCAH230L contact angle measurement system was employed with success, using droplets of 1-2 μl . The CA was evaluated versus the deposition time: as it can be seen from table 4.2 no large fluctuation was noticed for different deposition times.

Table 4.2 - CA values, together with standard deviations, of PEDA wet-deposited considering different deposition times.

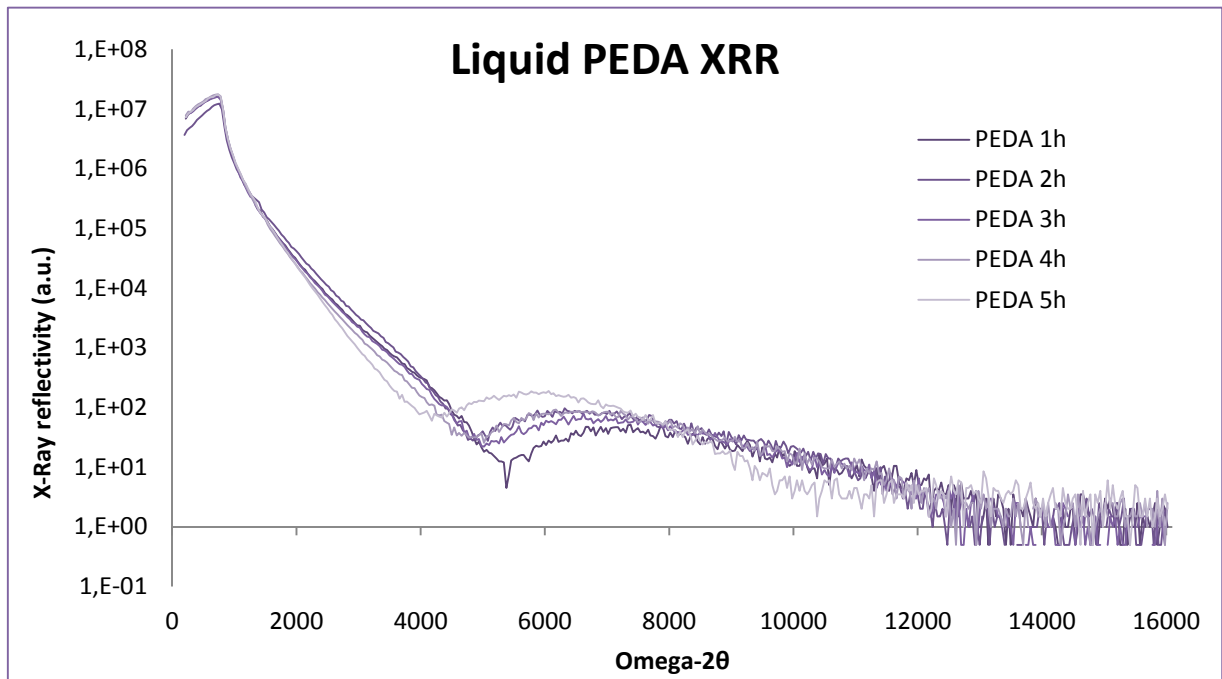
Deposition Time	CA value	Standard deviation
PEDA liq 1h	60.28	1.809
PEDA liq 3h	60.32	1.133
PEDA liq 4h	63.16	1.020
PEDA liq 5h	61.28	1.349



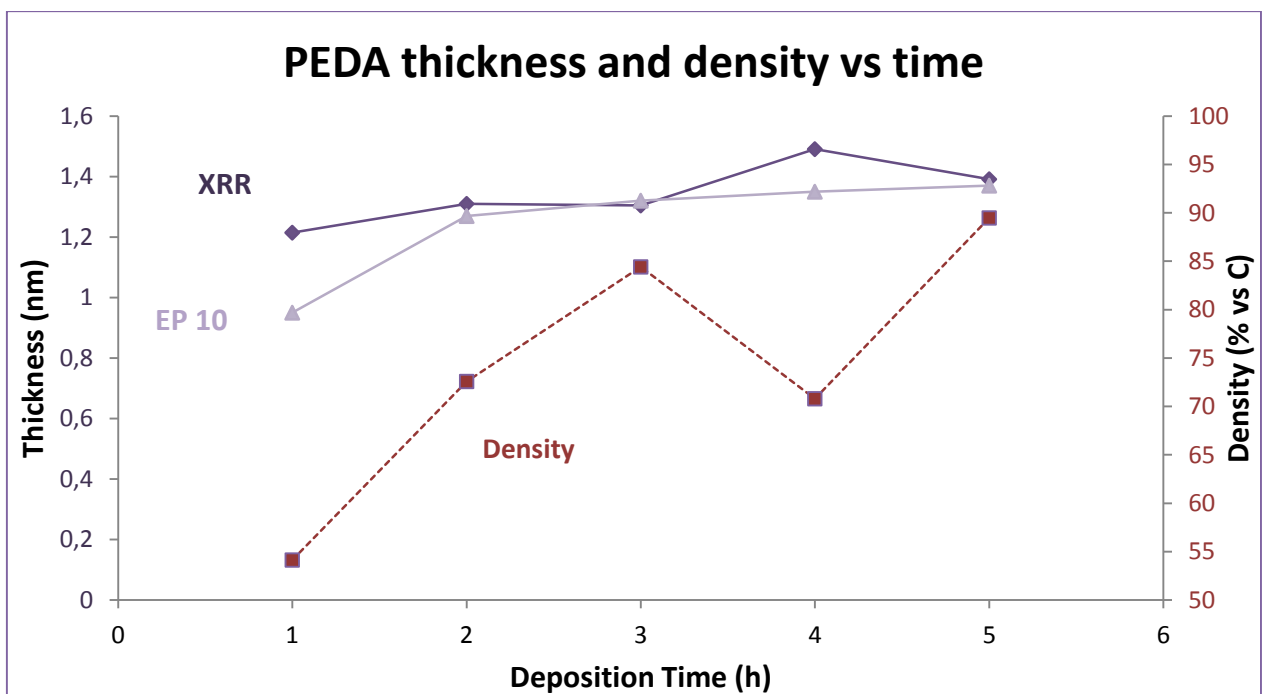
Plot 4.1 - Contact angle values of vapour deposited PEDA, for 1h and 30' deposition.

Also for the vapour deposited PEDA, the contact angle was evaluated. 37 measurements have been made along two perpendicular axes and an average value was calculated. These values are inserted in plot 4.1, together with the respective standard deviations. The values obtained are in line with the one found in literature of $60^\circ \pm 2^{10}$. Only the 1 hour deposition of vapour PEDA shows a higher value: this could be a symptom of a non-correct packing of the molecules or of a multilayer deposition. In this sense a longer deposition time does not seem to improve the layer properties.

XRR has proven to be a very useful measuring system for thickness and other SAM properties. In Plot 4.2 the XRR data is presented. The plot consists, for each deposition time, of reflectivity values varying together with the angle (2θ) of reflection. Such plots do not give quantitative results, but have to be analysed through BEDE MetrixL software; information on thickness, roughness and density can be derived by fitting the curves.

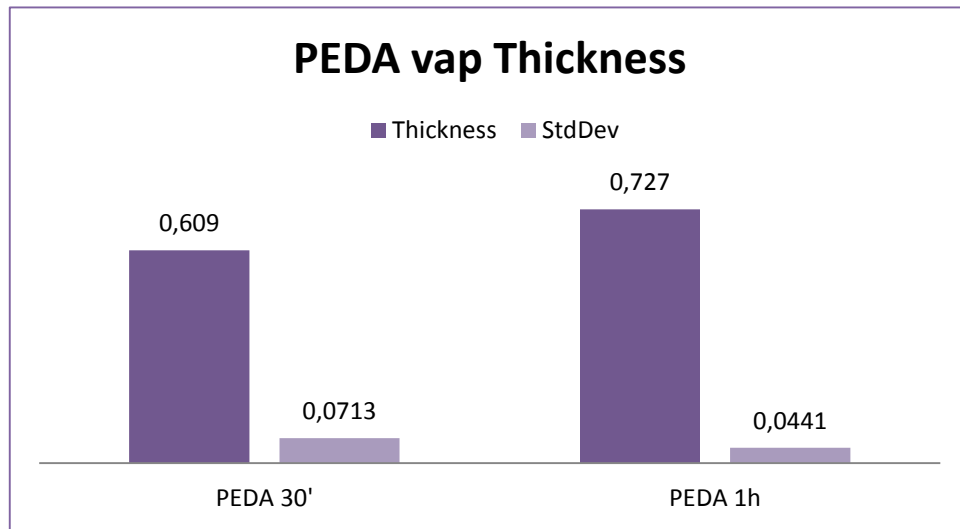


Plot 4.2 - XRR plots of PEDA SAM for different deposition times. The plot is presented in terms of reflectivity value of the x-ray vs the angle (2θ) of reflection.



Plot 4.3 - Thicknesses values of PEDA vs time. Two different measures, made with two different measuring systems are presented: one through XRR, one employing ellipsometry.

Plot 4.3 presents the thicknesses values versus the deposition time along with the density values considering the same deposition times. Although the values are not always consistent between the two instruments, due to the different measuring systems and the fitting software, a good trend can be seen from both curves.



Plot 4.4 - Thickness value, measured through F5 instrument for deposition times of 30' and 1h.

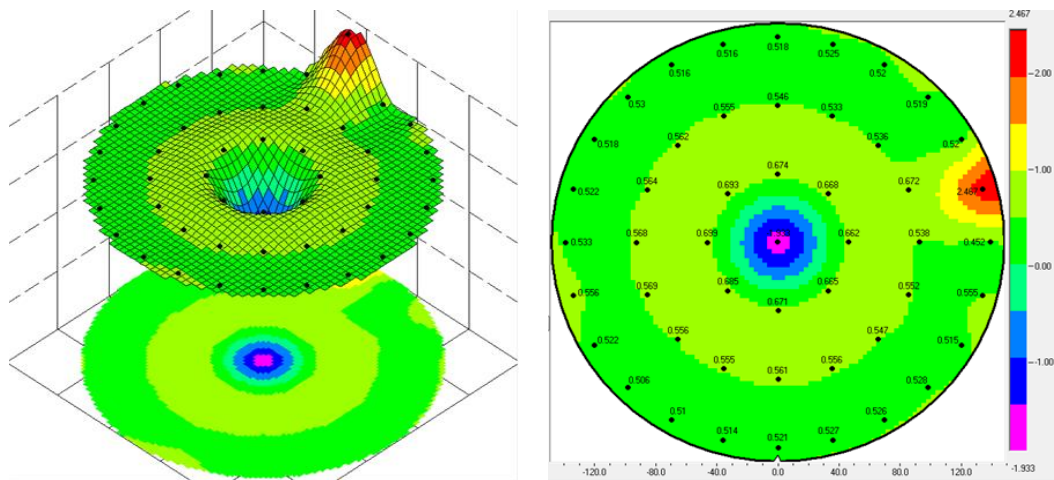
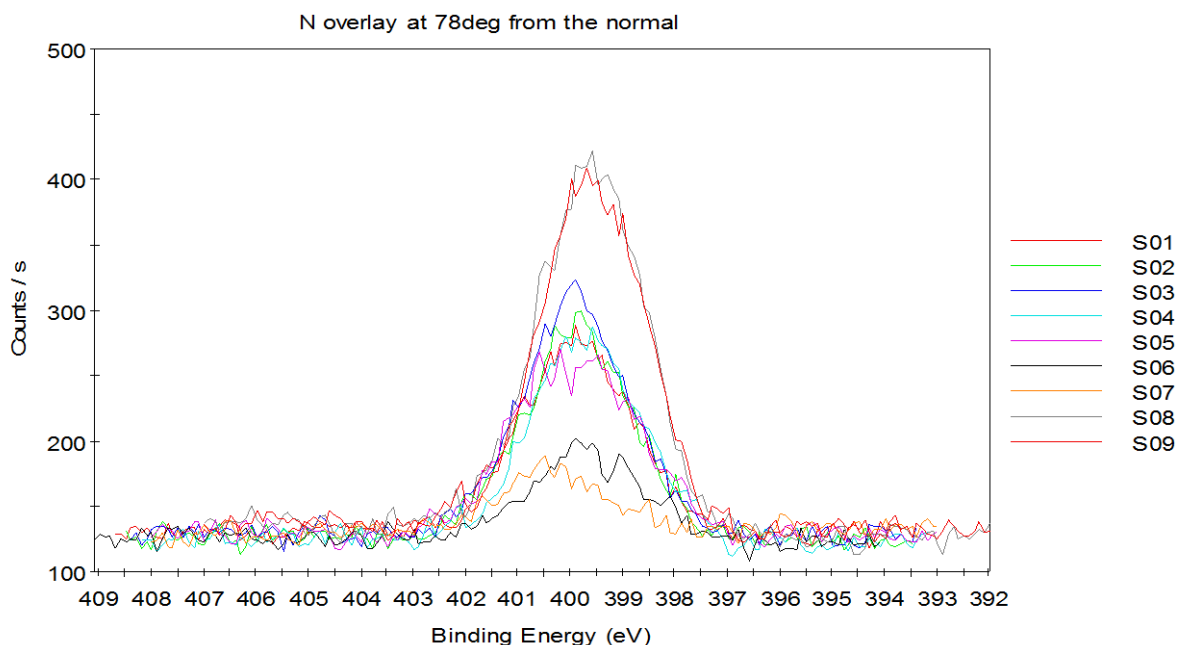


Figure 4.2 - Example of thickness data collected by the F5 tool.

The thickness increases from the shortest deposition time towards an asymptote that is approached already around three hours of processing. The asymptotic value stands at c/a 1.4 nm. The situation appears slightly different for the vapour deposited SAM: the CA indicates an hydrophilic behaviour that match the results find in the literature indicating a good deposition, but the thickness instead is c/a half of the attended one (plot 4.4).

Another very important measurement that has been made on PEDA is the XPS spectroscopy. The measurement has been done to compare the relative quantity of the groups and elements present on the surfaces. When this type of measurement is made, spectra are obtained, like the one represented in plot 4.5. The monochromatized aluminium $K\alpha$ X-ray source (1486.6 eV) was employed, with a spot size of 400 microns. Standard sensitivity factors were used to convert peak areas to atomic concentrations. As a result of this, it is possible that the concentrations deviate from reality in the absolute sense (generally not more than 20% relative). Figure 4.6 shows an example of such spectra.



Plot 4.5 - Atom count versus the bonds binding energy: from these plots it is possible to have an estimation of the atomic percentages in the surface.

Here we present the data on vapour PEDA (table 4.3), since the results on the liquid one was evaluated in a previous study. The acknowledgement of the deposition that may offer the highest amount of reactive sites is crucial for the study.

Table 4.3 - Atomic concentrations of the elements found on the surfaces.

description	C1s tot	N	O	Si2p3	SiO2
PEDA vap 30'	12.4	0.86	26.44	49.4	10.9
PEDA vap 1h	17.05	0.45	26.07	45.29	11.15

Between the 30' and the 1h deposition the concentration of N atoms has diminished by half. It should be noticed, as a term of paragon, that the concentration of surface N atoms on liquid PEDA (experiment made in a previous study) was as high as 3.5%⁷².

4.2.3 Discussion

PEDA SAM was intensively evaluated through the use of CA, XRR and XPS. The liquid deposited organic layer shows a “near-zero” value thickness, around 1.4 nm, as it was required. The value, as it can be seen from plot 4.3, is achieved around a deposition of 2 hours, indicating a correct alignment of the molecules on top of the substrate. A longer deposition show no hint of a multilayer deposit and instead could be useful for an increase packing of the precursor molecules in order to achieve a compact and dense layer (density up to 89%). The 1 hour deposition is probably not sufficient to allow the molecules to stand up and pack together. The molecules are lying down on the surface, not giving the hoped barrier properties. This phenomenon could be responsible for the thickness value around one nm.

The solution work very efficiently: if a first deposition of molecules is favoured, giving rise to a monolayer, the successive deposition is hindered and there was no hint of the formation of a multilayer.

If the result of the liquid deposition are promising, the behaviour of the vapour one is more hard to understand. CA, for the 30' deposition, is in line with the liquid one but the 1h deposit shows an increase up to 73° indicating a change in the layer structure. The measured average thickness is quite low, if compared to the liquid one: this could be indicating a packing of the molecules not complete like in the case of the case of the 1 hour deposition. Also, as seen from the XPS data shown in table 4.3, the 30' deposit shows a higher quantity of top N atoms, indicating a higher packing: a longer deposition seems to affect negatively the deposit itself, just unlike the liquid case. The higher value is anyway much lower than the previously measured one in the case of liquid DETA.

4.3 DETA

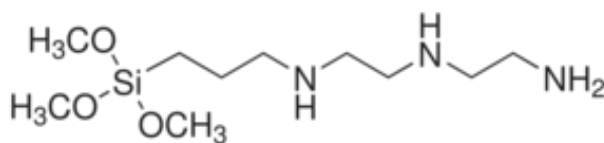


Figure 4.3 - Chemical structure of DETA

4.3.1 Materials and Methods

4.3.1.1 Sample preparation

The (3-Trimethoxysilylpropyl)-diethylenetriamine (DETA) SAM, was deposited as an alternative organic barrier layer for the first time during this work. The obvious choice was then to employ the same technique successfully used for the PEDA liquid deposition, also for DETA. The result, as we will see in the next pages, is very promising.

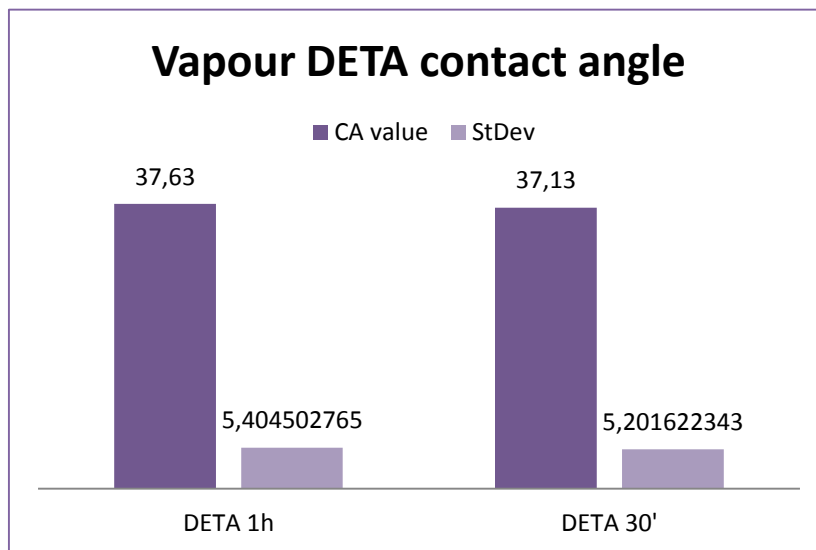
4.3.2 Analysis and Results

Contact angle measurements were made, as before, employing water as sessile liquid and are presented in table 4.4.

Table 4.4 - CA values for liquid deposited DETA

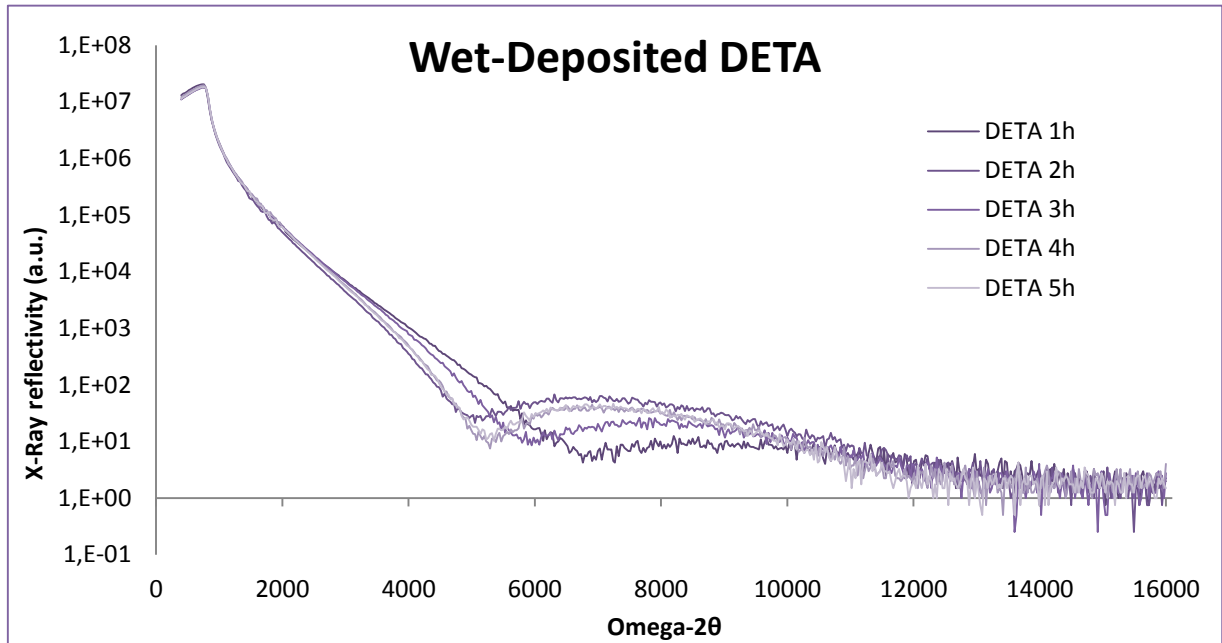
Deposition Time	CA value	st.dev.
DETA liq 1h	62.22	3,20587
DETA liq 3h	58.5	2,519524
DETA liq 4h	57.74	2,97765
DETA liq 5h	56.42	0,231517

The CA appear to stabilize, after 5 hours of deposition, around a value of 56.4°. The value seems legit, according to the values found in literature¹¹¹.

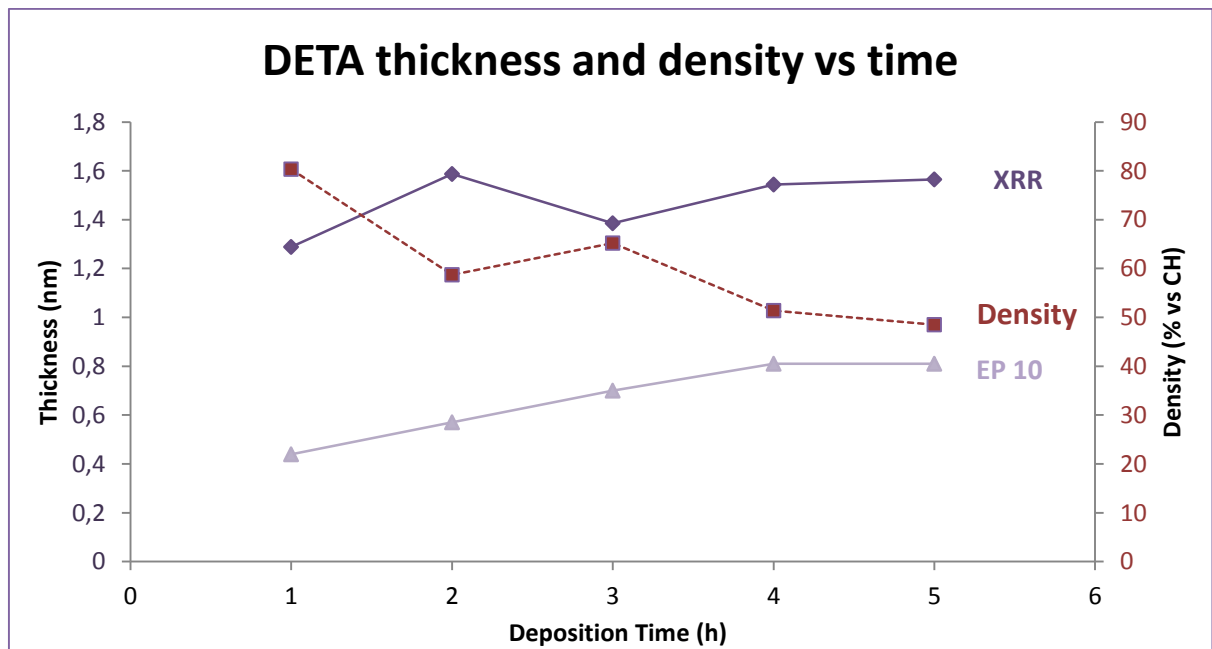


Plot 4.6 - Contact angle values of vapour deposited PEDA, for 1h and 30' deposition.

CA value found for DETA SAM is quite surprising: the layer seems to be very hydrophilic, much more than the liquid deposited one, with the value not so different between the 1h and 30' deposition, around 37.5°. In plot 4.7 instead the XRR plots are presented. The curves appear to follow a nice regularity. The following data, extrapolated from the fitting of these results are shown in the following plot 4.8. Just as before the data is confronted with the one given from the EP10 ellipsometry system. Density is also shown in the plot.

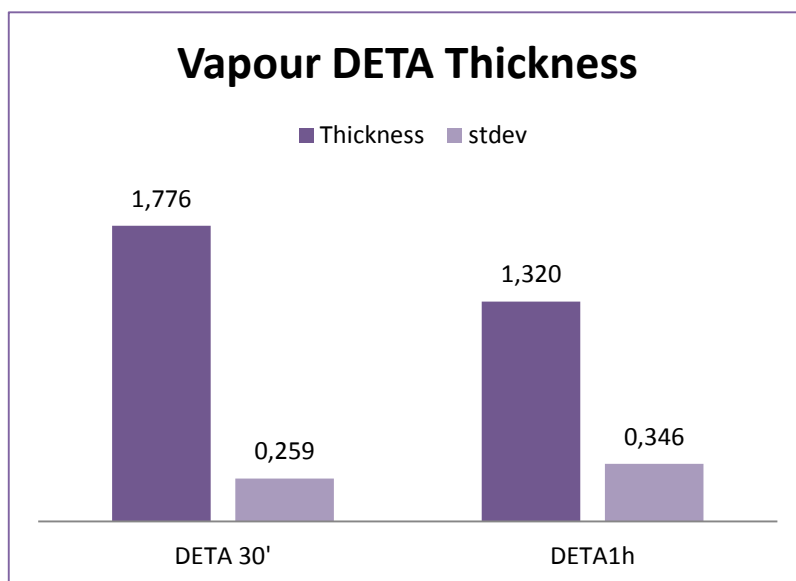


Plot 4.7 - XRR plots of DETA SAM for different deposition times. Like plot 4.1 every curve represent, for every a different deposition time, the reflectivity vs the angle (2θ) of reflection.



Plot 4.8 - Thicknesses values of DETA vs time. The two different measures, made through the use of the XRR method an Ellipsometry presented: one through XRR, one employing ellipsometry.

The data appears very different using the two evaluation methods. Anyway the same trend is noticed in both the plots, with the thickness reaching a constant value after 4 hours of deposition. This value is around 1.65 nm, reading the XRR data, it is 0.81 nm according to the EP10 tool. Like the previous case, also DETA reaches a near-zero thickness, essential requirement for the development of a new organic barrier layer.



Plot 4.9 - Thickness value, measured through F5 instrument for deposition times of DETA of 30' and 1h.

Vapour SAM appears to have a thickness more similar to the data collected by the XRR measurements. Also, the value of thickness decrease with an increasing deposition time.

Finally, the XPS data is presented on atomic concentrations on the surface of the samples. The data includes the liquid DETA, the vapour deposited one and, for the sake of completeness, also the previously shown data on vapour PEDDA.

Table 4.5 - Atomic relative concentrations of species on the coupons.

Sample	C1s tot	N	O	Si2p3	SiO2
DETA liq 1h	13.68	1.68	36.24	31.72	16.69
DETA liq 2h	13.67	2.16	36.65	31.08	16.45
DETA liq 3h	12.28	2.28	36.47	32.08	16.88
DETA liq 4h	12.68	1.84	36.87	32.2	16.41
DETA liq 5h	14.73	2.64	38.9	27.96	15.77
DETA vap 30'	23.04	5.31	25.33	35.57	10.75
DETA vap 1h	20.05	4.65	26.11	37.74	11.44
PEDA vap 30'	12.4	0.86	26.44	49.4	10.9
PEDA vap 1h	17.05	0.45	26.07	45.29	11.15

Looking at the trend for the liquid deposition, it appears that, apart from the shortest deposition, the N content seems independent from the deposition time. The value achieved in the vapour deposition is quite higher with respect to the liquid one, while, in the case of PEDTA this value is far smaller. In both the vapour cases, a higher number of N atoms is achieved at 30', while it decreases quite evidently in 1h deposition.

4.3.3 Discussion

As before, the liquid deposition appears to have a more understandable behaviour. A longer deposition is needed to achieve a stable organic (around 4h) with respect to the PEDTA deposition. The asymptotic value reached is not clear: depending on the measuring instrument this could be 0.81 or 1.5 nm. Anyway, the trend shown by both measuring tools is the same and a low thickness barrier layer is anyway achieved. Still, a longer deposition brings the density of the layer to a more

constant value, giving a rise of N atoms on the surface of the SAM up to a value of 2.64%. The value appears lower than PEDA (3.5%) even if DETA is a tri-amino tailored SAM, while PEDA has just two final amino groups. This could suggest a lower overall density of the DETA layer than the one of PEDA.

Vapour deposited DETA appears much more promising than his PEDA colleague. The CA value is very low, around 37°. This could be a sign that a very dense layer is reached, with the three amino groups sticking out of the film, giving the low CA value and explaining also the very high quantity of N atoms in the vapour deposited SAM seen from the XPS data in table 4.5. The thickness of the layer, of 1.7 nm and 1.3 nm for the two deposition times, is similar to the XRR data for the liquid deposition. It should anyway be noticed that full wafer deposition is much more uneven on such a large substrate, and all the values shown in this paragraph is always a result of an average made on all the data collected.

4.4 Observations

Two different self-assembled monolayers were analysed in this chapter, following two alternative deposition processes: a more well-known liquid deposition and a promising vapour one. Since the aim of the organic layer is to provide a suitable substrate for the anchoring of the Pd atoms, apart from its role as barrier, the aim of this part was to understand which deposit could better accomplish such role. With a 5.31% of N atoms on the top surface of the vapour DETA 30' deposition, the SAM appears to be the most promising. It can already be anticipated that the high value of N atoms will be also confirmed in the next section, where DETA vapour 30', will achieve the best results in terms of Pd uptake. Anyway, it should be noticed that the vapour deposition mechanism is not completely understood and additional studies should be necessary to complete the knowledge void. Considering the liquid deposition, PEDA seems to achieve better results, with a layer forming and well-packing already after 2 hours of deposition and with a percentage of N

surface atoms that goes up to 3.5% for a 5 hours deposition. The value is quite surprising considering the lower amount of amino- groups possessed by the PEDA precursor with respect to the DETA SAM precursor, which contains three of them, reaching a highest value of 2.64% for the same deposition time and processing. The DETA film, deposited from liquid solutions, does not show the hoped densities and catalysing abilities, even if it can be still considered a good barrier layer. A more complete comparison will be made when coupled with the metal layer. Overall, liquid PEDA appears more promising, reaching higher density values and thickness consistency over different deposition times as evaluated through XRR. On the contrary, obtaining the same layer properties with a vapour deposition appears much more complex.

Chapter 5: Electroless Deposition **of NiB on SAM**

The next step on the road to the formation of a complete interconnection system is the deposition of the metal over the barrier layer. The chapter will then be focusing on the metal deposit characteristics and properties by presenting the results achieved through the experiments realized in this work.

5.1 Introduction

The chapter can be broadly divided in three main parts. The first part will not be focusing on the metal per se but more on the catalyser. The palladium deposit on the SAM will be under focus to evaluate the situation where the highest amount of catalyser deposition is achieved. This was made through the use of XPS spectroscopy. The second part will be focusing on the NiB layer: analysing thickness and measuring resistivity with different deposition times, the characteristics of the deposit will be under consideration. Finally the best deposit, combined with the best organic barrier layer will be used to evaluate the line resistivity on patterned silicon.

Main goal of the deposition is to achieve a metal that may work as a good barrier layer metal, actively contributing to the overall conductivity of the interconnection, or autonomously compete with the other metal currently employed in the interconnection industry. Along with low resistivity, essential for both tasks, the metal has to respect some other process conditions that will have to be evaluated. A part from the requirement of blocking the diffusion between silicon and NiB, also good conformity is appreciated while high thicknesses are reached, essential for a

good CMP process. The adhesion is also an important feature of the film since the next processing steps in the IC industry have high requirements in terms of mechanical solicitation. All these characteristics were evaluated and are exposed in the following paragraphs.

5.2 Palladium deposition

The study of Pd deposition is made through the use of a PdCl₂-based commercial solution provided by LAM[®] Research while the measuring system (Atomika TXRF8300W) was described in 3.6.

5.2.1 Materials and Methods

5.2.1.1 Sample preparation

3x3 cm² coupons of silicon have been prepared for the experiments. Following the conventional cleaning steps both SAMs, PEDA and DETA, were deposited on the coupons with the liquid processing time ranging from 1 hour to 5 with steps of 1 hour. The vapour deposition instead followed the conventional 30' and 1 hour deposition. The Pd deposition was carried in 4 successive steps:

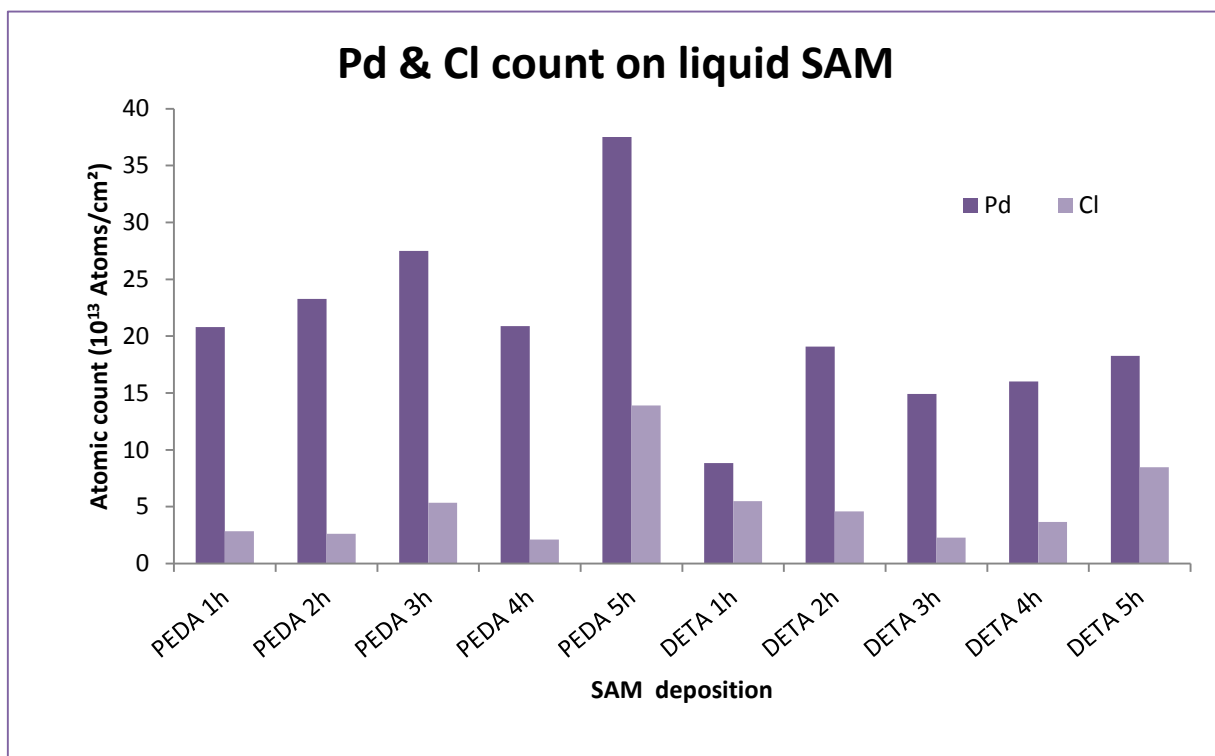
- Rinse in DIW, 30'';
- Immersion in the PdCl₂ solution, 5';
- Rinse in diluted Additive M, 2';
- Final rinsing in water 30''.

The rinse in Additive M (provided by LAM[®] Research and whose composition is unknown), diluted in water with the same concentration as the one present in the metal depositing solution, is

necessary for the partial removal of Cl cluster on top of the surface. The chloride has to be removed as much as possible because it pollutes the metal depositing solution, accelerating the degradation of it, and would also diminish the metal characteristics. The 5' immersion in the palladium solution was developed in previous studies and has been maintained.

5.2.2 Analysis and results

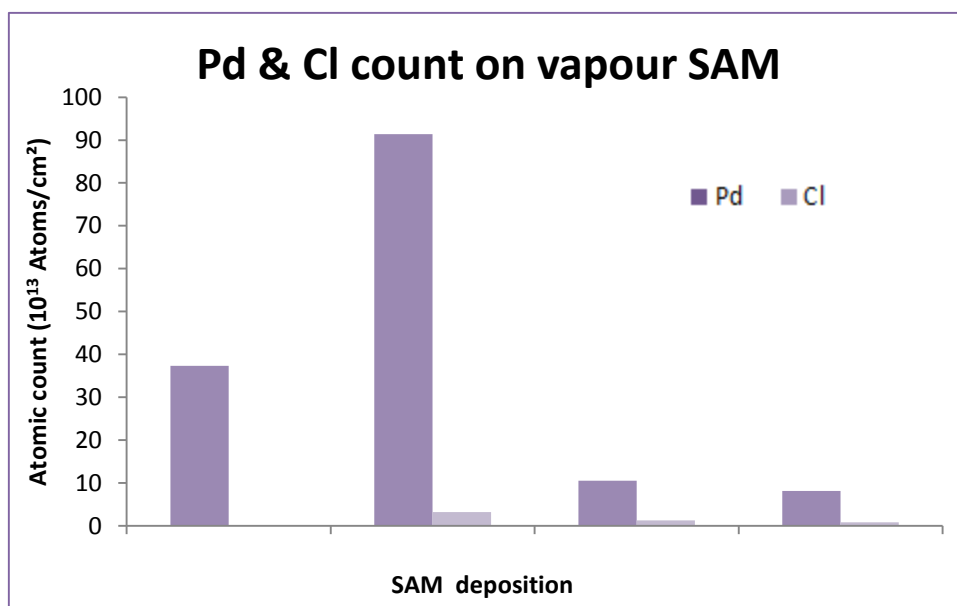
The results on the liquid deposited SAM are illustrated in plot 5.1.



Plot 5.1 - Atomic count of Pd and Cl atoms after palladium deposition on liquid SAM.

From plot 5.1, an increasing trend of PEDDA can be seen, with a maximum value reached for the 5h deposition. For the liquid DETA instead the palladium concentration is more or less constant from 2 to 5 hours of deposition. Similar trends are assisted considering the Cl content.

Uptake data in the case of vapour deposited SAM, is instead illustrated in plot 5.2. While, for DETA, the quantity of Pd is more than halved by doubling the deposition time from 30' to 1h, for PEDDA the value remains circa constant with different deposition periods. The higher amount of Pd in the DETA case is evident from the plot (nearly one order of magnitude higher), while the Cl content on the 1h DETA deposition was not evaluated due to a surface concentration lower than the minimum quantity for the instrument ($<760 \cdot 10^{10}$ atoms/cm²).



Plot 5.2 - Atomic count of Pd and Cl atoms after palladium deposition on vapour processed SAM.

5.2.3 Discussion

The deposit has been everywhere successfully completed with a bright and smooth surface, suggesting the absence of big cluster formation that would be causing an uneven metal film deposition. Longer period appear to be favouring the Pd acquiring on liquid PEDDA ($3.5 \cdot 10^{14}$ atoms/cm² at 5h deposition), while instead no big difference is noticed in the liquid DETA for the conventional deposition times of 2h up to 5h (always between $1.5 \cdot 10^{14}$ and $2 \cdot 10^{14}$ atoms/cm²).

It should be noticed that the Pd uptake in liquid DETA follows the same trend as the quantity of N atoms found on the top of the same organic layer, as it is shown in table 4.5. The higher count on the liquid PEDDA layer is probably due to a higher packing of the organic molecules that permit the binding of a higher number of the Pd atoms. Comparing, as before, the result of the Pd uptake with the quantity of N groups of the SAM, previous studies have shown how the percentage of amino- groups on top of PEDDA is higher than DETA (3.5 vs 2.64 at 5h liquid deposition). This explains the better results of PEDDA with respect to DETA in the palladium uptake.

If in the liquid case a better job is achieved by PEDDA, even if the difference is not so evident between the two SAMs, in the vapour deposition process far better results are measured for DETA than for PEDDA. Also, as expected, the 30' deposition seems to be more useful than the 1h one.

5.3 Electroless Deposition of NiB

The work described in the previous chapter, involving the two organic self-assembled monolayers, PEDDA and DETA, that were employed in this work and with the Pd uptake analysis, gave good results for both the films. Therefore, both SAMs were employed in the successive metal deposition steps. This chapter will be presenting the most important results that were achieved in this central part of the project, that's to say the electroless deposition of NiB.

5.3.1 Materials and Method

5.3.1.1 Sample preparation

As already said in the previous chapters, during this project two different ELD solutions were used. The exact composition of the solutions is an industrial secret belonging to *LAM® Research*,

therefore not know, but the main compounds that are present can be exposed. The two solutions are so composed:

- **NiB 10%:** 12.5ml of PuNic (*LAM® Research*), 60 ml of AddB (*LAM® Research*) and DIW up to 300 ml.
- **NiB 1%:** 13 ml of PuNic (*LAM® Research*), 17 of AddM (*LAM® Research*) and DIW up to 300 ml.

It is known that PuNic contains a nickel salt and dimethylaminoborane (DMAB) that acts as the reducing agent and which contains the boron present in the film.

The ELD on organic layer is a multiple step process: these steps are illustrate in figure 5.1 and are later explained.

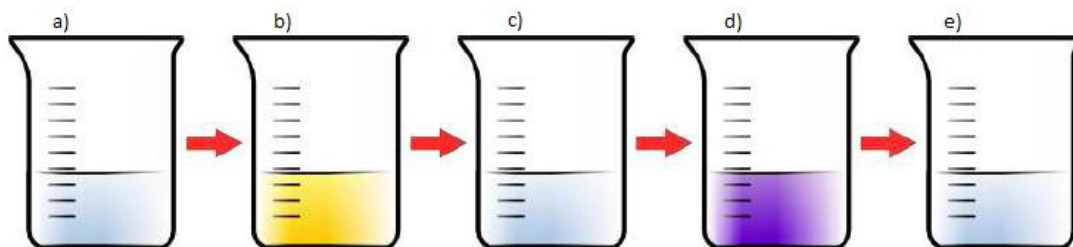


Figure 5.1 - Representation of the ELD steps. a) DIW rinse. b) Immersion in PdCl₂. c) Pre-rinse in DIW & Additive M/B. d) NiB solution immersion. e) Post rinse in DIW.

The first rinse is necessary to wet the surface and give a pre-clean to the substrate before it is immersed in the catalytic Pd-based solution which is easily deteriorated. A pre-rinse in the DIW/Additive solution is necessary to remove the chloride deposited on the substrate and for the removal of physisorbed Pd atoms: these atoms decrease the properties of the metal deposit because are not strongly bonded to the substrate and also, if released in the bath, contribute to the pollution of the NiB solution, making the reaction start on the substrate but also in the bulk of the solution. A post rinse is used to clean the top metal layer just formed. The NiB deposition is quite complex and has to be controlled accurately: a good agitation is necessary to remove the

H₂ bubbles that are formed during the deposition process. These bubbles decrease the properties of the growing layer due to the formation of voids in the film and may also be a cause of hydrogen cracking in later stages.

It should be noticed that in the previous process the pre-rinse step was carried out in pure DIW. During the development of this project it was noticed that a pre-rinse in a solution DIW-based with Add M or B (depending on which NiB solution was used) with the same concentration as the following depositing solution, gave better results in terms of fast growth and resistivity of the metal layer.

The deposition steps, from the first pre-clean to the post-rinse was carried out inside the glovebox in picture 3.12.

5.3.1.2 Analysis techniques

The growth of the metal was analysed in order to have a better understanding of the deposition process, using mainly x-ray reflectivity as characterization method. The resistance was evaluated for different thicknesses so that the condition to have the best conductivity could be achieved. The four point probe, in the line arrangement, has been used for this purpose. Together with these important results, other properties have been evaluated and will be presented in the following pages.

5.3.2 Thin Film Resistivity

5.3.2.1 Process description

In the first part of this project the goal was the measurement of the metal thin-film resistivity. A high number of 3x3 cm² coupons were produced in order to cover all possible range of

deposition options so that a complete overview of the process could be reached. The results on the liquid SAMs are exposed first, just after the one on the vapour deposited one. The deposition options, presented during the deposition of the barrier and metal stack, regarded:

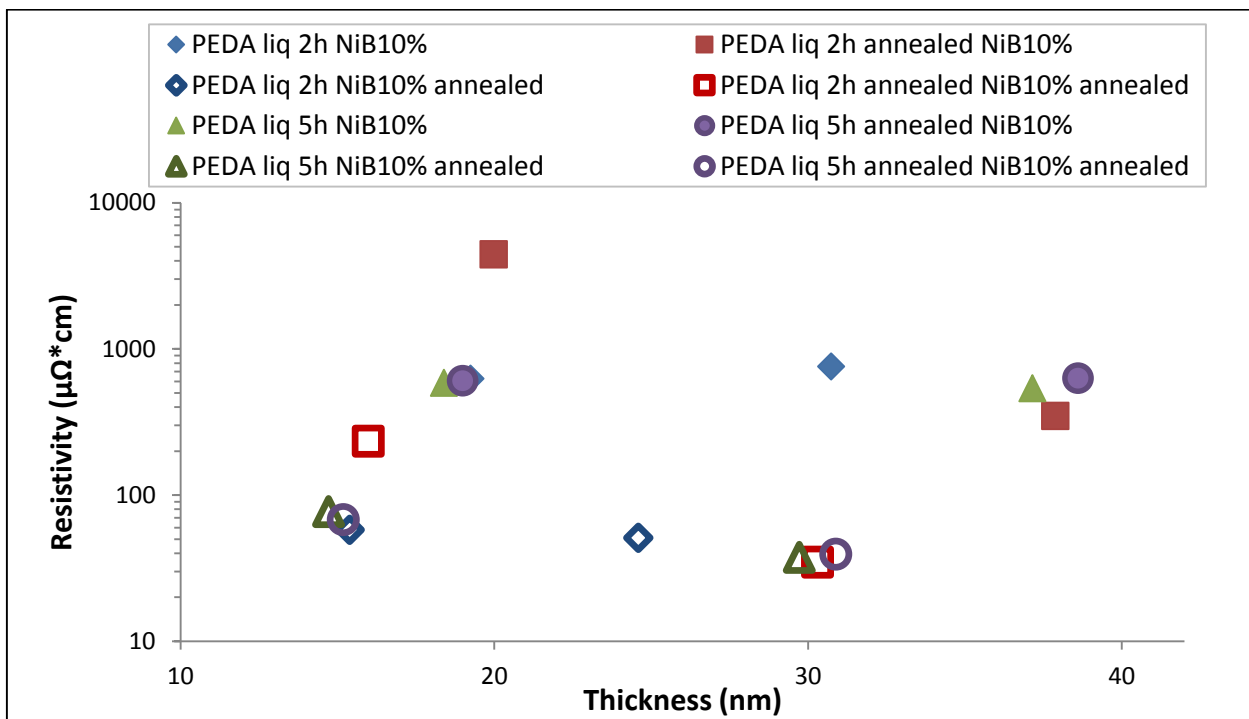
- the significant deposition times of the SAM;
- whether or not anneal the samples post SAM deposition;
- which NiB ELD time was most significant;
- the understanding of the effect of the metal annealing.

Since no decision could be made a priori, to have a full cover of all possibility all deposition specifics were covered. The SAM layer was processed with two significant deposition times: 2h and 5h, so that the range of successful organic layer depositions is covered. Copies of the same blanket were produced so that half could go through the SAM annealing step while the other half did not. Also two deposition times were used in the metal deposition step: 3' and 6' were used for the 10% NiB chemistry while for the 1%, 6' and 12' were considered more significant. This is because of the highest amount of additive in the 10% chemistry is expected to cause a boost in the deposition rate. Resistance and thickness were first evaluated on these coupons, while later they underwent an annealing step. Resistance was so evaluated also post-anneal while a nominal decrease of thickness was assumed due to a recrystallization event during the annealing phase.

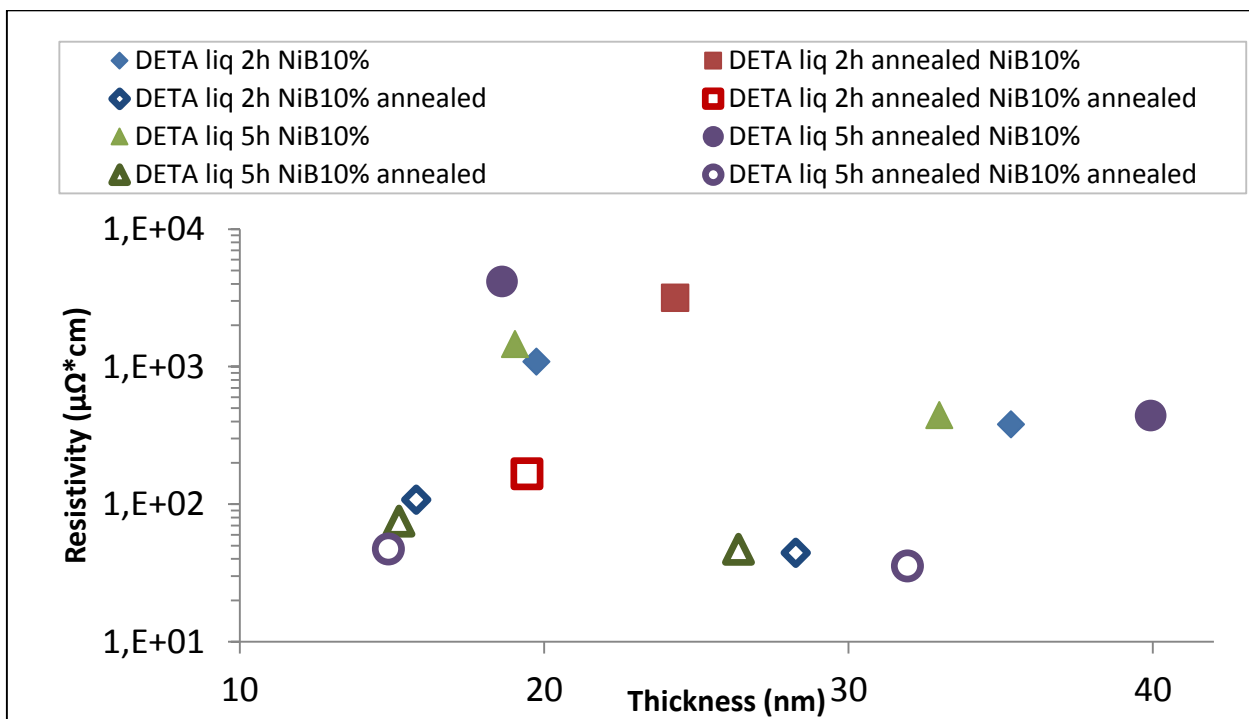
SAM Anneal was carried out at 120 °C, for 15 minutes under a N₂ flux. The temperature was chosen after previous studies have demonstrated that it did not affect negatively the organic layer. The metal anneal was made in a heatpulse anneal oven at the temperature of 350 °C for 15 minutes in a forming gas (FOG) atmosphere. At this temperature the SAM layer should be able to prevent interdiffusion while crystal reorganization is happening. A reduction of the 20% was taken in account with the annealing process, due to crystalline rearrangement.

5.3.2.2 Results presentation

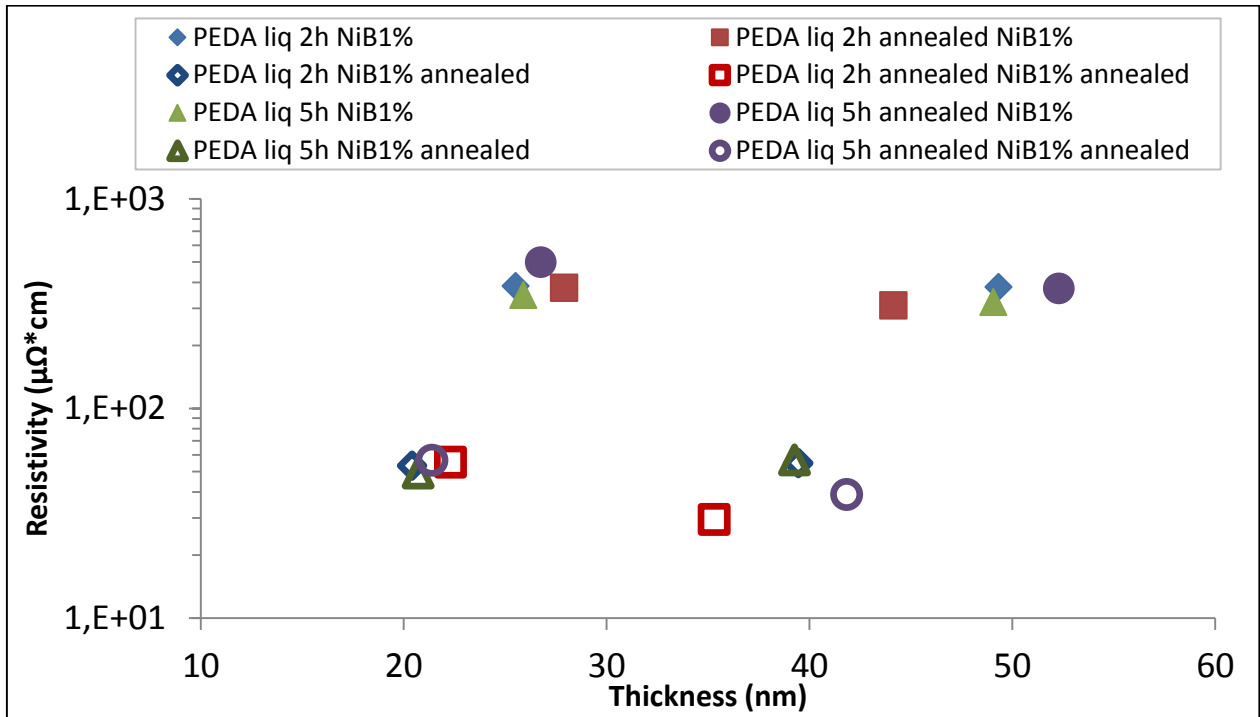
In the following graphs, all the data collected on the resistivity of NiB films, for different thicknesses is illustrated. The value obtained for every coupon is the result of the average made on 5 measurements made on each single specimen.



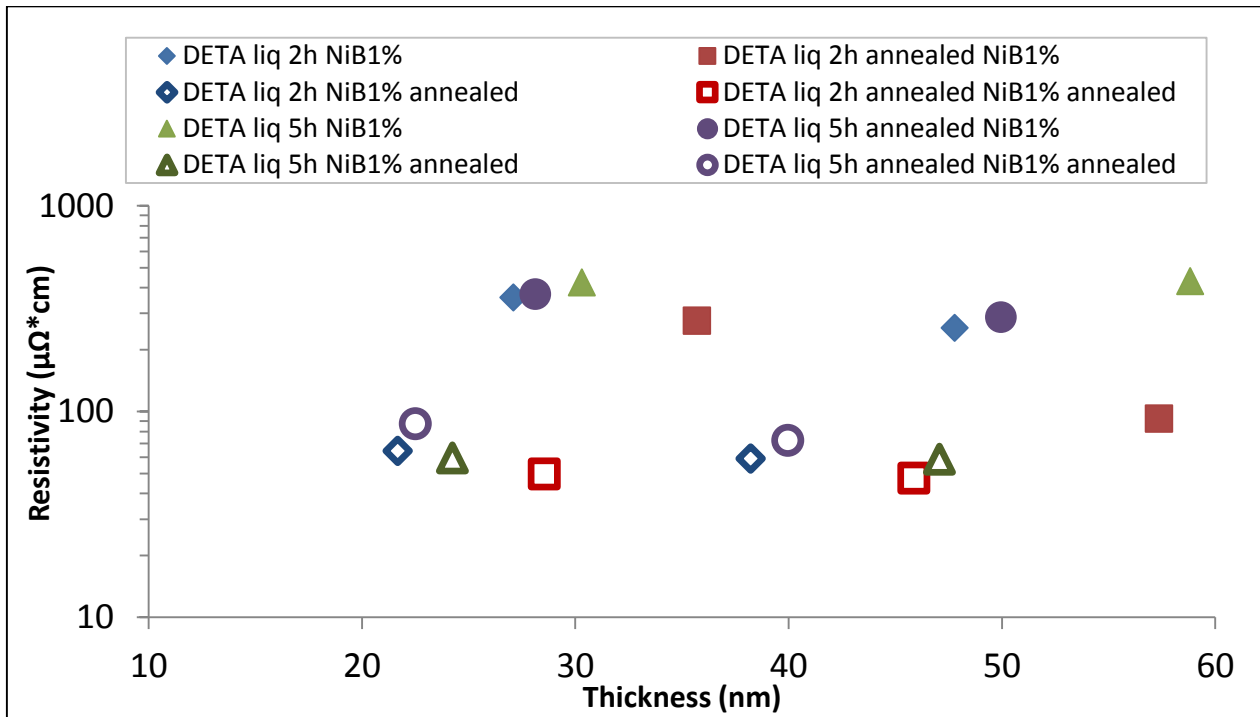
Plot 5.3 - Resistivity data of NiB10% processed on PEDA liq 2h and 5h.



Plot 5.4 - Resistivity data of NiB10% processed on DETA liq 2h and 5h.



Plot 5.5 - Resistivity data of NiB1% processed on PEDA liq 2h and 5h



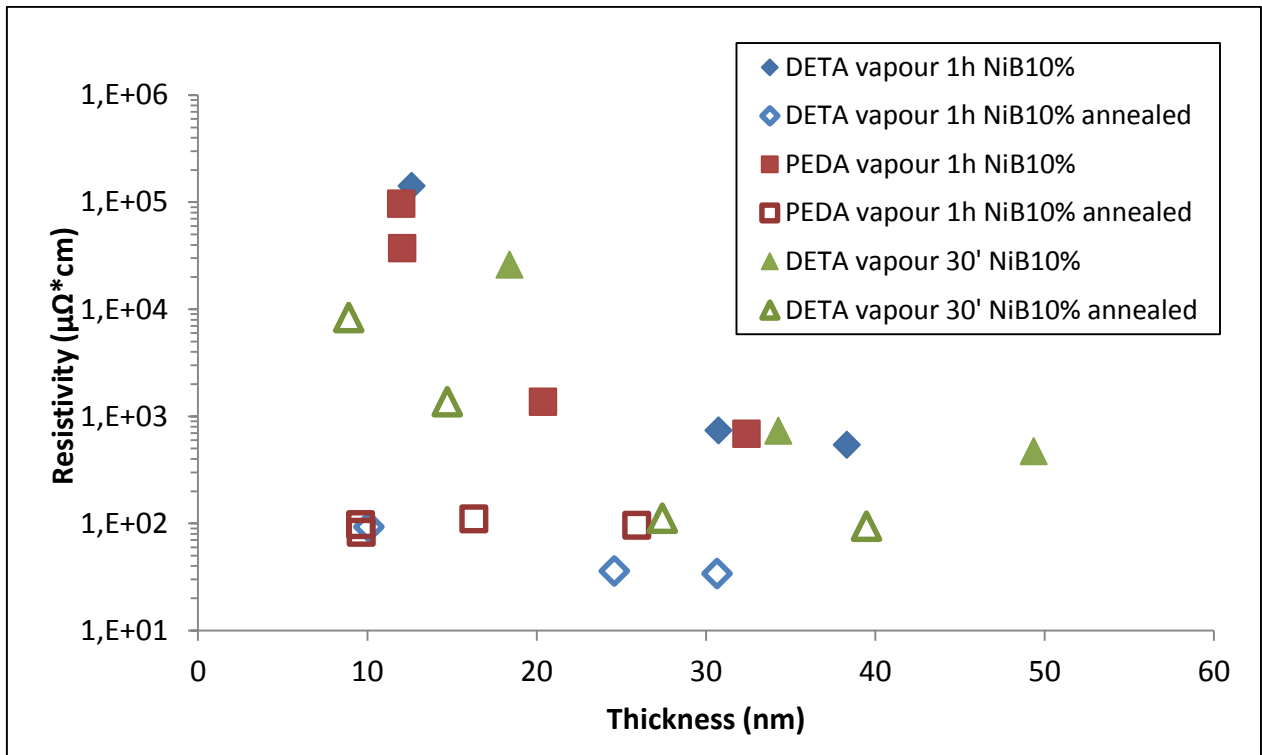
Plot 5.6 - Resistivity data of NiB1% processed on DETA liq 2h and 5h.

Plot 5.3 and 5.4 describe the values of resistivity calculated in such way:

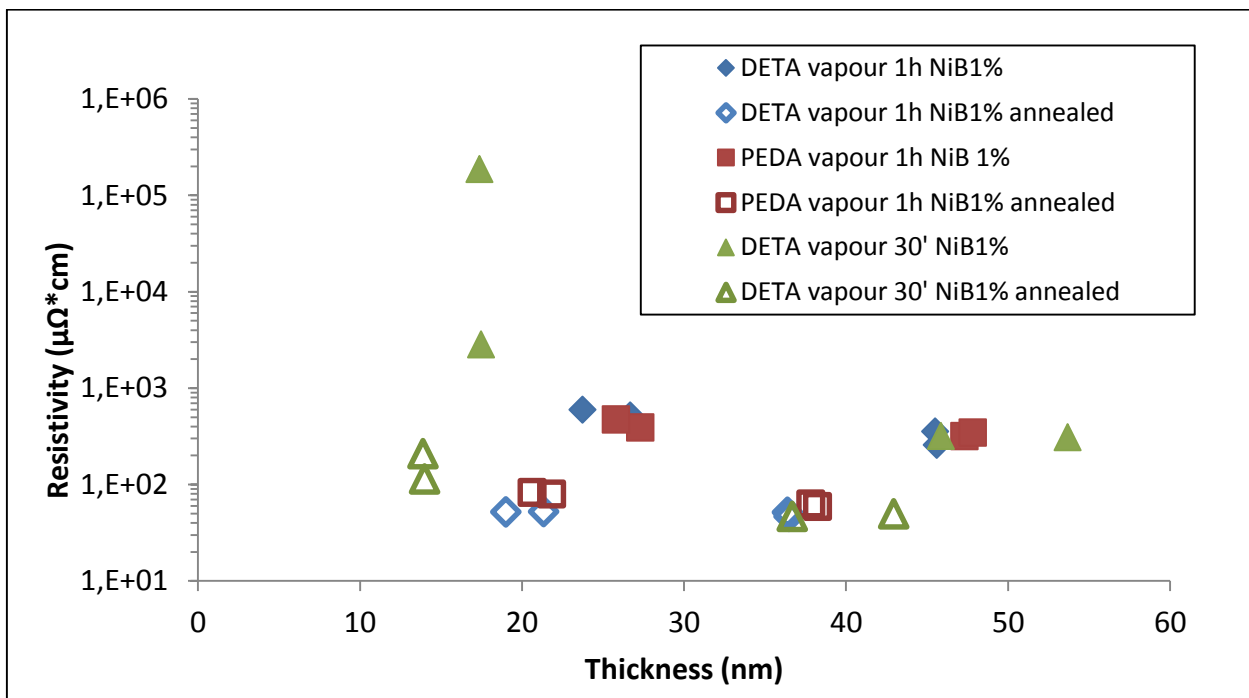
$$\rho = R * T$$

where ρ is the resistivity in the graph, R is the resistance values measured on the coupon and T is the XRR measured thickness. As a confirmation of the goodness of the metal film, the density of it is always higher than 75% of the nickel one. Also it should be noticed that the process is time-controlled: it is understandable then why thicknesses appear scattered through the graph and not at the same value of the abscissa.

The data collected on vapour coupons are also presented (plot 5.5 and 5.6):



Plot 5.7 - Resistivity data of NiB10% on vapour deposited (1h and 30') PEDDA and 30' DETA



Plot 5.8 - Resistivity data of NiB1% on vapour deposited (1h and 30') PEDDA and 30' DETA.

5.3.2.3 Discussion

Good results in terms of low resistivity are achieved on most of the liquid coupons, decreasing after anneal. Both DETA 2h anneal and PEDDA 2h anneal show lower resistivity with respect to all the other coupons: the anneal of the organic layer does not seem to give advantages on the subsequent metal deposition. Overall longer processed PEDDA and DETA SAM (both 5h) show lower resistivity of NiB than the 2h processed. Also, as expected because of the higher boron content, the NiB10% chemistry shows worse conductivity properties than the NiB 1%. It can be deduced that longer processed SAMs, with higher densities and packing coefficients, work as better substrates for the NiB layer; higher is the B content and higher will be the resistivity.

In the vapour case, the two chemistries seem to have different behaviours on same substrates: while the 10% NiB show very good results on PEDDA and DETA both 1h deposited, with a very

high resistivity on the DETA 30' deposition, The 1% NiB present good results everywhere, but especially low resistivity values, for very thin films, for the 30' DETA SAM.

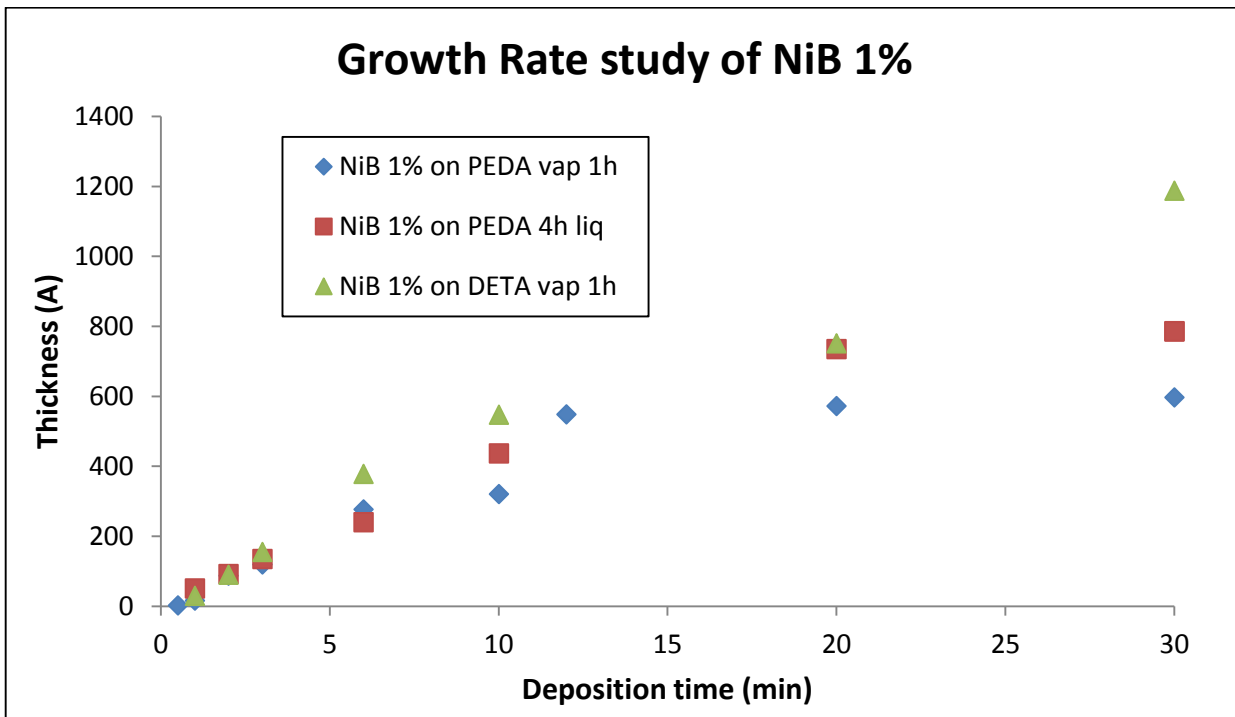
5.3.3 Growth Rate Evaluation

5.3.3.1 Process description

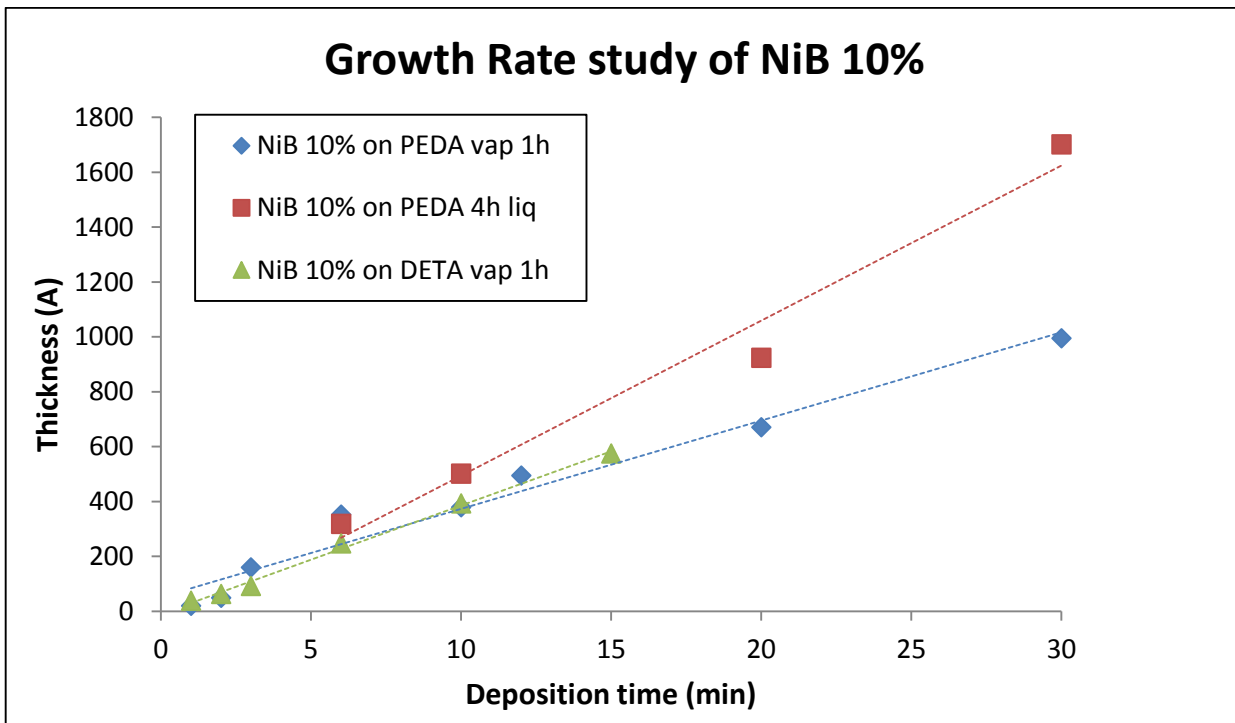
A series of 3x3 cm² coupons have been produced with vapour-deposited SAM with the goal of better understand the metal deposition. The deposition steps, options and characteristics are the same as the ones described in the first part of the previous paragraph. Two types of coupons where used, one with PEDA and one with DETA, both deposited for one hour from vapour phase. A third type of deposition (liquid-deposited DETA for four hours) was used as a benchmark.

5.3.3.2 Results presentation

In plots 5.10 and 5.11 thickness data is plotted versus the deposition time. The thickness was evaluated through XRR analysis.



Plot 5.9 - Growth rate study of the NiB 1% chemistry.



Plot 5.10 - Growth rate study of the NiB 10%. The black lines represent the three linear trend lines.

5.3.3.3 Discussion

The two graphs shows little but remarkable differences. The growth rate of the NiB 1% seems to reach a limit, or a very low growth rate, for deposition times higher than 15 minutes. This is especially true for the PEDA SAM (both liquid and vapour deposited) and also for DETA, even if in this case this reduction is less evident. No reduction in the growth rate is instead show for the 10% chemistry. Thicknesses up to 180 nm are reached for a 30' deposition while in the case of vapour PEDA plus NiB 1% not even 60 nm could be reached.

Another important aspect is the actual evaluated growth rate. In the case of NiB10% we would have expected a higher growth rate, due to a higher presence of additive that should boost the deposition process. This is not true in practise: with a rate of 3.4 nm/min and 3.8 nm/min in the case of respectively vapour PEDA and DETA, the growth is much slower than in the case of the NiB 1% where values, for the first 10 minutes, that's to say before the deposition strongly slows, the respective values are 4.1 nm/min and 5.2 nm/min.

5.3.4 Adhesion Evaluation

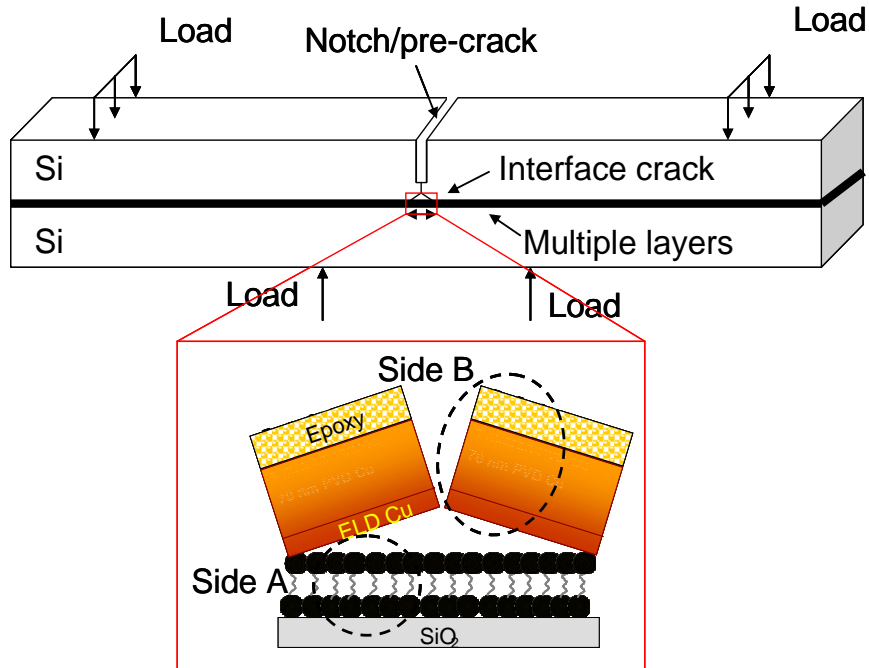


Figure 5.2 - Representation of the crack created to estimate the adhesion of the metal layer.

The adhesion measurement is an important step in the realization of a good barrier/metal stack. A low value in adhesion can cause lifting issues like the one pictured in figure 5.3: the deposition was carried out on a different substrate.

The experiment is carried out through the use of a 4-point bending tool, with a metal layer that has been previously capped with CVD silicon oxide and epoxy silicon. On this sandwich structure a small notch is made to force the crack to start from a specific point, as it can be seen from figure 5.2. Once the piece is broken the evaluation of the strength necessary to break it is a direct consequence of the adhesion energy of the weakest interface. Instead, through a chemical analysis of the fracture planes, a better understanding of which interface represent the lower adhesion properties can be made. In this case, plots like the 5.8 one, is obtained with different peaks, corresponding to the different chemical species found on the two fracture planes. The

green line correspond to a non-etched surfaces while the green plot correspond to a surface that underwent an etching step to evaluate which species actually remained on the surfaces.

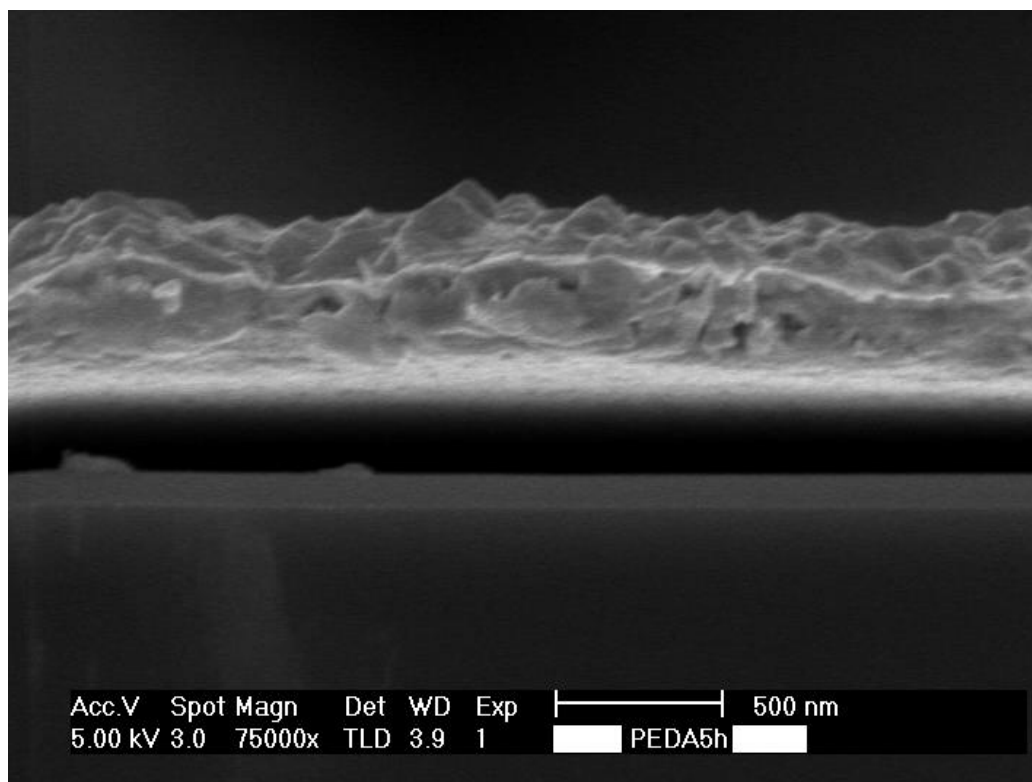
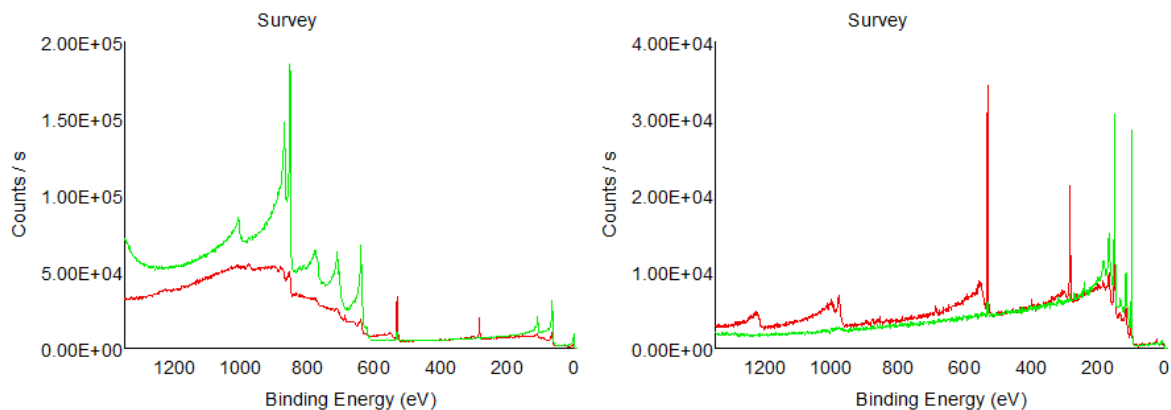


Figure 5.3 - Adhesion issues: a low adhesion may cause the lifting of the metal layer.



Plot 5.11 - Two examples of chemical test made on the surfaces of the two fracture planes.

The experiment were made on 5x5 cm² samples, coated with vapour and liquid SAM (1h for the vapour and 6h for the liquid deposition), with both 1% and 10% NiB chemistry employed. Measurements were made on both annealed and not annealed coupon in order to evaluate the difference this passage made on the adhesion properties of the barrier and metal system. Results on NiB 10 % are shown in table 5.1, the ones of NiB1% are in the table 5.2.

Table 5.1 - Adhesion properties of NiB 10% and 1% on differently processed barrier layers.

Description	No Anneal (J/m ²)	Anneal (J/m ²)	Fracture Location
PEDA 6h +NiB 1%	2.8 ± 0.4	5.5 ± 0.2	SAMs
PEDA vap 1h+NiB 1% 90'	1.2 ± 0.4	3.5 ± 0.8	SAMs
PEDA 6h +NiB1% 90'	3.9 ± 0.5	4.8 ± 0.3	SAMs
PEDA 6h +NiB 10%	5.1 ± 0.9	6.5 ± 1.5	NiB

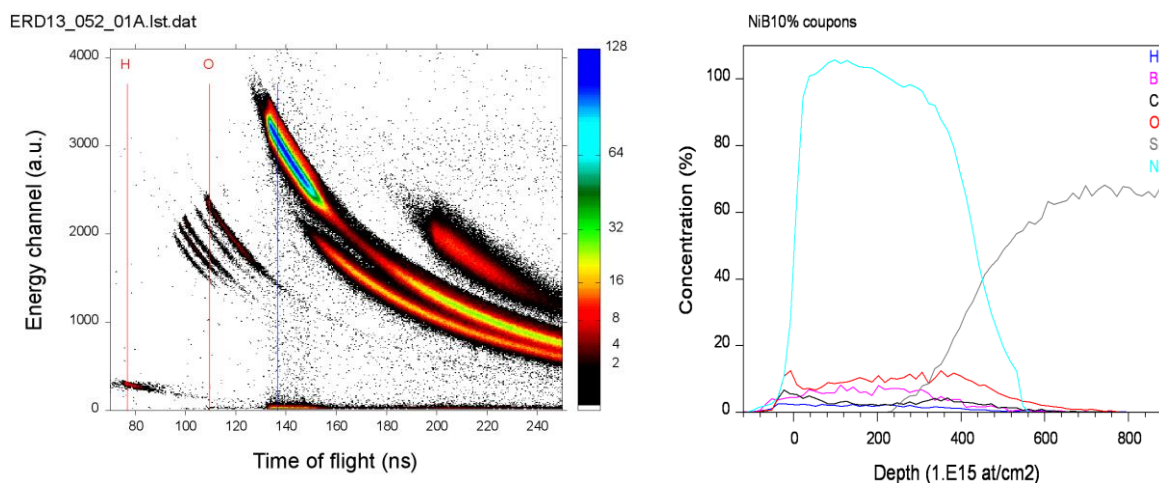
Very good results are achieved in terms of adhesion, with the strength increasing with the annealing of the sample. The value of surface adhesion is high enough to meet the requirements normally needed in the IC industry. The fracture location seems always to be the SAM layer, except for the last case, where the interface seems to have broken at the NiB layer. Here the surface did not appear clean under optical microscopy, but the absence of N peaks on both interfaces, like instead happened in the previous coupons, suggest a rapture of the NiB layer.

5.3.5 Chemical analysis

The two chemistries used for the deposition of the NiB layer, contain a different nominal content of boron in the film: 10% and 1% in atomic percentage. The chemical analysis was employed to evaluate if the actual presence of boron in the film was close to the supposed one. A technique

named *Elastic Recoil Detection* (ERD), a particular ion beam analysis measuring system, was used to evaluate the concentration of the present atomic species at different depths of the stack.

Coupons employed where 3x3 cm² with PEDTA liquid deposited for 4 hours, and both NiB1% and 10% where provided pre- and post-anneal. An example of the data obtained is shown in plot 5.9 while the percentages in the four coupons provided are shown in table 5.2.



Plot 5.12 – (left) spectrum obtained from the ERD measurement; the graph is presented in terms of the time of flight of the detached atoms from the surface versus the energy possessed. A depth graph (right) can be then obtained.

Table 5.2 - Atomic species present in the coupons.

Sample	Spectrum	H	B	C	N	O	Ni
1. NiB10% coupons	ERD13_043_01A	4,5%	3,5%	1,2%	0,9%	6,8%	83,2%
2. NiB10% coupons anneal	ERD13_043_02A		4,4%	0,0%	0,8%	3,6%	91,1%
3. NiB1% coupons	ERD13_043_03A	5,1%	1,9%	2,7%	1,5%	11,1%	77,7%
4. NiB1% coupons anneal	ERD13_043_04A		2,7%	0,2%	0,4%	4,3%	92,4%

As it can be seen from the tables, boron concentration is different when the 1% and 10% NiB chemistry is used. The percentages of boron are anyway quite different from the expected ones. The 1% NiB, with a quantity of 1.9% has a quite low boron quantity that is still higher than the nominal one. This quantity increased after anneal, due to the high temperatures reached when other chemical species are released. The NiB 10%, present a quantity that is a third of the expected one before anneal and that goes up to 4.4% after the annealing step. Carbon and hydrogen are nearly totally released after anneal and also the oxygen quantity presents a strong decrease, giving rise to a good layer. The boron quantity is a factor directly influencing the conductivity of the layer: since the different in the content is not as high as the nominal value may suggest, it can be understood why the resistivity measured between the NiB 10% and 1% is not so high either.

5.4 NiB in Trenches

5.4.1 Materials and Methods

The next step of the development of an alternative metal as interconnect is the actual depositing and testing of the metal inside the conductive lines. Full wafer where provided, with a single die patterned in many copies on it. The pattern of the die can be seen in figure 5.4.

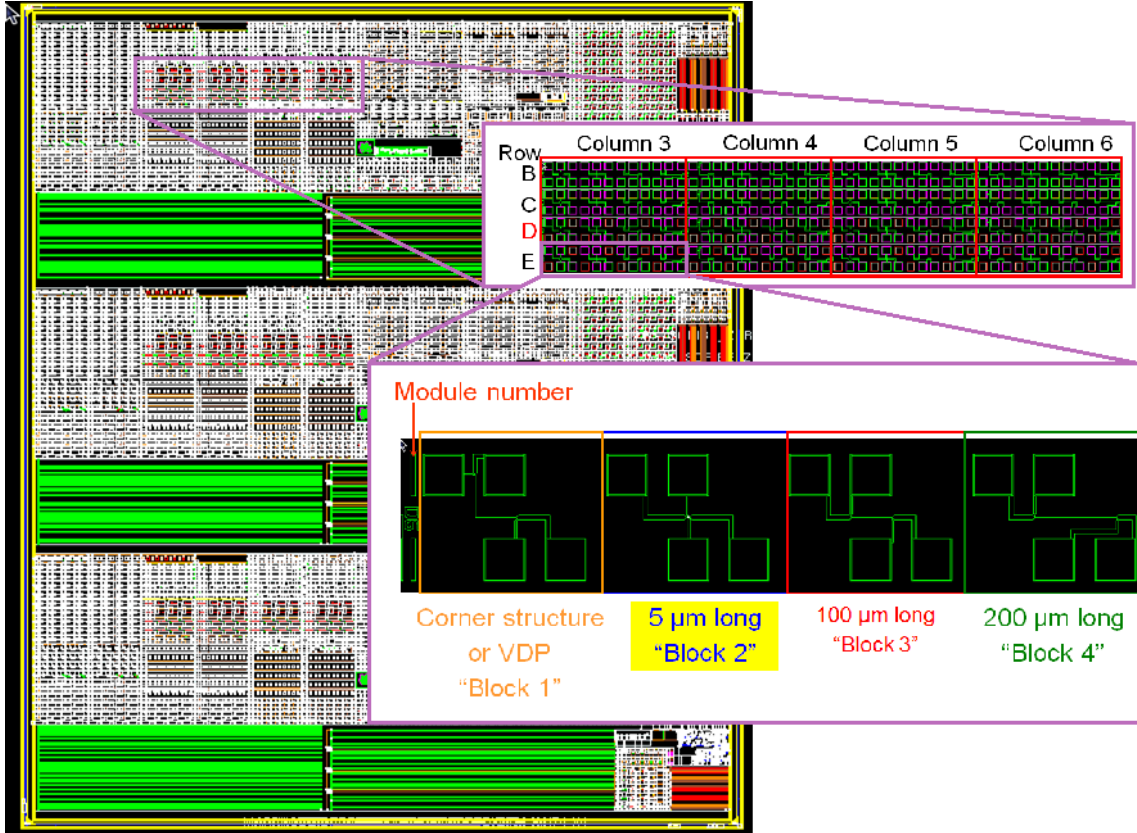


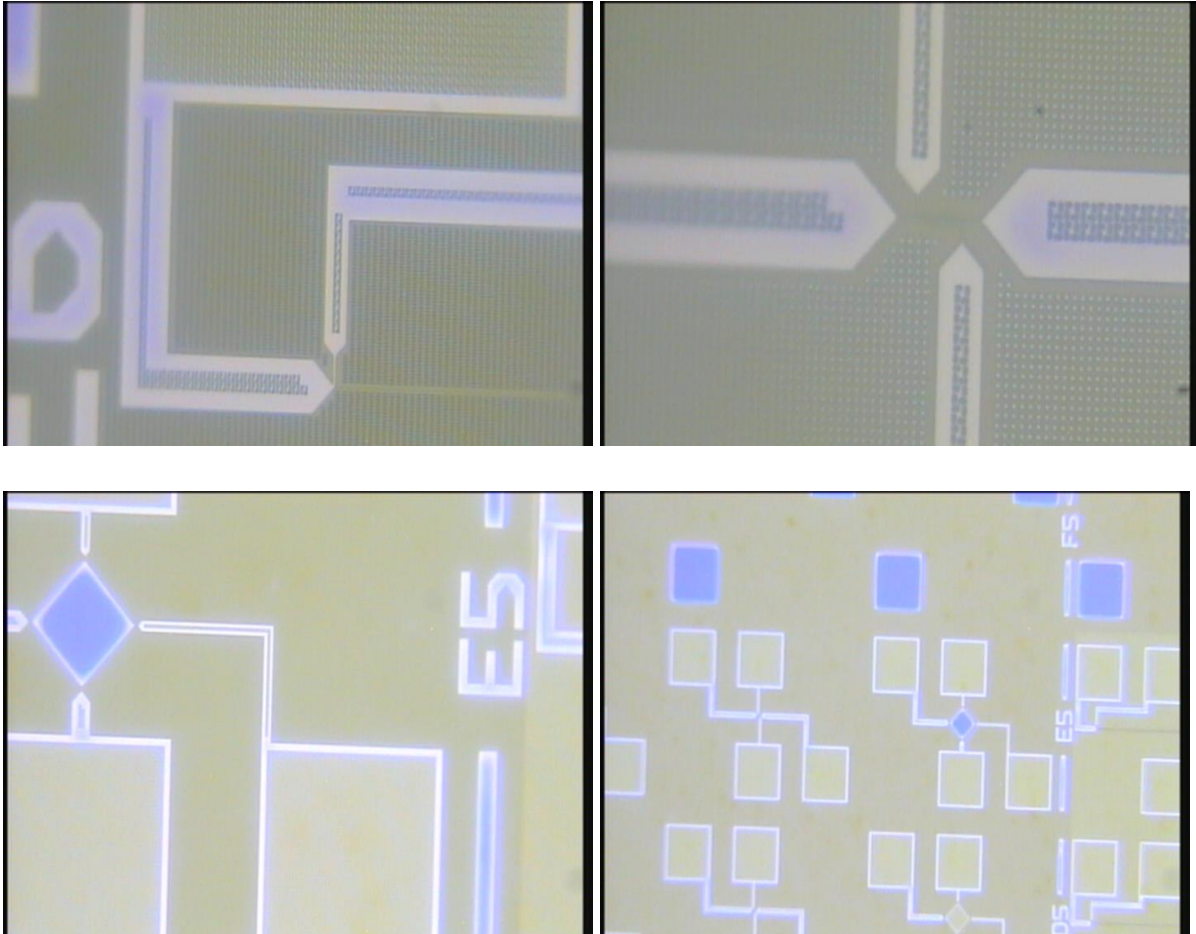
Figure 5.4 - Representation of the die: every die is divided in 3 sub dies (A0, A1, A2). Each column and row contains different features. In the present work the 5 μm long line was measured, with nominal depth of 60 nm. Width ranged from 10 nm to 825 nm.

In every sub-die a series of patterned structure where present. The 5 μm long “Block 2” line was used for the experiments, with the depth of 60 nm and the width that varied from 10 to 825 nm. Test were conducted on coupons 2.9x2.6 cm^2 in order to match the dimension of the pad used for the Chemical-Mechanical Polishing (CMP) step (figure 5.5).



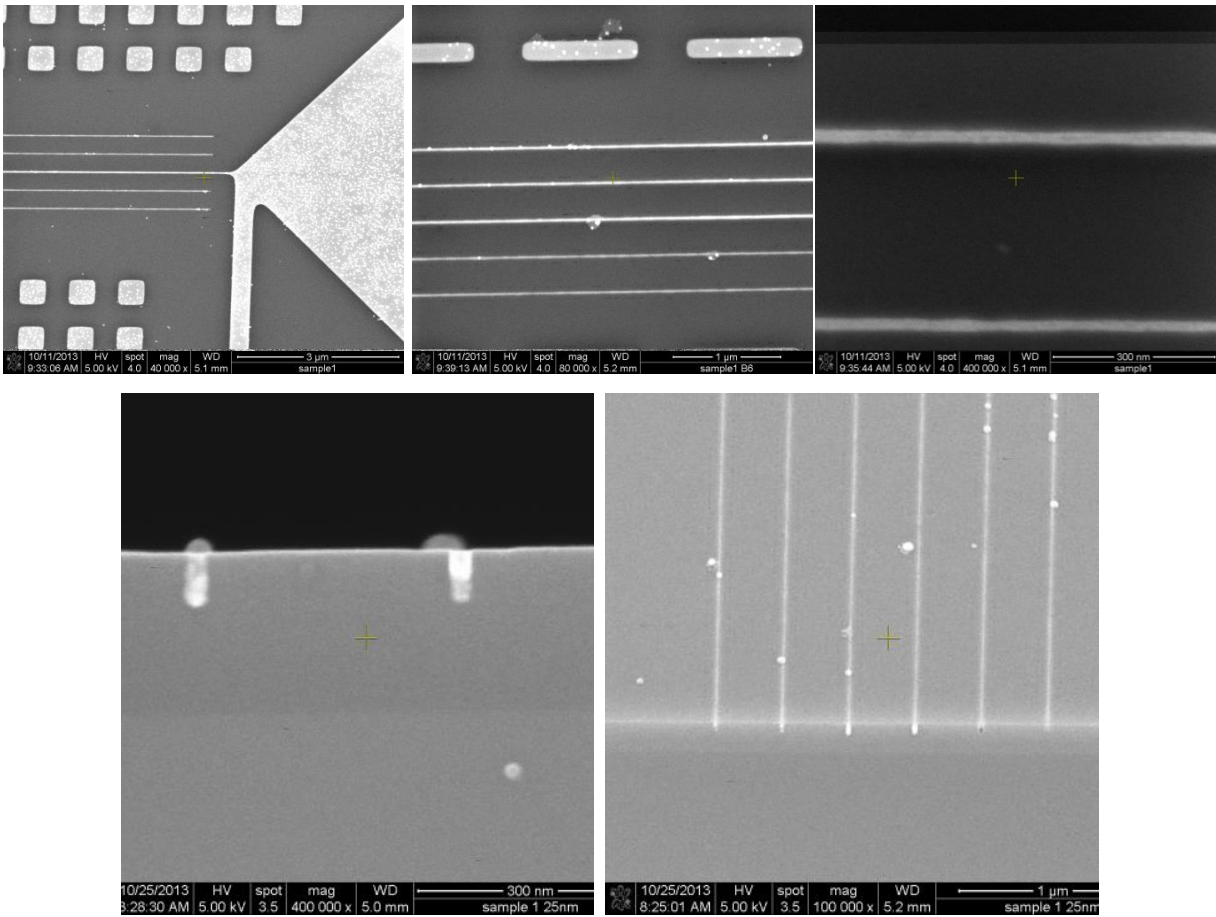
Figure 5.5 - Particular of the CMP Mecapol tool.

Both SAMs were initially from a liquid phase for 2 and 5 hours, since these timings have been proven to be useful in the previous experiments. PEDA and DETA were then used, coupled with both NiB 1% and 10%. The deposition was carried out for several minutes, normally around 45', to give the possibility of a good metal film to deposit. A big deposit favours a more precise CMP step. Once the deposition was made, the coupons were measured once, in order to evaluate the line resistance pre-anneal, and then after anneal. The anneal step could not be made after anneal due to delaminating events during the successive CMP progress. This was probably caused by a variation in the chemical structure of the NiB that favoured a granular structure; CMP was then made always pre-anneal. The CMP could be controlled easily through optical microscope during the polishing. To avoid the transmission of high stresses on the metal through the rotating pad the rotating speed was kept low and the pressure of the pad was set on 2 psi; no cracking or delamination of the metal was seen in this case. The slurry employed was based on the Acuplane 4100, normally employed for the polishing of nickel alloys, it was very useful for the project due to its selectivity, during the polishing, of the metal and not of the silica. The solution was composed by 2 L of water, 1 L of Acuplane 4100 with 15 ml of H₂O₂ needed to activate the chemical reactions happening during the polishing.



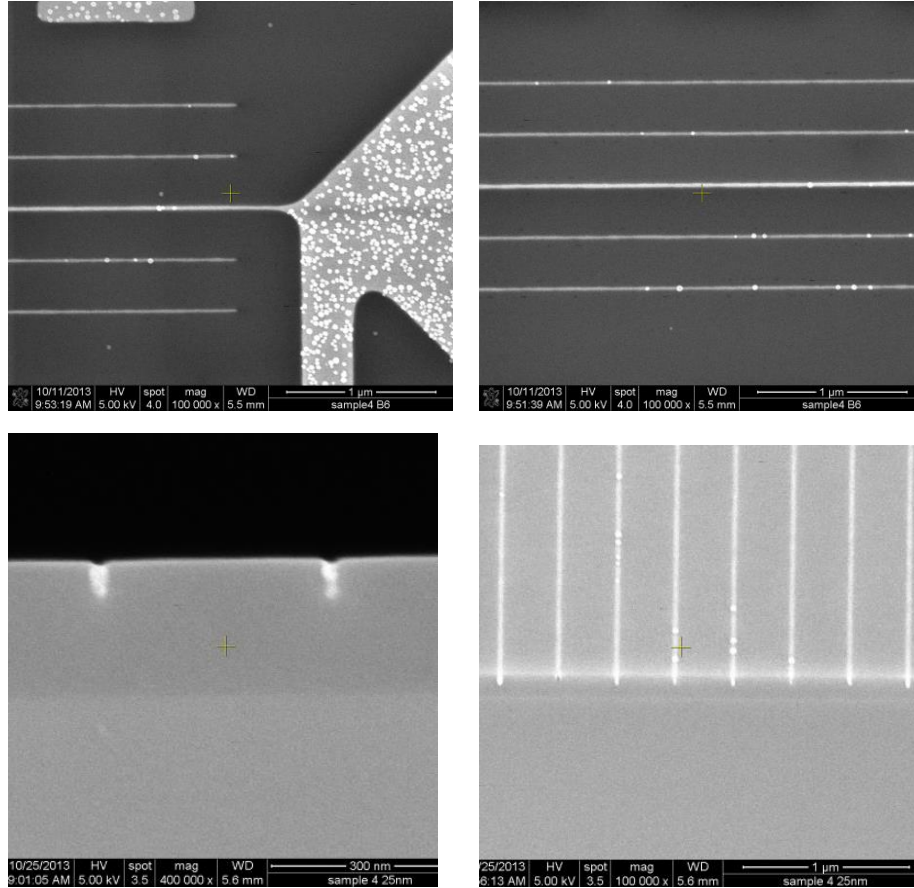
Figures 5.6 - Particulars of the patterned coupons after CMP; the square represent the contacts necessary for the electric measurement of the resistance of the lines.

The processed coupons were seen on the SEM microscope in order to have a clearer value of the contacts and the lines. The evaluation through the SEM was especially useful to evaluate continuity in the line. Figure 5.7 and 5.8 show two of the most successful cases.



Figures 5.7 – Details of the patterned sample PEDA liq 2h with NiB 10%.

The particulate present in the images is formed by the nanoparticles contained in the slurry which are necessary for the mechanical etching of the metal. Their presence anyway did not affect the electrical measurements of resistivity.



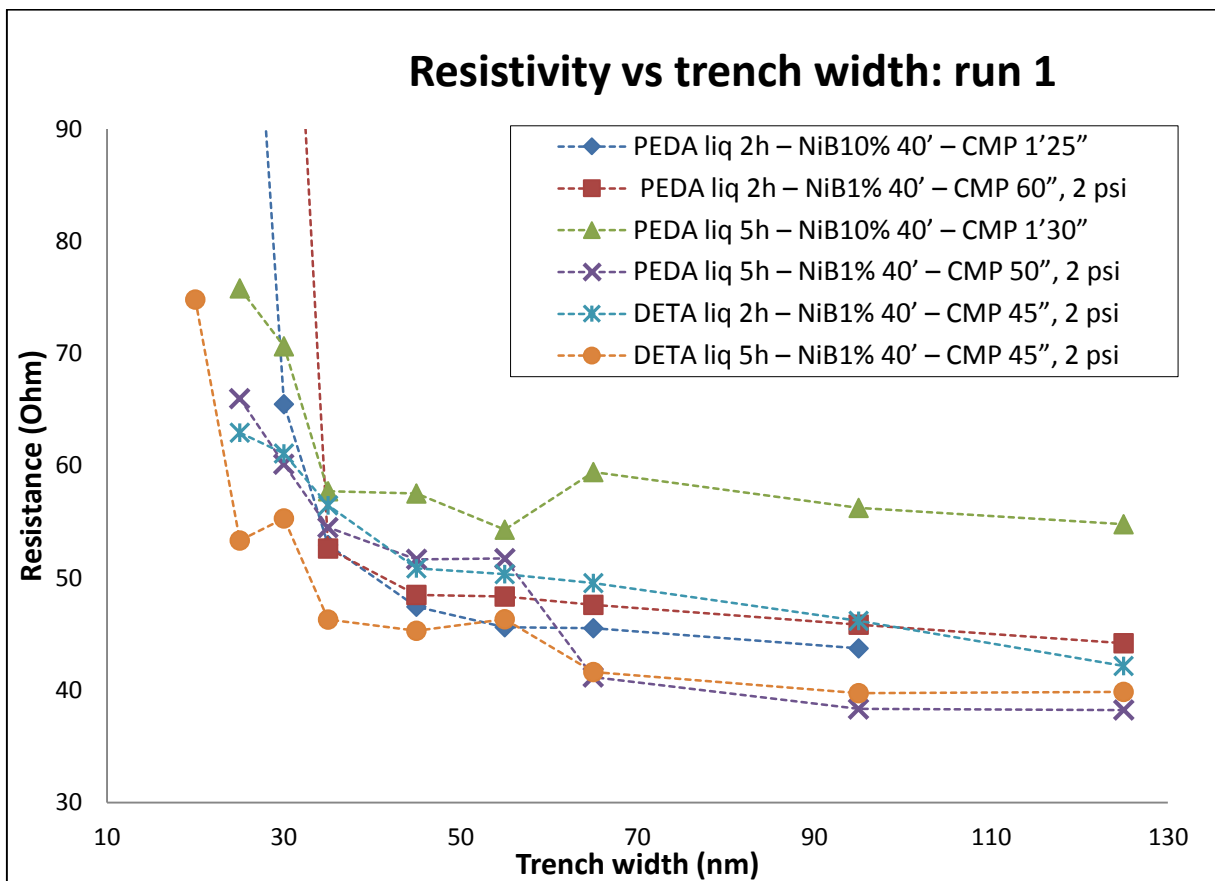
Figures 5.8 - Details of the coupon PEDA liq 5h with NiB 10%.

The well processed coupon where then used to measure the electrical resistivity of the lines.

5.4.2 Results Presentation and Discussion

5.4.2.1 First run

The resistivity data of the first run of patterned coupons are presented in the next plot. Not all the sample have passed successfully the CMP and measuring test could not be performed. The best results were achieved with the liquid DETA 2h, with NiB 1% deposition. The post-anneal data has been presented since it is more representative and eventually comparable.



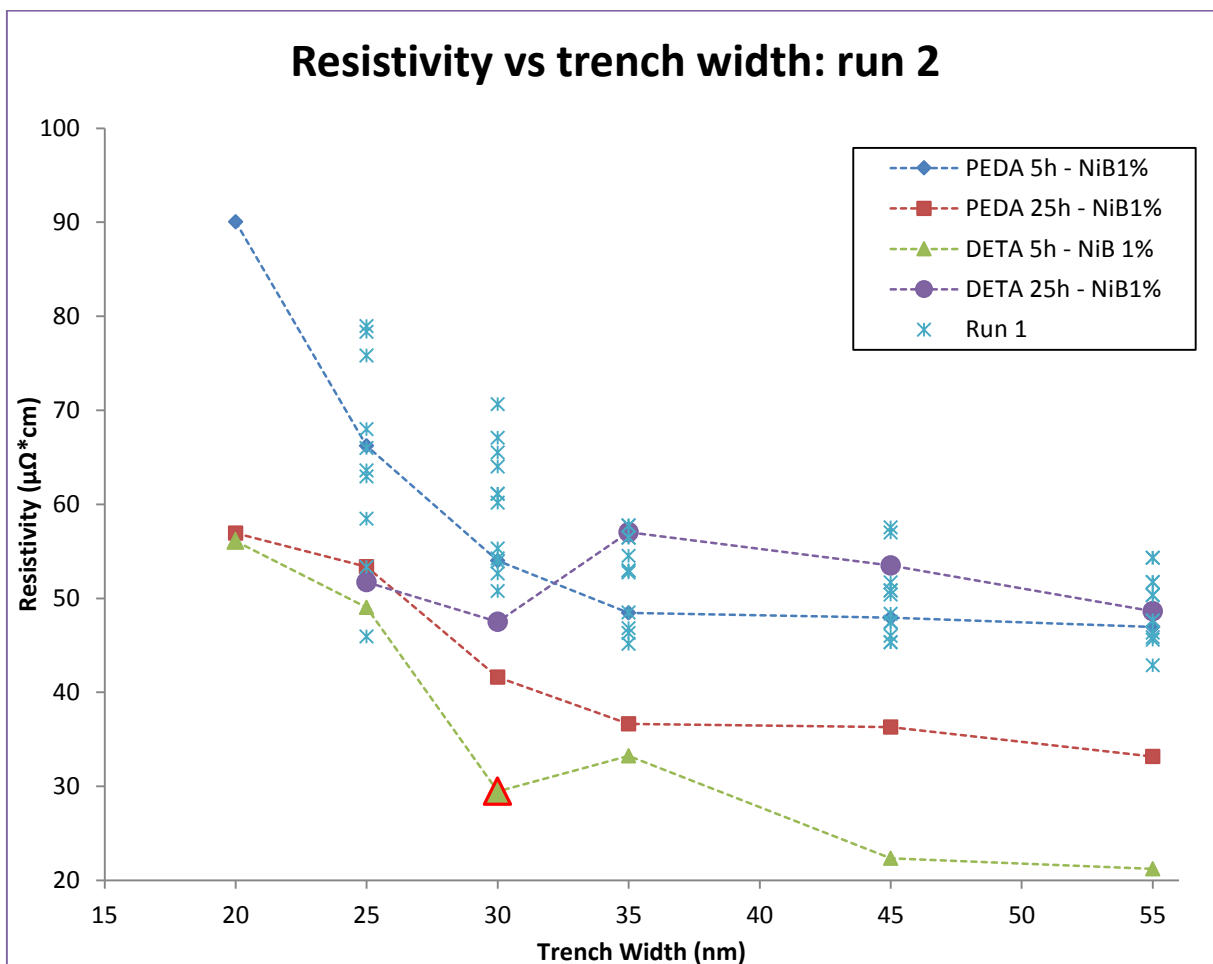
Plot 5.13 - Resistivity data of the first run on patterned coupons.

The graph indicates the good values of resistivity achieved with the DETA 5h liquid deposited with NiB 1%; in general, at the lower measurable line width (20-35 nm), the 1% NiB shows the best results. Therefore, the next experiments insisted on the coupling of the SAM with NiB 1%.

5.4.2.2 Second run

During the next deposition, a higher density of the DETA or PEDAs layer was the objective; therefore, a longer deposition time has been tested, along with the previously tried 5h

deposition. In the meantime a better understanding of the CMP step was achieved: avoiding dishing of the line greatly improved the filling and thus the resistivity of the lines.

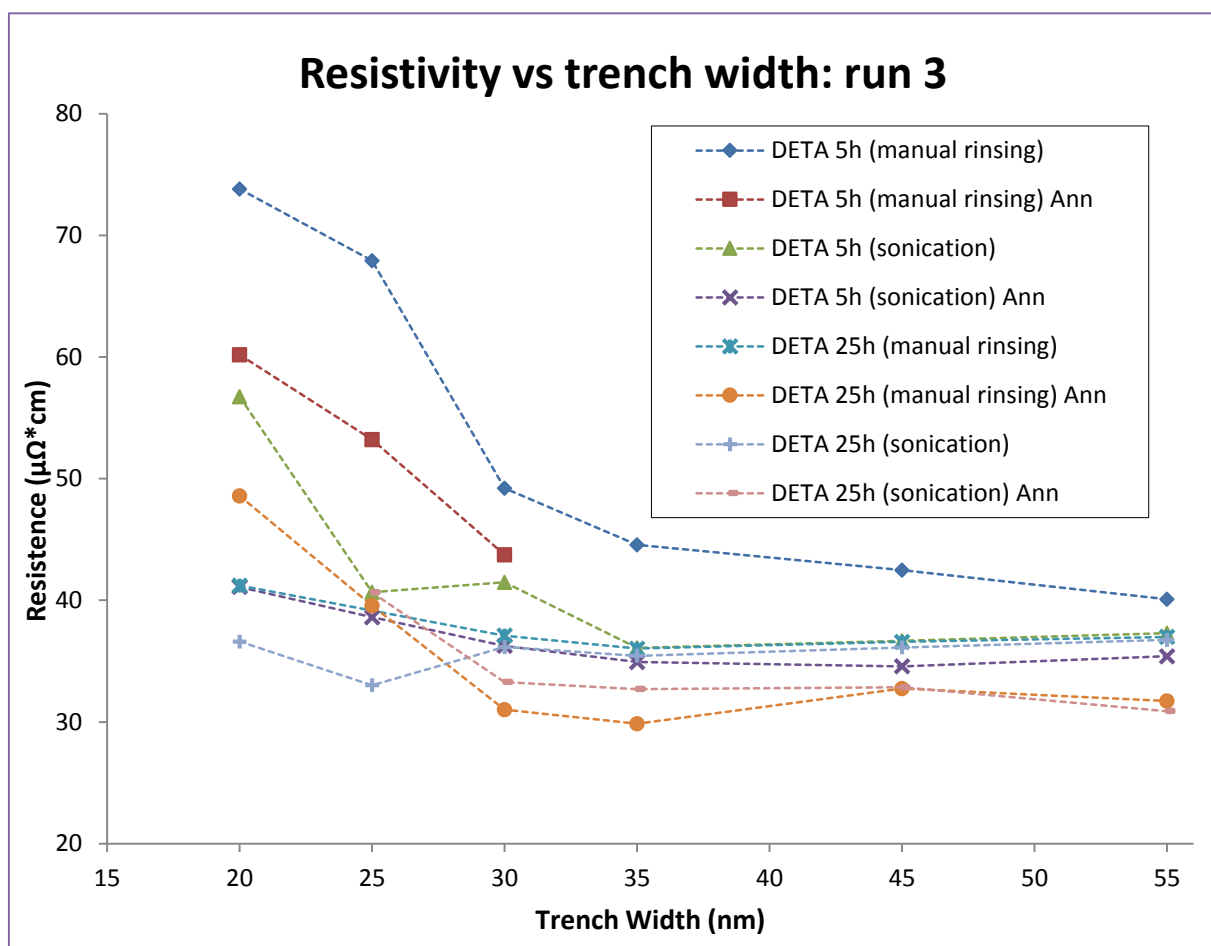


Plot 5.14 - Resistivity data of the second run of patterned coupons (the first one has been kept to permit a good confront).

The increased deposition time of the SAM up to 25 h did not give the expected results. Anyway a better production of the coupons managed to lower the resistivity down to a very promising 29.4 $\mu\Omega\cdot\text{cm}$ for liquid DETA 5h deposited.

5.4.2.3 Third run

Even if the dimension of the trenches was provided, next goal was an effective measurement of the dimension of the metal deposit, in order to get a more precise evaluation of the resistivity. To obtain images with such a definition the only option was to use the Transmission Electron Microscope (TEM). A new set of coupon was then produced. Since the DETA SAM seemed the most promising, PEDTA was not employed. In the meantime, annealing of the organic layer and sonication after deposition was also used as a last tentative for the improvement of the deposition. The value of resistivity versus the line width of the coupon processed is presented in plot 5.12.



Plot 5.15 - Run 3 of patterned coupons.

The results are in line with the previous ones obtained and no particular improvement is shown by the annealing, while the most conductive line for the lower trench widths is possessed by the 25 hour processed DETA coupon with post-SAM deposition sonication.

5.4.3 TEM Analysis

5.4.3.1 Line shape

Of all the coupons processed, four were examined with the TEM to evaluate the area; images of these samples are shown. These are:

- #4: 20nm lines DETA liq 5h sonication ANN Pd 5' + NiB 30' +CMP 30'' 2psi+anneal
- #6: 30nm lines DETA liq 25h manual rinse Pd 5' + NiB1% 40' + CMP 48'' 2psi+anneal
- #7: 20nm lines DETA liq 25h sonication No ANN Pd 5' + NiB 40'+CMP 45'' 2psi+anneal
- #8: 25nm lines DETA liq 25h sonication ANN Pd 5' + NiB 40'-CMP 45''2psi+anneal

The system used is the Tecnai F30, operating at 300kV.

The coupons were capped with low temperature CVD silicon oxide before the microscopy procedure. It is clear from the SAM top image (figure that five parallel lines are present but only the central one is actually the one making current flow possible; the other four represent dummy lines that may give information on the deposition characteristics.

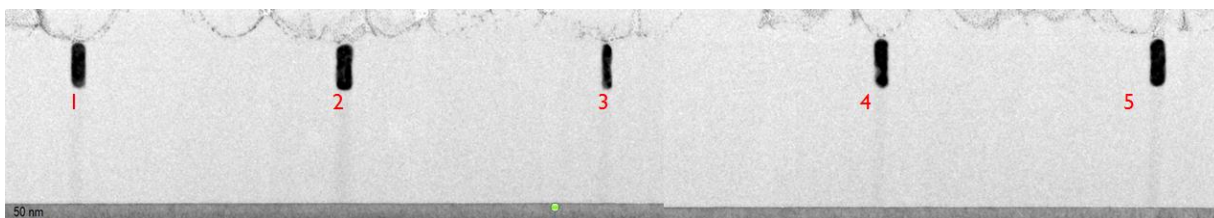


Figure 5.9 – TEM image of the section of the parallel in the patterned coupons; only the middle one is able to conduct, the other four are dummies.

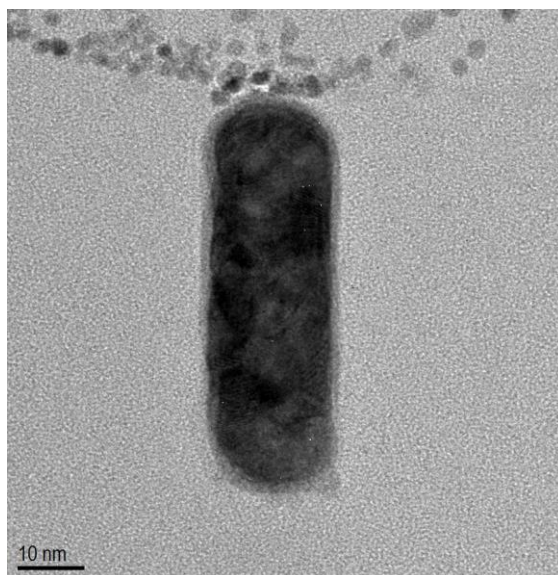


Figure 5.10 - TEM section of line #1.

From the particular image of the line we can see the exact geometry of it: the line does not present a polygonal shape, both top and (expectedly) bottom show a round surface. The bulk of the metal is formed by different shades: the metal is polycrystalline and the orientation of is able to change the intensity of the colour. The grey layer around the lines is probably due to the roughness at the interface; the presence of it also on top of the substrate indicates that it is not the SAM layer. The measurement technique HAADF-STEM was used, together with the

DF-STEM. The first has brightness proportional to the square of the atomic number $\langle Z^2 \rangle$ of the element while in the second it is related to the density and crystallinity (especially evaluating defects, grains and voids).

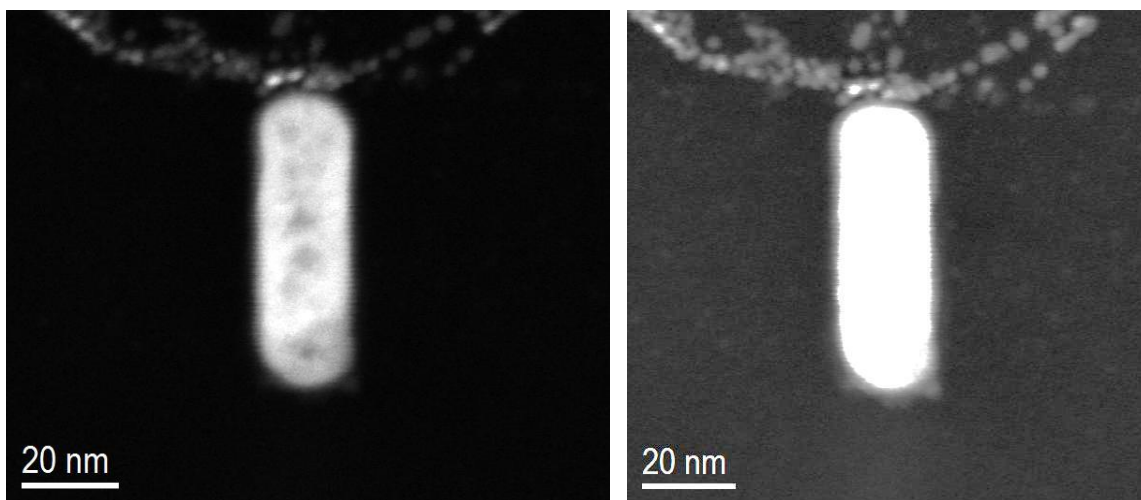
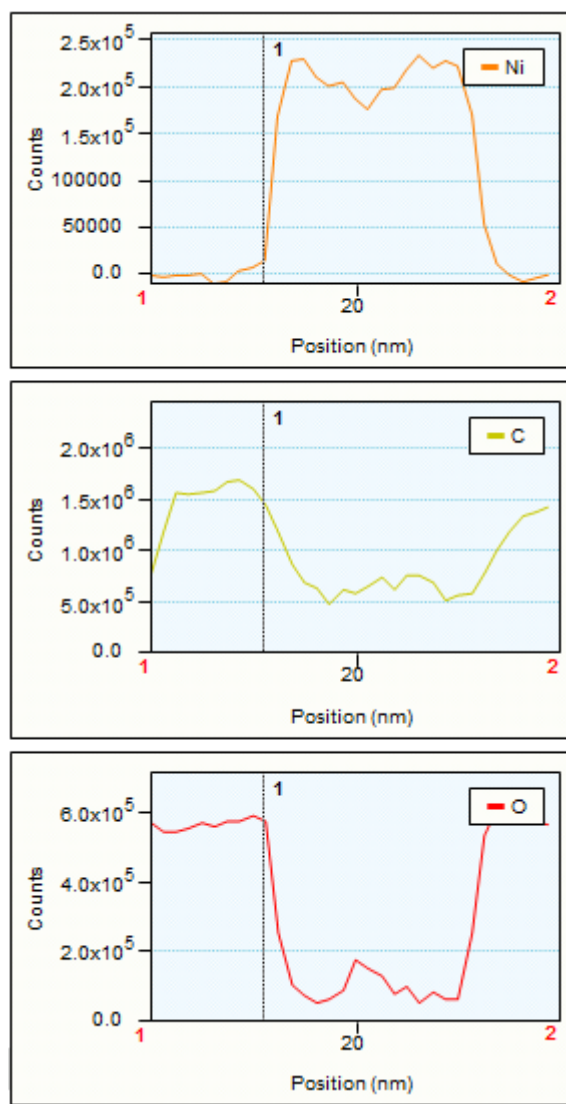


Figure 5.11 - (left) HAADF-STEM of the previously pictured section and (right) DF-STEM of it.

The Pd cannot be distinguished at the metal/dioxide interface; some voids are present at the center of the line but the deposition is overall quite good. With the TEM, using an Energy Dispersive Spectroscopy (EDS), we are also able to see which elements are present in our images and count them. This count is shown in plot 5.13, and the count is made along a line

cutting the line parallel to the surface. Point 1 and 2 represent the intersection between this line and the NiB/SiO₂ interface.



Plot 5.16 - Element count made by HAADF-STEM

While the nickel signal is perfectly inserted inside the trench line and no signal is measured outside of it, the carbon signal is present all over the line. The signal is maybe caused by the

plasma etch step necessary to clean the sample before the measuring step. An intensity peak is not evident at the interface where the SAM layer should be but this is might be due to a not high enough lateral resolution or the destruction of the SAM during the plasma etching step.

5.4.3.2 Line resistivity

The sections of the four conductive lines are shown in figure 5.10: we will now use this additional information to evaluate the resistivity of the samples.

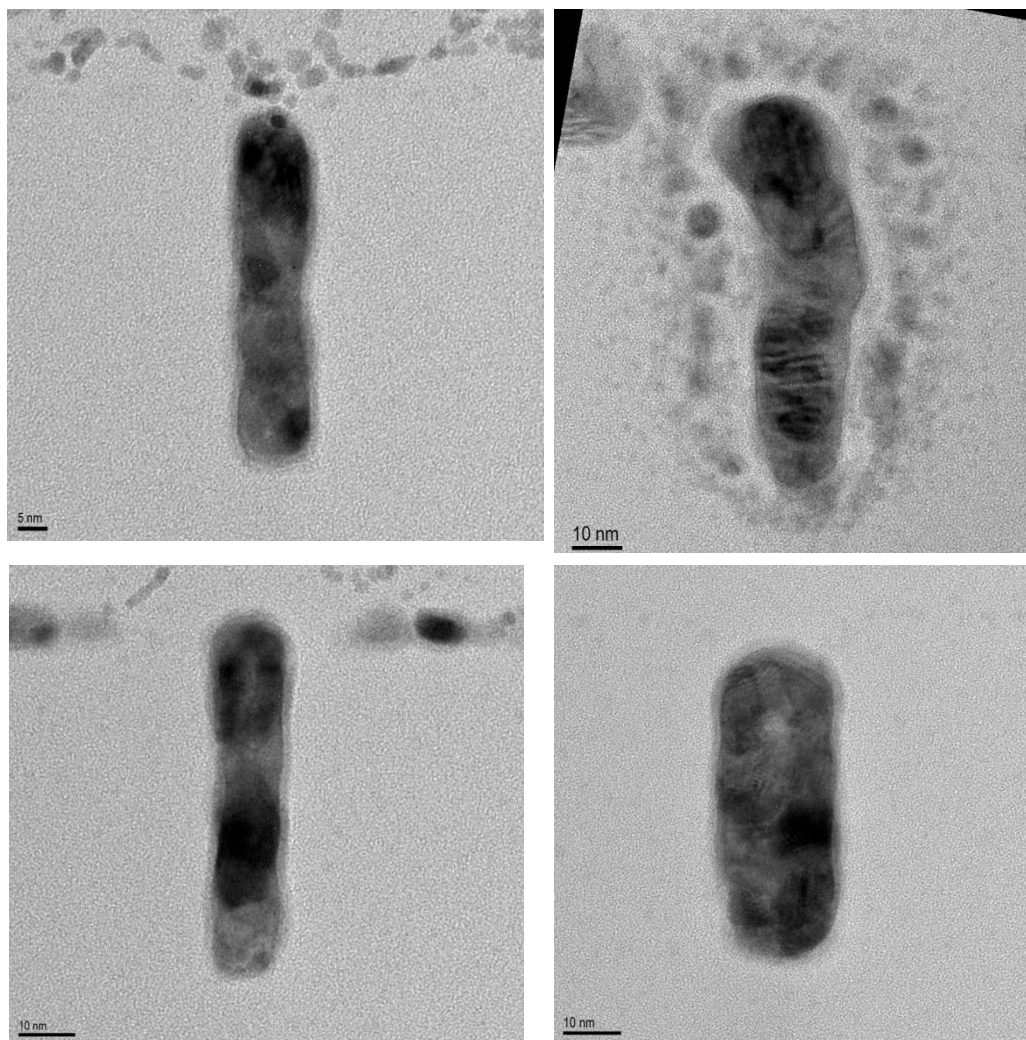
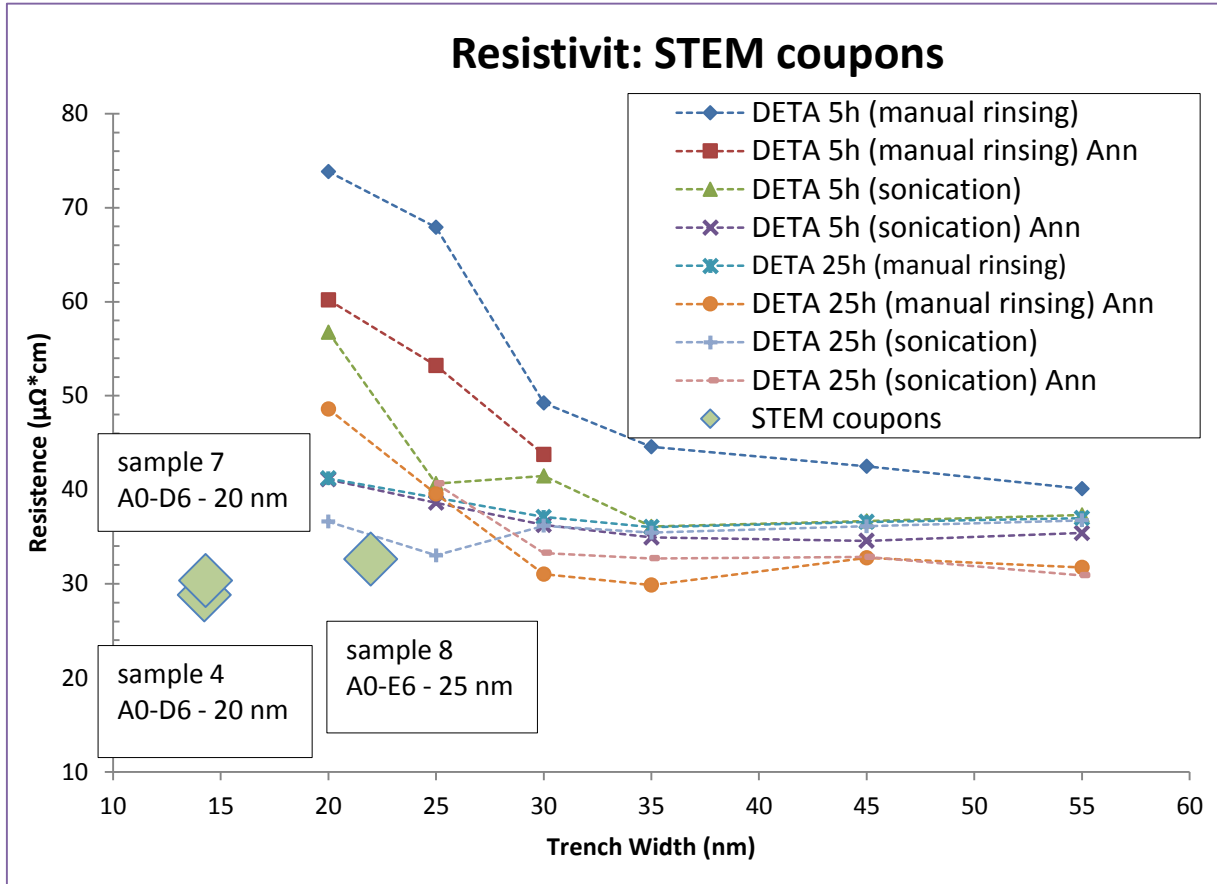


Figure 5.12 - (from upper left, clockwise) Section of the four conductive lines. The explosion in the second line is evident from the image.

It can be noticed how, in coupon #6 (upper right in figure 5.12) the current, passing through the line, to high for it to support, caused the explosion of the metal outside the line, de facto making it unusable from now on. In this case the change in resistivity was not evaluated. The dimensions were measured during the STEM use: the height of the line did not vary to much with respect to the expected 60 nm dimension (for all coupons variation <5%), while the width

did greatly. The use of the actual line width to plot the resistivity data, like previously made, changed drastically the importance of such data, like it can be seen from plot 5.14..



Plot 5.17 - Resistivity data, together with the samples STEM processed.

To give a better and more complete idea to the reader of the importance of these data a plot has been prepared and is shown in which different resistivity data is present: the newly calculated resistivity of coupon #4, #7 and #8 (with nominal line width of respectively 20, 20

and 25 nm), the old data on NiB resistivity made during the realization of this project, plus the data gently provided by imec on copper and tungsten. The result is shown in plot 5.15.

The plot gives very interesting results: NiB is able to conduct with results that are in line, or even better than tungsten, deposited through vapour techniques or through electrodeposition. Copper instead has still much lower resistivity with respect to NiB, but the gap between the metal and the alloy is not so high as expected before, once the actual dimension of the line is evaluated. It should be noticed that anyway, data on Cu is referred to a technique that involves copper sputtering and electrodeposition growth of it on the seed layer.

Table 5.3 - Line dimension and Resistivity as evaluated from TEM.

Specific	Sample #4	Sample #7	Sample #8
Nominal Width (nm)	20	20	25
Actual Line Width (nm)	14.23	14.30	21.97
Actual Line Height (nm)	59.1	63.9	54.8
Resistivity ($\mu\Omega \cdot \text{cm}$)	28.809	30.36	32.63

The process is greatly employed because of its capability to fill without voids the trenches and good electromechanical properties. The NiB produced in such project shows higher resistivity but at production costs infinitely inferior: a simple wet deposition was performed giving good results, without the need of costly low-pressure instrumentation and in a single deposition step.

The most important objective, reached in this section, is that the deposition of NiB through ELD is not only possible but it can be easily achieved in lines as small as 12 nm, with remarkable conductivity properties.

Chapter 6: Conclusions and **Future Perspectives**

6.1 Conclusions

As the shrinking of the characteristic dimensions of nodes and interconnections continues in the IC industry it is by now clear that the Ta/TaN layer will not be able guarantee good step coverage and anti-diffusion properties for thicknesses below 5 nm.

Self-assembled monolayer, embedded in a SiO₂/NiB stack, appears as a strong candidate for the substitution of obsolete barrier layers, due to their structural and chemical properties allowing them to have good barrier properties and provide a suitable substrate for subsequent depositions. To realize such sandwiched structure, an “all-wet” process has been under examination in this work.

The first part of the project was focused on the screening of two different SAM precursor molecules, with varying deposition process specifics. Along with the commonly used liquid deposition, a vapour deposition was also explored in a first attempt for the scaling-up of the current “all-wet” process to full wafer. The SAMs layers were characterized through the evaluation of different properties in order to achieve an overall better deposition in terms of:

- structural density and thicknesses;
- formation of a monolayer;
- surface amino- groups.

A Langmuir-type growth was observed for both DETA and PEDA deposited from solution. Low thicknesses (<2 nm) were reached with good densities (especially for liquid PEDA) just after

2 hours deposition, with the packing of the molecules increasing with longer deposition times. But if for PEDA, the maximum amount of nitrogen surface atoms (directly related to the amount of amino-groups present) reaches 3.5% after 5 hours of liquid deposition, the DETA SAM, despite the higher amount of amino groups possessed by the precursor (3, against the 2 of PEDA), shows a lower quantity of surface N atoms: 2.64%. On the contrary vapour DETA manages to reach values as high as 5.31% for a 30' deposit, confirming promising outlook. PEDA instead does not show good properties for a vapour deposition. Results are confirmed by XPS, where the amount of Pd-catalyser deposited over the organic layer, whose quantity and homogeneity directly affects the metal deposit properties, is higher for the vapour DETA ($91.4 \cdot 10^{13}$), in the case of liquid deposition, and the 5 hours liquid PEDA ($36 \cdot 10^{13}$). PEDA confirms to be a highly packed organic layer, thanks to the bulky benzene ring present in the backbone and a very good substrate for Pd liquid uptake. Vapour DETA appears promising but a better understanding of vapour deposition should be achieved to perfectly understand the organic layer formation mechanism and the deposit quality.

After analysing the organic layer deposition step and the palladium uptake on different substrates, the metal electroless deposition was taken into account. The PdCl₂-based solution and the two NiB chemistry employed in the research were provided by LAM Research®. A different amount of boron is contained in the two deposits due to different bath composition, with nominal quantity of 10% and 1%. Since the two chemistries are not commercial, no precise knowledge of the composition of them is perfectly known. Resistivity was calculated for thin film deposition of both NiB 1% and 10% on variously deposited organic layer. The annealing of the SAM did not bring any change in the deposit quality and was therefore abandoned to avoid the risk of contamination. The metal annealing, providing the possibility of crystalline reorganization, confirmed a drop of one order of magnitude of the thin film resistivity. NiB 1% gave the best result especially on 5 hours long processed liquid PEDA and DETA (respectively $\rho_{\min}=30 \div 40 \mu\Omega \cdot \text{cm}$ for film thicknesses around 20 nm and $\rho_{\min}=35 \div 45 \mu\Omega \cdot \text{cm}$ for thicknesses around 15nm) and on vapour PEDA $\rho_{\min}=21 \div 23 \mu\Omega \cdot \text{cm}$ for 20 nm and

65÷70 $\mu\Omega\cdot\text{cm}$ for 10 nm). Other measurements confirmed a not expected faster growth rate of 1% with respect to the 10% (the higher quantity of reducing agent in NiB 10% should be responsible for a faster deposition of the metal). Also, adhesion confirmed to be high enough to exceed the requirements for successive processing in the IC industry with values up to 6.5 J/m^2 . ERD confirmed a different composition of the bath from the deposit, with NiB 1% film containing slightly more than expected B (2,7% after anneal) and NiB 10% containing much less (4,4%) than the nominal 10%.

Since better knowledge is possessed on liquid SAM deposition and, at the same time, vapour deposition is known not to have good homogeneity over full wafer and good step coverage still have to be confirmed, only liquid deposited SAM was used on patterned coupons. Line resistivity was measured employing both chemistry, even if NiB 10% was promptly abandoned due to the lower conductive properties compared to the NiB 1%. NiB was deposited up to circa 300 nm in order to completely fill the trenches and features present in the coupons and easing the successive CMP step. After a better knowledge of this latter step was achieved, through experience and through the use of optical microscopy and SEM, the best result where reached on liquid 5h DETA deposited, with a resistivity of 29.4 $\mu\Omega\cdot\text{cm}$ on a 30 nm wide line. Longer deposition, coupled with sonication cleaning did not give a remarkable decrease in resistivity, but, of this last run, the four better resulting coupons where given for TEM analysis. The TEM confirmed the barrier ability of the organic layer between NiB and SiO_2 , with good filling of the line. A rough interface and the presence of different grains are confirmed by the high resolution images. Also, it is evident that shape and dimensions of the line is not the one expected: the section possesses a round top and bottom and width appears to be much smaller (height is more or less the same). A new evaluation of the section, coupled with the modification of the already calculated resistivity, gave the remarkable result of 28 $\mu\Omega\cdot\text{cm}$ for a line width of 14 nm. The gap between copper and NiB appear still quite large but the deposition shows important promising characteristics. A part from a resistivity in line, or even lower, with all the other metals normally employed in IC industry (like W), the process has the

great advantage of employing very cheap deposition techniques. Besides, no, or limited (in the case of vapour SAM deposition), use of high vacuum processes, like instead traditional processes like sputtering or CVD/PVD, is required. Therefore ELD NiB on SAM can be considered a good alternative to the currently employed PVD/sputtering Ta/TaN barrier.

6.2 Future Perspectives

It would be impossible in just a few lines to address the infinite possible perspectives of integrated circuits in ULSI technology. Thus, only the possibilities of SAM organic layers coupled with ELD metals will be treated. To complete the current project a better study on the metal annealing step should be taken: the fact that the CMP step works easily pre-anneal but not after it implies a change in the chemical and physical structure of it. A change in the phases and/or grain dimension could be the cause, but an accurate XRD test is probably needed to actually demonstrate it. A better understanding of the bath could give insight on the composition and could explain why the composition of the film are different from the nominal one and why the growth rates show inverted values (faster for NiB 1% which contains a lower quantity of reduction agent). Finally a better filling of the line (voids may be caused by the rearrangement of the increasing grain size) should be achieved in order to get lower resistivity values.

Considering a more long-term research, a better understanding of the vapour deposition mechanism of amino-silanes would bring essential advancements in the scaling up process from coupons to full-wafer. This is an essential step necessary for the process to be developed for an industrial application. Other terminating group could also be studied and employed: i.e. pyridines, azido-compounds, metalphthalocyanines. Maybe coupled with alternative catalysers like copper, tin or other noble metal nanoparticles. It would be interesting to evaluate the

coupling of SAM with other ELD metals. Deposition of pure Ni instead of an alloy would surely bring better conduction properties. Different metals could be deposited, like cobalt (Co), transitional metals, like Rhodium (Rh) or Ruthenium (Ru) or even silver (Ag).

References

1. Feynman, R. P. Plenty of room at the bottom. in *Talk to Am. Phys. Soc.* 1–7 (1959).
2. Taniguchi, N. On the Basic Concept of “Nano-Technology.” in *Proc. Int. Conf. Prod. Eng.* (1974).
3. Ramsden, J. *Essentials of nanotechnology.* 126 (2009).
4. Foresight Institute - About Nanotechnology. at <https://www.foresight.org/nano/>
5. Haselman, M. & Hauck, S. The future of integrated circuits: A survey of nanoelectronics. *Proc. IEEE* 1–57 (2010).
6. International Technology Roadmap for Semiconductors (2005 Edition). (2005). at <http://scholar.google.com/scholar?hl=en&btnG=Search&q=intitle:INTERNATIONAL+TECHNOLOGY+ROADMAP+FOR+semiconductors+2005+edition#1>
7. Rodgers, P. Nanoelectronics: Single file. *Nat. Nanotechnol.* (2006). doi:10.1038/nnano.2006.5
8. Tseng, A. A., Cheng, K., Chen, C. D. & Ma, K. J. IEEE Transaction on Electronics Packaging Manufacturing. *IEEE* (2003).
9. George, S. M., Ott, A. W. & Klaus, J. W. Surface Chemistry for Atomic Layer Growth. *J. Phys. Chem.* **100**, 31 (1996).
10. George, S. M., Yoon, B. & Dameron, A. A. Surface Chemistry for Molecular Layer Deposition of Organic and Hybrid Organic-Inorganic Polymers. *Acc. Chem. Res.* **42**, 498 (2008).
11. Gin, A., Movaghar, B., Razeghi, M. & Brow, G. J. Infrared detection from GaInAs/InP nanopillar arrays. *Nanotechnol.* **16** (2005).
12. *IBM100 - Copper Interconnects: The Evolution of Microprocessors.* (IBM Corporation, 2012).

13. Andricacos, P. C. Copper on-chip interconnections, a breakthrough in electrodeposition to make better chips. *Electrochem. Soc. Interface* 32–37 (1999).
14. Campbell, S. *The science and engineering of microelectronic fabrication*. 2nd Ed. Oxford university Press (2001).
15. Andricacos, P. C., Uzoh, C., Dukovic, J. O., Horkans, J. & Deligianni, H. Damascene copper electroplating for chip interconnections. *IBM J. Res. Dev.* **42**, 567–574 (1998).
16. Pallinti, J. & Lakshminarayanan, S. An overview of stress free polishing of Cu with ultra low-k ($k < 2.0$) films. *Interconnect Technol. Conf.* 83–85 (2003).
17. Pratt, A. Overview of the use of copper interconnects in the semiconductor industry. *Adv Energy Ind* (2004).
18. Gupta, T. *Copper interconnect technology*. (2009).
19. Intel's 14nm milkshake: It's better than yours. at <http://www.extremetech.com/computing/171477-intels-14nm-milkshake-its-better-than-yours>
20. Istratov, A., Flink, C., Hieslmair, H., Weber, E. & Heiser, T. Intrinsic Diffusion Coefficient of Interstitial Copper in Silicon. *Phys. Rev. Lett.* **81**, 1243–1246 (1998).
21. Cros, a., Aboelfotoh, M. O. & Tu, K. N. Formation, oxidation, electronic, and electrical properties of copper silicides. *J. Appl. Phys.* **67**, 3328 (1990).
22. McBrayer, J. D., Swanson, R. M. & Sigmon, T. W. Diffusion of Metals in Silicon Dioxide. *J. Electrochem. Soc.* **133**, 1242–1246 (1986).
23. Murarka, S. P. *Copper – Fundamental Mechanisms for Microelectronic Applications*. (1989).
24. Baklanov, M., Ho, P. S. & Zschech, E. *Advanced Interconnects for ULSI Technology*. 579 (2012).
25. Nicolet, M. & Bartur, M. Diffusion barriers in layered contact structures. *J. Vac. Sci. Technol.* **19**, 786–793 (1981).
26. Li, B., Sullivan, T. D., Lee, T. C. & Badami, D. Reliability challenges for copper interconnects. *Microelectron. Reliab.* **44**, 365–380 (2004).

27. Rathore, H., Aganvala, B. & Nguyen, D. A high performance liner for copper damascene interconnects. *Interconnect Technol. Conf. 2001. Proc. IEEE 2001 Int.* 9–11 (2001).
28. Fischer, a C. *et al.* Very high aspect ratio through-silicon vias (TSVs) fabricated using automated magnetic assembly of nickel wires. *J. Micromechanics Microengineering* **22**, 105001 (2012).
29. Kim, H., Kellock, A. J. & Rossnagel, S. M. Growth of cubic-TaN thin films by plasmaenhanced atomic layer deposition. *J. Appl. Phys.* **92**, 7080–7085 (2002).
30. Fayolle, M., Passemard, G. & Louveau, O. Challenges of back end of the line for sub 65 nm generation. *Microelectron. ...* **70**, 255–266 (2003).
31. Wang, K., Horsfall, A., Cuthbertson, A., Bull, S. & O'Neill, A. Comparative study of novel barrier layers in ULSI copper interconnects. *Microelectron. Eng.* **84**, 2486–2490 (2007).
32. Dubin, V. M. Scaling Trends and Advances in Metal Technologies for On-Chip Interconnects. 4 (2003).
33. Li, W. Atomic layer deposition methods for forming a multi-layer adhesion-barrier layer for integrated circuits. *US Pat. 6,955,986* **2**, (2005).
34. Chaudhry, A. Interconnects for nanoscale MOSFET technology: a review. *J. Semicond.* **34**, 066001 (2013).
35. Kioussis, D. *et al.* Optimization of Porous Ultra Low- κ Dielectrics ($\kappa \leq 2.55$) for 28nm Generation. 2–4 (2011).
36. Caro, A. M. *Exploration of SAMs (self - assembled monolayers) in advanced interconnects.* **IMEC-KUL**, (2012).
37. Barlow, S. M. & Raval, R. Complex organic molecules at metal surfaces: bonding, organisation and chirality. *Surf. Sci. Rep.* **50**, 201–341 (2003).
38. Schreiber, F. Structure and growth of self-assembling monolayers. *Prog. Surf. Sci.* **65**, 151–257 (2000).
39. Franklin, B., Brownrigg, W. & Farish, M. Of the Stilling of Waves by means of Oil. Extracted from Sundry Letters between Benjamin Franklin, LL. D. F. R. S. William Brownrigg, M. D. F. R. S. and the Reverend Mr. Farish. *Philos. Trans. R. Soc. London* **64**, 445–460 (1774).

40. Pockels, A. *Nature* **43**, 437 (1891).
41. Pockels, A. *Nature* **46**, 418 (1892).
42. Pockels, A. *Nature* **50**, 223 (1894).
43. Rayleigh, L. *Philosophic Mag.* **48**, 321 (1899).
44. Hardy, W. B. *Proc. R. Soc. London A* **86**, 610 (1912).
45. Langmuir, I. The Faraday Society. *Trans. Faraday Soc.* **17**, (1920).
46. Blodgett, K. B. Films built by depositing successive monomolecular layers on a solid surface. *J. Am. Chem. Soc.* **621**, 1007–1022 (1935).
47. Love, J. C., Estroff, L. A., Kriebel, J. K., Nuzzo, R. G. & Whitesides, G. M. *Chem. Rev. Chem. Rev.* **105**, 1103 (2005).
48. Love, J. C., Estroff, L. a, Kriebel, J. K., Nuzzo, R. G. & Whitesides, G. M. *Self-assembled monolayers of thiolates on metals as a form of nanotechnology. Chem. Rev.* **105**, 1103–69 (2005).
49. Janssen, D. Self-assembling monolayers for organic thin-film transistors. (2006). at <<https://lirias.kuleuven.be/handle/1979/330>>
50. Ishida, T. *et al. J. Phys. Chem.* **106**, **23**, 5886 (2002).
51. Bhushan, B. *Principles and Applications of Tribology*. (John Wiley & Sons, Inc., 1999).
52. Maboudian, R., Ashurst, W. R. & Carraro, C. Self-assembled monolayers as anti-stiction coatings for MEMS: characteristics and recent developments. *Sensors Actuators A Phys.* **82**, 219–223 (2000).
53. Srinivasan, U., Houston, M. R., Howe, R. T. & Maboudian, R. Alkyltrichlorosilane-based self-assembled monolayer films for stiction reduction in silicon micromachines. *J. Microelectromechanical Syst.* **7**, 252–260 (1998).
54. Xiang, H. & Komvopoulos, K. Effect of fluorocarbon self-assembled monolayer films on sidewall adhesion and friction of surface micromachines with impacting and sliding contact interfaces. *J. Appl. Phys.* **113**, 224505 (2013).

55. Maboudian, R., Ashurst, W. R. & Carraro, C. Tribological challenges in micromechanical systems. *Tribol. Lett.* **12**, 95–100 (2002).
56. Xu, G., Bao, Z. & Groves, J. Langmuir-Blodgett films of regioregular poly (3-hexylthiophene) as field-effect transistors. *Langmuir* 1834–1841 (2000).
57. Collet, J., Bonnier, M., Bouloussa, O., Rondelez, F. & Vuillaume, D. *Microelectron. Eng.* **36**, 119 (1997).
58. Sakuma, H., Iizuka, M., Nakamura, M., Kudo, K. & Tanaka, K. Fabrication of Field-Effect Transistor Using Charge-Transfer-Complex Langmuir-Blodgett Films. *Jpn. J. Appl. Phys.* **41**, 2727–2729 (2002).
59. Gee, M. L., Healy, T. W. & White, L. R. Hydrophobicity effects in the condensation of water films on quartz. *J. Colloid Interface Sci.* **140**, 450–465 (1990).
60. Vigil, G., Xu, Z., Steinberg, S. & Israelachvili, J. Interactions of Silica Surfaces. *J. Colloid Interface Sci.* **165**, 367–385 (1994).
61. Krishnamoorthy, A., Chanda, K., Murarka, S. P., Ramanath, G. & Ryan, J. G. Self-assembled near-zero-thickness molecular layers as diffusion barriers for Cu metallization. *Appl. Phys. Lett.* **78**, 2467–2469 (2001).
62. Bishop, A. R. & Nuzzo, R. G. Self-assembled monolayers: Recent developments and applications. *Curr. Opin. Colloid Interface Sci.* **1**, 127–136 (1996).
63. Sung, M. & Kim, Y. Self-assembled monolayers of alkanethiols on clean copper surfaces. *Bull. Chem. Soc.* **22**, 748–752 (2001).
64. Mikami, N., Hata, N., Kikkawa, T. & Machida, H. Robust self-assembled monolayer as diffusion barrier for copper metallization. *Appl. Phys. Lett.* **83**, 5181 (2003).
65. Ramanath, G. *et al.* Self-assembled subnanolayers as interfacial adhesion enhancers and diffusion barriers for integrated circuits. *Appl. Phys. Lett.* **83**, 383 (2003).
66. Ganesan, P. G., Singh, a. P. & Ramanath, G. Diffusion barrier properties of carboxyl- and amine-terminated molecular nanolayers. *Appl. Phys. Lett.* **85**, 579 (2004).
67. Gandhi, D. D. *et al.* Molecular-nanolayer-induced suppression of in-plane Cu transport at Cu-silica interfaces. *Appl. Phys. Lett.* **90**, 163507 (2007).

68. Gandhi, D. D. *et al.* Annealing-induced interfacial toughening using a molecular nanolayer. *Nature* **447**, 299–302 (2007).
69. Maestre Caro, a., Maes, G., Borghs, G. & Whelan, C. M. Screening self-assembled monolayers as Cu diffusion barriers. *Microelectron. Eng.* **85**, 2047–2050 (2008).
70. Caro, A. M. *et al.* High Quality NH₂SAM (Self Assembled Monolayer) Diffusion Barrier for Advanced Copper Interconnects. *MRS Proc.* **1249**, F02–01 (2010).
71. Caro, A. M. *et al.* Bottom-Up Engineering of Subnanometer Copper Diffusion Barriers Using NH₂-Derived Self-Assembled Monolayers. *Adv. Funct. Mater.* **20**, 1125–1131 (2010).
72. Carnevali, G. Self-assembled monolayers for electroless metallization in TSV integration. (2013).
73. Parikh, A. & Allara, D. An intrinsic relationship between molecular structure in self-assembled n-alkylsiloxane monolayers and deposition temperature. *J. Phys. Chem.* **98**, 7577–7590 (1994).
74. Chailapakul, O. & Sun, L. Interactions between organized, surface-confined monolayers and vapor-phase probe molecules. 7. Comparison of self-assembling n-alkanethiol monolayers. *J. Am. Chem. Soc.* **115**, 12459–12467 (1993).
75. Djokic, S. S. & Cavallotti, P. L. in *Electroless Depos. Theory Pract.* 252 (2010).
76. Hajdu, G. O., Hajdu, M. & Hajdu, J. B. Electroless Plating: Fundamentals and Applications. *Am. Electroplat. Surf. Finischers Soc.* (1990).
77. Schlesinger, M. *Electroless Deposition of Nickel, in Modern Electroplating, Fifth Edition.* (2011).
78. Shacham-Diamond, Y., Dubin, V. M. & Argyal, M. *Thin Solid Film.* **262**, 93 (1995).
79. Dubin, V. M., Shacham-Diamond, Y., Zhao, B., Vasudev, P. K. & Ting, C. H. *Journal of The Electrochemical Society. J. Electrochem. Soc.* **144**, 93 (1997).
80. Bindra, P. & White, J. R. in *Electroless Plat. - Fundam. Appl.* (Publishing/Noyes, W. A.) 289 (1990).
81. Gorbunova, K., Ivanov, M. & Moiseev, V. *Journal of Electrochemical Society.* **120**, 613 (1973).

82. Mallory, G. *Plating*. **58**, 319 (1971).
83. Cavallotti, P. L. & Salvago, G. *Electrochimica Metalli*. **3**, 239 (1968).
84. Novotortseva, I. G., Gaevskaya, T. V. & Tsybul'skaya, L. S. *Bulletin of Belarussian State University*. **2**, 16–20 (1994).
85. Gaevskaya, T. V., Novotortseva, I. G. & Tsybul'skaya, L. S. *Russian Journal of Applied Chemistry*. **68**, 587–592 (1995).
86. Novotortseva, I. G., Gaevskaya, T. V. & Tsybul'skaya, L. S. *Izvestiya Belarussian Academy of Sciences. Ser. Chem. Sci.* 49–54 (1995).
87. Novotortseva, I. G. & Gaevskaya, T. V. *Inorganic Materials*. **31**, 1053–1058 (1995).
88. Rao, Q., Bi, G., Lu, Q., Wang, H. & Fan, X. Microstructure evolution of electroless Ni-B film during its depositing process. *Appl. Surf. Sci.* **240**, 28–33 (2005).
89. Ohno, I., Wakabayashi, O. & Haruyama, S. *Denki Kagaku*. **53**, 190 (1985).
90. Shipley, C. R. J. *U. S. Pat.* 3011920 (1961).
91. O'Sullivan, E. J. *et al.* Electrolessly deposited diffusion barriers for microelectronics. *IBM J. Res. Dev.* **42**, 607–620 (1998).
92. Takano, N., Kurokawa, T., Osaka, T. & Kazuyoshi, U. Electroless Nickel Ternary Alloy Films for Copper Interconnection Technology. **3639**, 3639 (1999).
93. Shacham-Diamand, Y. & Lopatin, S. Integrated electroless metallization for ULSI. *Electrochim. Acta* **44**, 3639–3649 (1999).
94. Osaka, T. *et al.* All-wet fabrication process for ULSI interconnect technologies. *Electrochim. Acta* **51**, 916–920 (2005).
95. UVO-CLEANER® Model 42 SERIES Instruction Manual, Jelight Company, Inc. **1**,
96. Delande, T. & Armini, S. *SELF ASSEMBLED MONOLAYERS SAM'S SILANIZATION OVEN 39261*. (2012).
97. Rip, J. & Robert, S. *Work instructions for Dataphysics OCAH230L contact angle measurement system*. 1–35 (2009).
98. Schoofs, G. *SENTECH SE400PV Ellipsometer: Work Regulations*. 1–26 (2012).

-
99. Yasaka, M. X-ray thin-film measurement techniques. *Rigaku J.* **26**, (2010).
 100. Hilde, T. *Uitvoering van standaard metingen op Bede Metrix-L.* 1–18 (2013).
 101. Hellin, D. *et al. Basics of TXRF & VPD-DC-TXRF for metallic contamination analysis.*
 102. Vranckx, N. & Doc, J. F. *Total Reflection X-Ray Fluorescence.* (2009).
 103. Total Reflection X-ray Fluorescence (TXRF) | XOS. at <http://www.xos.com/techniques/xrf/total-reflection-x-ray-fluorescence-txrf/>
 104. Jiang, E. J. Advanced FT-IR Spectroscopy, in *Princ. Exp. Appl. Res. Nicolet™ FT-IR Spectrometers*
 105. Schoofs, G. *User guidelines Nicolet 6700 FTIR tool.* 1–54 (2011).
 106. Steigerwald, J. M., Murarka, S. P. & Gutmann, R. J. *Chemical Mechanical Planarization of Microelectronic Materials.* 377 (1997).
 107. Awano, Y. *et al. Carbon Nanotubes for VLSI: Interconnect and Transistor Applications. Proc. IEEE* **98**, 2015–2031 (2010).
 108. CMP, chemical mechanical planarization, polishing equipment. at <http://www.crystec.com/alpovere.htm>
 109. Teugels, L. MecapolToolGuide260213.
 110. Calvert, J., Chrisey, L. & Dressick, W. Selective attachment of nucleic acid molecules to patterned self-assembled surfaces. *US Pat. 5,688,642* (1997). at <http://www.google.com/patents/US5688642>
 111. Wilson, K. OF ALKYL SILANE SELF-ASSEMBLED MONOLAYERS FOR CELL PATTERNING AND DEVELOPMENT OF BIOLOGICAL MICROELECTROMECHANICAL. (2009).

Aknowledgments